Nanoscale analysis of human G1 and metaphase chromatin in situ

Jon Ken Chen[1], Tingsheng Liu (刘廷生)[1], Shujun Cai (蔡舒君)[1], Weimei Ruan[2], Cai Tong Ng[1], Jian Shi[1], Uttam Surana[2,3], and Lu Gan (甘露)[1,✉]

[1] Department of Biological Sciences and Centre for BioImaging Sciences, National University of Singapore, Singapore 117543

[2] Institute of Molecular and Cell Biology and Agency for Science Technology and Research, 61 Biopolis Drive, Singapore 138673

[3] Department of Pharmacology, National University of Singapore, Singapore 117543

✉ Correspondence: lu@anaphase.org

Keywords:
Chromatin, mitosis, mammalian cells, nucleosome, condensation, cryo-ET

Abbreviations used:
cryo-ET: electron cryotomography / cryo-electron cryotomography
Megacomplex: multi-megadalton globular complexes

New terms:
Dense irregular bodies

ABSTRACT

The structure of chromatin at the nucleosome level inside cells is mysterious. Here we present *in situ* cryo-ET analyses of chromatin in both G1 and metaphase RPE-1 cells. G1 nucleosomes are concentrated in globular chromatin domains and metaphase nucleosomes are concentrated in the chromatids. Classification analysis reveals that canonical mononucleosomes, ordered stacked dinucleosomes, and mononucleosomes with a disordered gyre-proximal density are abundant in both cell-cycle states. Class averages that have more than two stacked nucleosomes or that have side-by-side dinucleosomes are not detected, suggesting that groups of more than two nucleosomes are heterogeneous. Large multi-megadalton structures are abundant in G1 nucleoplasm, but not found in G1 chromatin domains and metaphase chromatin. The macromolecular phenotypes studied here represent a starting point for the comparative analysis of condensation in normal and unhealthy human cells, in other cell-cycle states, other organisms, and *in vitro* chromatin assemblies.

INTRODUCTION

Eukaryotic chromosomes are long nucleoprotein polymers (chromatin) whose basic units are called nucleosomes. The canonical nucleosome is a 10-nm wide, 6-nm thick cylindrical structure that consists of an eight-histone protein core surrounded by 1.65 left-handed turns (145 – 147 base pairs) of ordered DNA (Hewish and Burgoyne, 1973; Kornberg, 1974; Luger et al., 1997; Olins and Olins, 1974). Sequential nucleosomes are connected by short stretches of linker DNA. Groups of nucleosomes (oligonucleosomes) are believed to interact and pack in higher-order structures. Electron microscopy studies of purified and cellular samples have led to diverse higher-order chromatin models, including the 30-nm fiber (Finch and Klug, 1976), arc-shaped nucleosome stacks (Dubochet and Noll, 1978), liquid-like chromatin (Eltsov et al., 2008; McDowall et al., 1986), zig-zags (Bednar et al., 1998), 5- to 24-nm-thick fibers (Ou et al., 2017), plates (Chicano et al., 2019), 100- to 200-nm periodic structures (Hayashida et al., 2021), and 200-nm-wide slinkies of sequentially stacked nucleosomes (Sedat et al., 2022a; Sedat et al., 2022b). These models have not been adequately tested *in situ* in the absence of traditional-EM sample-preparation perturbations.

In metazoans, chromatin is distributed throughout the nucleus during interphase (Huxley and Zubay, 1961) and compacted to individualized chromosomes in mitosis (Flemming, 1880). Super-resolution microscopy studies of interphase mammalian cells have detected small irregular clusters of nucleosomes called clutches (Ricci et al., 2015) and 160- to 500-nm-wide chromatin-rich regions called “chromatin domains” (Barth et al., 2020; Fang et al., 2018; Li et al., 2021; Miron et al., 2020; Nagashima et al., 2019; Nozaki et al., 2017; Otterstrom et al., 2019; Xiang et al., 2018; Xu et al., 2018). Chromatin domains have also been indirectly detected by super-resolution microscopy of mitotic cells (Nozaki et al., 2017). Correct chromatin organization is required for important mitotic phenotypes like transcriptional repression and accurate segregation. Recent cryo-EM advancements make it possible to study these rearranged states at the nucleosome level in 3-D.

Electron cryotomography (cryo-ET) is a popular form of cryo-EM that is used to study the *in situ* 3-D structure of cells in a frozen-hydrated life-like state, without the artifacts associated with the chemical fixation, dehydration, and staining (Ng and Gan, 2020). *In situ* cryo-ET studies of eukaryotic chromatin have been done in microbial (Cai et al., 2018b; Cai et al., 2020; Chen et al., 2016; Gan et al., 2013; Tan et al., 2023), human (Cai et al., 2018a), and insect cells (Eltsov et al., 2018; Fatmaoui et al., 2022). These studies confirmed that the chromatin of multiple species is irregular *in situ* (Itoh et al., 2021). Importantly, cryo-ET can reveal nucleosome-level chromatin structure (Cai et al., 2018a; Eltsov et al., 2018), non-chromatin globular multi-megadalton complexes (megacomplexes), and “pockets” – regions that are devoid of megacomplexes and nucleosome-like particles (Cai et al., 2018b). When groups of macromolecular complexes that have very similar conformations are abundant, they manifest as unambiguous class averages in 3-D classification and subtomogram averaging analysis. *In situ* cryo-ET is therefore an essential tool to test different chromatin compaction models and to discover previously undescribed molecular phenotypes.

Here we present cryo-ET analysis of chromatin in cryo-FIB-milled RPE-1 cells, arrested in G1 phase (herein abbreviated to G1) and in metaphase. These cell-cycle states represent the extremes of both chromosome condensation and of transcriptional activity. Our study reveals differences in chromatin structure spanning length scales from ~2 nm to more than 100 nm, from the mononucleosome to the chromatin domain level. Subtomogram classification and averaging analyses reveal canonical nucleosomes and other nucleosome-containing assemblies not seen in previous studies. Remapping shows that G1 chromatin packs into domains and that metaphase chromatin does not have internal domain-like structure. These findings allow us to find the structural features that are shared and that deviate in two vastly different cell-cycle states.

RESULTS

Cell cycle synchronization

We used a pharmacological block-and-release protocol to enrich hTERT-immortalized human retinal pigment epithelial (RPE-1) cells in both G1 and metaphase (Scott et al., 2020). First, G1 cells are enriched by arrest with palbociclib. The cells are then released from G1, allowed to grow, and treated with nocodazole to arrest at prometaphase. Finally, the cells are washed free of nocodazole and immediately incubated in MG132 to allow progression to and then arrest at metaphase (**Figure S1A**). This mitotic arrest is reversible (Scott et al., 2020), which we confirmed by following the loss of mitotic markers histone H3 phosphorylated at serine 10 and Cyclin B1 (**Figure S1B**). The cytology of both G1 and metaphase cells and chromosomes were verified by immunofluorescence microscopy (**Figure S1, C and D**). Herein, we refer to palbociclib- and MG132-arrested cells as G1 and metaphase cells, respectively.

In addition to morphological differences, an important phenotypic difference between interphase and mitotic chromatin is the repression of transcription in mitosis. To confirm these phenotypes in synchronized RPE-1 cells, we used antibodies specific for the RNA polymerase II (RNAPII) large subunit Rpb1's C-terminal heptad repeats YSPTSPS phosphorylated at S5 (CTD-S5P) and at S2 (CTD-S2P). These epitopes indicate initiating RNAPII and elongating RNAPII, respectively (Harlen and Churchman, 2017; Komarnitsky et al., 2000). As expected, both forms of RNAPII were detected in G1 cell nuclei and were largely excluded from the chromatin of metaphase cells (**Figure 1**). These immunofluorescence results are consistent with the near-global repression of chromatin transcription in metaphase cells.

Optimization of cryoprotectants for cellular cryo-ET

In cellular cryo-EM and cryo-ET experiments, cells are frozen and imaged in conditions that immobilize the water molecules in a glassy "vitreous ice" state that resembles the life-like disordered form (Dubochet et al., 1988). Cryo-EM images of intact eukaryotic cells have poor contrast because cells are generally too thick. Therefore, frozen-hydrated cellular samples are made much thinner by either cryosectioning (Ladinsky et al., 2006; Studer et al., 2014) or cryo-FIB milling (Hayles et al., 2007; Marko et al., 2006; Medeiros et al., 2018; Rigort et al., 2010; Schaffer et al., 2015; Villa et al., 2013). We did pilot experiments on metaphase RPE-1 cells prepared by sequential thymidine block and Taxol-induced arrest (before the Scott protocol was published). These cells were then self-pressurized frozen, which is a method we have previously used to prepare frozen-hydrated yeast for cryosections (Cai et al., 2018b; Ma et al., 2022; Ng et al., 2019; Ng et al., 2020), with dextran as an extracellular cryoprotectant. Compared to standard high-pressure freezing, self-pressurized freezing is faster and cheaper (Han et al., 2012; Yakovlev and Downing, 2011). In this method, a cellular sample is sealed in a copper tube, then submerged in liquid-ethane cryogen. The cellular material that is closest to the tube's inner-wall surface forms crystalline ice. This ice expands and pressurizes the material that is cooling deeper inside the tube, suppressing ice-crystal formation there. Unfortunately, our pilot samples had diffraction-contrast features (Dubochet et al., 1988) in the tilt-series projection images (**Figure S2, A and B**),

indicating that the ice within the frozen cells was crystalline instead of vitreous. Furthermore, the crevasse artifacts were more severe and the cryosections were more often detached from the carbon support in our RPE-1 samples than in our yeast ones. In the cryotomograms, condensed chromosomes have the expected dimensions (hundreds of nanometers) and are surrounded by ribosomes (**Figure S2, C and D**), as previously observed *in situ* (Eltsov et al., 2008; McDowall et al., 1986). Chromatin densities in our pilot samples appeared string-like, rather than granular, which may be an artifact from the crystalline ice. While these experiments show that our RPE-1 cryosections are inadequate as cryo-ET samples, they suggest that mitotic chromosomes can potentially be located due to different image features relative to the surrounding cytoplasm.

An alternative and more-popular way to prepare frozen-hydrated cells is plunge freezing. While the region of the cell at the mammalian nuclear periphery is just thin enough (~5 to 10 µm) to be plunge-frozen in a vitreous state (Cai et al., 2018a; Mahamid et al., 2016), both metaphase cells and the regions in the nuclei interior are thicker than this limit. Ice-crystal formation in thick plunge-frozen biological cryo-ET samples can be suppressed by prior treatment with cryoprotectants (Bäuerlein et al., 2022; Cai et al., 2022; Harapin et al., 2015). Glycerol and DMSO are popular cryoprotectants used to prepare cell-line cryostocks, so we treated cells with each of these cryoprotectants at different concentrations and then characterized their morphology by timelapse light microscopy (**Figure S3A**). RPE-1 cells that were incubated with 6% and higher concentrations of DMSO, but not glycerol, showed detachment from the tissue culture plate and shrinkage of the nucleus after a 6-minute treatment (**Figure S3, B and C**). At the highest concentration (9%) of DMSO and glycerol tested, we found that DMSO-treated cells start detaching in 2 minutes. Therefore, at the highest – and most cryoprotective – concentrations of DMSO, incubations need to be shorter than 2 minutes, which was done for all following experiments. While this cryoprotectant screen suggests that glycerol is better than DMSO, the experiments below show that DMSO treatment allows for higher image contrast and that the treatment time can be shortened to a few seconds.

To determine the effects of cryoprotectants on ice-crystal formation and image contrast, we performed cryo-ET of cryo-FIB-milled cryolamellae of G1 cells that had been treated with different concentrations of DMSO and glycerol. Due to the time-consuming nature of these tests, we used G1 cells, which are easier to prepare, and we used DMSO to screen the cryoprotectant concentration. Grids bearing the G1 RPE-1 cells were briefly immersed in PBS+Ca+Mg plus cryoprotectant, then immediately mounted in the Vitrobot, blotted manually and then plunged into propane-ethane mix (details in Methods). Because cryoprotection is expected to change with sample thickness, we kept our analysis to regions of approximate equal thickness, namely the nuclear periphery, which could be located by the distinctive double membranes of the nuclear envelope. Tilt series of these samples show that ice-crystal diffraction contrast occupied large regions in samples treated with ≤ 3% cryoprotectant, smaller regions in 6% cryoprotectant (**Figure S4**), and were undetectable in most samples in 9% cryoprotectant.

Next, we collected cryo-ET data of cells in 9% glycerol for comparison with 9% DMSO, in both defocus phase contrast and with Volta phase plate (VPP). VPP data have more low-resolution contrast than defocus phase-contrast data (Danev et al., 2014; Fukuda et al., 2015). This extra contrast facilitates the detection of macromolecular complexes in challenging samples like cryotomograms of cells, especially if contrast is further lowered by cryoprotectant. We found that cells treated with 9% glycerol produce cryotomograms with unacceptably low contrast, even when the VPP is used (**Figure S5**). Therefore, a brief 9% DMSO treatment offers the best combination of cryoprotection and contrast. In all subsequently collected tilt series, only those without diffraction-contrast artifacts were used for further analysis.

To control for the potential disruption of nucleosomes in 9% DMSO, we plunge-froze HeLa oligonucleosomes in either pure storage buffer or storage buffer plus 9% DMSO, followed by cryo-ET with a VPP. Cryotomogram densities showed the characteristic beads-on-string motifs are preserved in 9% DMSO (**Figure S6**). Nucleosomes have a conspicuous double-gyre motif (two 10-nm-long parallel linear densities) in cryotomographic slices (**Figure S6, insets**). This double-gyre motif is evident when the nucleosome is oriented with its superhelical axis parallel to the ice surface, and corresponds to side and gyre views (Zhou et al., 2019). These observations suggest that the 9% DMSO treatment does not disrupt nucleosomes.

To further test if DMSO treatment alters nucleosome structure, we performed subtomogram analysis of the oligonucleosome samples (details in Methods). This workflow was originally established using nuclear lysates (Cai et al., 2018c) and has three major steps. First, nucleosome-like particles are template-matched using a rounded-cylinder reference. Template matching done this way is analogous to single-particle cryo-EM automated particle picking using a Gaussian (2-D) blob that has dimensions similar to the complex under study. Given the simplistic nature of the reference, template-matching hits are not considered to be “identified” nucleosomes, so we refer to them as candidate nucleosomes. Second, canonical nucleosomes are identified based on their structure by sequential 2-D and then 3-D subtomogram classification. Alternatively, the subtomograms are 3-D classified directly (2-D classification skipped), resulting in more nucleosomes detected, though at a cost of computation time . Third, the subtomogram class averages are inspected for known structures, which are subsequently refined in 3-D. Canonical nucleosome class averages were detected in both the absence of DMSO (**Figure S7A**) and presence of 9% DMSO (**Figure S7B**). Refinement of the canonical nucleosome classes that have the highest-resolution features resulted in a 19 – 19.5 Å resolution subtomogram averages; both classes resemble the canonical nucleosome with some ordered linker DNA as expected of oligonucleosome samples. In summary, brief immersion in medium containing 9% DMSO both cryoprotects plunge-frozen cells and preserves nucleosome structure. In the following cryo-ET experiments, all samples were cryoprotected in medium with 9% DMSO.

Overview of the G1 nucleus interior
G1-arrested cells were immersed in medium containing 9% DMSO, plunge-frozen, cryo-FIB milled, and then imaged by VPP cryo-ET. In the G1 cell nucleus cryotomographic slices, we observed masses of nucleosome-like densities, both near the nuclear envelope (**Figure 2A**) and further in the nuclear interior (**Figure 2B**). An additional example cryotomographic slice from another G1 cell is shown in **Figure S8**. To control for the cryolamellae quality, we template matched cytoplasmic ribosomes in G1 cryolamellae (**Figure S9**) and then directly 3-D classified the candidate ribosomes to yield 684 ribosome subtomograms. Note that the low number of ribosomes results from the targeting of nuclei, meaning that cytoplasm occupies small portions of the fields of view. The refined average is at ~33 Å resolution (**Figure S9B**) and has the same handedness as and comparable features to density maps of human ribosome single-particle cryo-EM reconstructions (Khatter et al., 2015) simulated at similar resolutions (**Figure S9C**).

Densities that resemble the nucleosome gyre view are abundant in the locally concentrated groups (chromatin domains; see below) in both intranuclear regions (**Figure 2, C and E**). In addition to nucleosome-like densities, the G1 nucleus contains conspicuous non-nucleosome features, of which the most abundant are megacomplexes (**Figure 2D**). Because the best-characterized nuclear megacomplexes are preribosomes, we template matched them using a spherical reference. We performed both 2-D and 3-D classification, yielding one class average of candidate preribosomes (**Figure S10A**). The preribosome average resembles the 60S complex, which is apparent when the refined structure is oriented to the large subunit of the 80S ribosome (**Figure S10B**). In addition to preribosomes, G1 nuclei have dense bodies that have irregular shapes and dimensions more than 40 nm (**Figure 2F**); because they are much larger than megacomplexes, herein we refer to them as “dense irregular bodies". The dense irregular bodies do not have any double-gyre motifs, suggesting that they do not contain nucleosomes. They are also not a result of DMSO treatment because we have, in retrospect, observed them in other cells that were not treated with DMSO (see Discussion)

G1 chromatin domains have multiple ordered nucleosome species
The mammalian interphase nucleus contains both chromatin-rich and chromatin-poor regions. This uneven chromatin distribution is visible in confocal images of RPE-1 cells (**Figure 1**), consistent with recent confocal and super-resolution studies of other cell types (Barth et al., 2020; Cho et al., 2022; Fang et al., 2018; Li et al., 2021; Miron et al., 2020; Nagashima et al., 2019; Nozaki et al., 2017; Otterstrom et al., 2019; Xiang et al., 2018; Xu et al., 2018). The super-resolution studies have named the 100- to 500-nm-wide compact chromatin-rich regions “chromatin domains”. Because the nucleosome-rich regions that we see in G1 cells have dimensions compatible with the chromatin domains seen by super-resolution microscopy, herein we call them “chromatin domains”, and for brevity, we refer to the chromatin-poor regions as nucleoplasm.

To get insight into the nucleosome organization of G1 cells, we performed subtomogram analysis using a cylindrical reference, which minimizes model bias. We

sped up this initial analysis by doing template matching with a larger grid spacing of 21 nm. The expectation is that a subset of nucleosomes will be missed, which is acceptable as long as the analysis provides a representative sample of structures within this large dataset. We analyzed the chromatin domains by direct 3-D classification of the template-matched candidate nucleosomes. To limit the effects of neighboring particles in the alignment and classification, we used a tight 110 Å diameter spherical mask. As a positive control, we restricted subtomogram analysis to the chromatin domains and found canonical nucleosome class averages (**Figure S11A**), like we saw in HeLa (Cai et al., 2018a). These class averages have the unmistakable features of canonical nucleosomes: a ~10-nm-long double-gyre density that follows a left-handed ~1.65 turn helical path. Next, we performed a negative control subtomogram analysis of the cytoplasm, which does not have chromatin. As expected, the cytoplasm does not have any nucleosome class averages (**Figure S11B**).

To increase the number of detectable nucleosomes, we repeated the template matching with a smaller 7 nm grid spacing. Three-dimensional classification of the resultant hits revealed 4 canonical-nucleosome class averages (**Figure S12A**). Two of these class averages had an extra density near one face, suggesting the presence of a nearby complex that was potentially excluded by the tight spherical mask. Because cryotomographic slices had densities that resemble stacked nucleosomes (**Figure 2, B and D**), we repeated 3-D classification, except using a stacked-double-cylinder reference and a mask large enough (240 Å sphere) to accommodate two nucleosomes (**Figure S12B**). Classification with these new parameters revealed two classes that each had a canonical nucleosome and an extra density near the face. The subtomograms belonging to these two classes were pooled and subjected to a second round of 3-D classification, using the larger mask and one of the nucleosome class averages as the reference (**Figure S12C**). This second round of classification revealed a stacked dinucleosome class average and six class averages that have an ordered mononucleosome plus an extra, disordered density. In the stacked dinucleosome, both nucleosome densities have unambiguous features of mononucleosomes with DNA gyres well resolved; herein we refer to this class as ordered stacked dinucleosomes. Here, the term “ordered” implies that there are sufficient numbers of canonical nucleosome pairs that are oriented and positioned with very low heterogeneity, resulting in a class average with two unambiguous canonical nucleosome densities. Stacked dinucleosomes have a broader range of inter-nucleosome orientations and positions would be too heterogeneous to resolve as a separate, unambiguous class average.

To potentially detect more subtomograms that contain a canonical nucleosome, we repeated the first round of 3-D classification with the larger mask and using the stacked dinucleosome class average as the reference (**Figure S12D**). This modified classification strategy revealed three groups of class averages: (1) canonical nucleosomes, (2) a stacked dinucleosome, and (3) a canonical nucleosome with a large noisy density near the DNA gyres (**Figure S12D**). Each of these three groups of nucleosomes was subjected to a third round of classification, resulting in seven classes from group 1, three classes from group 2, and five classes from group 3 (**Figure S12E**). Group 1’s class averages primarily differ in the length of the linker DNA and the noisy

densities near the nucleosome face, so we refined each class average separately. Group 2's classes differ primarily in their noise densities, so we pooled them for refinement. Group 3's class averages have gyre-proximal densities at variable positions, so we refined each class separately. The 13 refined class averages have resolutions ranging from 24 to 34 Å (**Figure S13, Movie S1**).

The seven refined mononucleosome class averages (Group 1) differ by the length of ordered linker DNA **(Figure 3A)**. Furthermore, three of these class averages have asymmetry in the lengths of the two linker DNAs. Note that the difference in the subtomogram averages' linker DNA lengths may result either from the absolute length of the individual nucleosomes' linkers or from the heterogeneity of the linker DNA structure (see Discussion). When rendered at a lower contour level, the classes have a heterogeneous extra density near one of the faces (**Figure S13A**), indicating that another complex is present, though at a lower occupancy (more details below). Remapping analysis in the later section suggests that some of gyre-proximal densities have contributions from other nucleosomes.

The two nucleosomes of the ordered stacked dinucleosome class average (Group 2) differ in the lengths of ordered linker DNA (**Figure 3B and S13B**). As with the Group 1 mononucleosomes, the linker DNA density could appear shorter in one of the dinucleosome average's members due to either short linker DNA or variable linker DNA conformation in the contributing nucleosomes (see Discussion). Earlier single-particle cryo-EM analysis of recombinant oligonucleosome arrays revealed dinucleosome stacking (Dombrowski et al., 2022; Garcia-Saez et al., 2018; Song et al., 2014). Both the tetranucleosome and twisted-fiber arrays show two types of dinucleosome stacking: closely packed dinucleosomes (Type I interface) and less-closely packed nucleosomes (Type II interface). Following the nomenclature in these studies, the G1 stacked dinucleosome structures we observe have the Type II interface (**Figure 3B**).

Nucleosomes with a gyre-proximal density (Group 3) are conformationally variable (**Figure 3C and S13C**). Each class average has a canonical nucleosome – albeit with lower-resolution features than in the mononucleosome and stacked dinucleosome classes. These class averages refined lower resolutions than the other groups (30 – 34 Å vs. low ~20s Å resolution; **Figures S13, D – F**). Compared to the other groups, the disc views of this group are undersampled (**Figure S13G**), meaning that the members of this class are more abundant than the numbers detected here. When rendered at a lower contour level, an additional noisy density becomes visible proximal to the DNA gyres. Even though the additional densities appear noisy, they are not uniformly distributed around the gyre. Instead, their centers of mass are at four different superhelical locations (seven when the nucleosome's pseudo-twofold symmetry is considered); see the analysis with docked nucleosome crystal structure below.

Other ordered multiple-nucleosome motifs are not detected in G1

We also attempted to detect ordered sets of nucleosomes packed in other arrangements. One such arrangement is the side-by-side dinucleosome. The original mask (240 Å sphere) is big enough to accommodate a side-by-side dinucleosome.

However, the isotropic shape of the mask can enclose other nearby particles, which, if heterogeneous, would interfere with both alignment and classification. We therefore designed both a mask and low-resolution reference that better conform to the longer aspect ratio needed to accommodate two nucleosomes packed side-by-side. We then performed another round of 3-D classification on the subtomograms from Group 3 using the new mask and reference. However, none of the resultant class averages revealed two canonical nucleosome densities (**Figure S14A**).

The presence of ordered stack dinucleosomes raised the possibility of stacks with more than two ordered nucleosomes. To test if ordered stacking extends beyond two nucleosomes in G1 chromatin domains, we modified our classification workflow to accommodate either three or four stacked nucleosomes (**Figure S14B**). We used stacked tubular masks instead of a spherical one and we used the stacked dinucleosome class average as the reference for an additional round of 3-D classification on the subtomograms from Group 2. No ordered tri- or tetranucleosome stacks emerged from 3-D classification. A few classes have noisy densities above/below the upper-most/bottom-most ordered nucleosome, which may correspond to an additional heterogeneously oriented/positioned nucleosome or other macromolecular complex. Because the ordered stacked trinucleosome and tetranucleosome would be part of stacks with even more ordered nucleosomes (pentanucleosomes, hexanucleosomes, etc.), class averages with larger ordered stacked nucleosome assemblies would also be absent.

G1 chromatin domains are irregular and have few megacomplexes and pockets
To visualize the overall shape of these chromatin-rich regions, we used the EMAN2 convolutional neural network tool (Chen et al., 2017; Tang et al., 2007) to train and then automatically segment the chromatin domains (**Figure S15**). Segmentations were done at both the nuclear periphery and the nuclear interior (more examples in **Figure S16**). Because the cryolamellae are thinner than the chromatin domains, the segmentation samples a random slice through each domain. Nevertheless, all chromatin domain segmentations have irregular shapes, suggesting that the domains are themselves irregular because random sections through platonic bodies like spheres and ovoids would have circular and oval profiles, respectively.

To visualize the nucleosomes' *in situ* 3-D distribution, we remapped them into the volume of the original cryotomogram along with the preribosomes and (cytoplasmic) ribosomes (**Figure 3D, Movie S2**). Consistent with the appearance of cryotomographic slices, the nucleosomes were not mixed with the preribosomes (megacomplexes). Instead, they are concentrated in regions that span several hundred nm as expected of chromatin domains. The remapped model shows that the chromatin domains have irregular shapes, like we expected based on the segmentations. Stacks with four nucleosomes are also present in the remapped model (**Figure 3D, inset II**), but are not ordered because their numbers were too low to detect as a class average with multiple unambiguous nucleosome densities; see similar analysis of metaphase chromatin below.

Our previous cryo-ET study of condensed fission yeast mitotic chromatin brought our attention to two non-chromatin features – megacomplexes and regions devoid of macromolecular complexes, which we termed pockets (Cai et al., 2018b). After visually inspecting 21 cryotomograms, we found only one candidate intra-domain megacomplex. In these cryotomograms, we did not find any unambiguous pockets such as the ones seen in metaphase chromatin (see below). In summary, G1 chromatin domains have few non-chromatin features that we have previously seen in condensed fission yeast chromatin.

Canonical nucleosome classes were not obtained from the nucleoplasm

Mammalian chromatin domains are thought to be connected by short stretches of chromatin "linker filaments" that extend through the nucleoplasm (Li et al., 2021; Miron et al., 2020). The composition of these linker filaments is unknown: they could be mostly naked DNA, oligonucleosome chains, or compacted chromatin fibers. In our cellular cryotomograms, we are unable to see naked DNA, but we can locate canonical nucleosomes by class averaging – if they are abundant. We therefore performed template matching followed by 3-D classification on subtomograms that were outside of the chromatin domains, i.e., within the nucleoplasm and some cytoplasm. The nucleoplasm is more constitutionally heterogeneous than the chromatin domains, so we used 200 classes, of which 157 remained non-empty after the run completed. Only one canonical-nucleosome class average was found (**Figure S17**), but remapping showed that they came from the periphery of the chromatin domains due to imperfect seeding of the initial search points (not shown). None of the other class averages bear resemblance to a nucleosome. Therefore, either the linker filament nucleosomes are too rare to manifest as a nucleoplasmic class average in our dataset or the linker-filament nucleosomes have structures that we do not yet recognize.

Overview of RPE-1 metaphase chromatin

We next prepared DMSO-cryoprotected cryo-FIB-milled metaphase-arrested cells and then recorded VPP cryo-ET data. Unlike G1 cells, in which the chromatin is separated from cytoplasm by a high-contrast easy-to-recognize nuclear envelope, metaphase chromosomes are in contact with the cytoplasm due to mitotic nuclear-envelope breakdown. This difference complicates metaphase-chromosome targeting for cryo-ET. Based on clues from our pilot cryotomograms of cryosections, we found that in the lower-magnification survey images of cryolamellae, cytoplasm regions of cryolamellae have granular and linear densities from ribosomes, membranes, and cytoskeleton; in contrast metaphase chromatin have more uniform densities (**Figure S18**). These visual cues greatly facilitated target selection. In cryotomographic slices, metaphase chromatin appear as large regions enriched with nucleosome-like particles and without any cytoplasmic constituents such as ribosomes, bundles of ~10-nm-diameter filaments (**Figure 4A**), and microtubule bundles (**Figure 4B**). Another metaphase cell example is shown in **Figure S19**.

Ribosomes are located near the surface of the condensed chromosomes (**Figure 4A**), consistent with previous analysis of both HeLa cell cryosections (Eltsov et al., 2008), U2OS cryolamellae (Zhao and Jensen, 2022), our cryosections (**Figure S2**), and

isolated metaphase chromosomes (Nishino et al., 2012). Spindle microtubules that are inserted into metaphase chromosomes were previously observed in U2OS cells (Kamasaki et al., 2013) and are also seen in the RPE-1 chromosomes (**Figure 4B**). Nucleosomes are also irregularly packed in the metaphase chromosome surface and interior, without any large higher-order chromatin structures like 30-nm fibers (Scheffer et al., 2011). In RPE-1 metaphase chromosomes, pockets are present (**Figure S19**), albeit rarer than in G1. However, neither megacomplexes nor dense irregular bodies were seen inside any of the metaphase chromatin regions in our dataset.

Mononucleosomes and stacked dinucleosomes in metaphase chromatin
The most conspicuous macromolecular complexes in metaphase chromatin are nucleosome-like particles (**Figure 4, C – F**). We performed template matching, subtomogram classification, and averaging of metaphase nucleosomes using the same image-processing parameters and workflow as for G1 chromatin (**Figure S20, A – E**). The individually refined mononucleosome class averages of group 1 have linker DNA of different lengths **(Figure 5A)**. Unlike in G1 chromatin, we did not find a class average that resembles the nucleosome core particle, which has barely detectable linker DNA. Some of the metaphase class averages with shorter linker length appear to be less well-defined, suggesting that they are more heterogeneous. We also observed a mononucleosome class with asymmetric linker DNA lengths. As with the G1 mononucleosome averages, the differences in metaphase mononucleosome linker DNA lengths could arise from multiple factors (see Discussion).

Metaphase chromatin also has numerous densities that resemble stacked nucleosomes (**Figure 4, C – F**). Accordingly, subtomogram analysis revealed ordered stacked metaphase dinucleosome class averages (**Figures S20 C – E and 5B**). We also found class averages of nucleosomes with a noisy density proximal to the gyres (**Figure S21C, Figure 5C**). We refined these class averages to 26 Å (mononucleosomes and stacked dinucleosomes) and 32 – 35 Å (nucleosomes with gyre-proximal densities) (**Figure S21, Movie S3**). When rendered at a lower contour level, the metaphase stacked dinucleosome and some of the mononucleosome class averages show an extra density near the nucleosome face, like what is seen in G1 (more details below).

We performed the modified search for ordered side-by-side dinucleosomes like we did for G1 chromatin and did not detect any candidates in the metaphase chromatin either (**Figure S22A**). Likewise, using the same modified strategy as for G1 chromatin, we attempted – and failed – to detect ordered stacked trinucleosomes in metaphase chromatin (**Figure S22B**). In summary, ordered stacked dinucleosomes, and nucleosomes with gyre-proximal densities are abundant in both G1 and metaphase cells, but ordered structures with two side-by-side or more than two stacked nucleosomes are not.

Next, we remapped the refined class averages of all three nucleosome groups and the ribosomes (**Figure 5D**). The remapped ribosomes localized exclusively outside the chromosome, consistent with the absence of megacomplexes inside. Remapping revealed a few sets of stacks with more than two nucleosomes (**Figure 5D, insets I –**

IV), suggesting that stacked tri- and tetranucleosomes are present (**Figures 4D and E, Movie S4**). These tri- and tetranucleosome stacks are too few to manifest as class averages with unambiguous nucleosomes. Therefore, nucleosome stacking can extend beyond two nucleosomes *in situ* in both G1 and metaphase, albeit with less order.

Detailed remapping analysis of nucleosome packing

As noted in our subtomogram classification above, at least one class average from each group has an extra density, which is visible at a sufficiently low contour level. To test if these densities are from other nucleosomes, we remapped all the class averages at low contour levels and then shaded them in different colors (**Figure 6**). This visualization scheme allowed us to see if any of the 'extra' densities overlapped with the nucleosome densities of neighboring class averages. In both G1 (**Figure 6A**) and metaphase (**Figure 6B**), we found examples where the extra density partially overlapped a nearby remapped nucleosome (black arrowheads), the extra density did not overlap with a remapped nucleosome but did partially overlap with a nucleosome-like density in the tomographic slice (gray arrowheads), and examples of no overlap with either a remapped nucleosome or a nucleosome-like density in the cryotomographic slice (white arrowhead. In the latter case, there was some overlap with unknown structures, suggesting that non-nucleosome complexes may also contribute to the extra densities. In summary, both nucleosomes and non-nucleosomes contribute to the heterogeneous extra densities in our class averages.

Comparative analysis of G1 and metaphase nucleosomes *in situ*

The organization of RPE-1 nucleosomes can be explored in greater detail by comparison with crystal structures. To simplify the analysis, we assigned the group 1 mononucleosome class averages into only two classes, based on either short or long linker DNA lengths. These two classes were then refined **(Figure S23)**, separately for G1 and metaphase nucleosomes. Next, we docked nucleosome and chromatosome crystal structures as rigid bodies in the refined class averages from both G1 (**Figure 7A**) and metaphase (**Figure 7B**). The main source of variation is the length of ordered linker DNA in the mononucleosome and the stacked dinucleosome structures. Both G1 and metaphase stacked dinucleosomes have a center-to-center spacings of ~6.8 nm. Comparison of the nucleosomes with gyre-proximal densities shows that the centers of mass of these densities populate the following approximate superhelical locations: 3.8, 4.8, 5.5 and 6 in G1 chromatin and 3.4, 3.9, 4.2 and 5 in metaphase chromatin. For nucleosomes with gyre-proximal densities, metaphase nucleosomes do not show interactions near the DNA entry/exit site whereas G1 nucleosomes do (superhelical location 6).

To assess how the populations of the ordered nucleosome-containing subtomograms differ in G1 and metaphase, we calculated the ratios of class averages of stacked dinucleosomes plus nucleosomes with gyre-proximal densities relative to the canonical mononucleosome class averages (all linker DNA lengths) in each cell-cycle state (**Table 1**)**.** Note that this analysis is limited because (1) the total number of canonical vs. non-canonical nucleosomes is unknown and (2) only ordered stacked dinucleosomes are considered here. We found modest differences in the class-average populations:

compared to G1 cells, metaphase cells have ~23% more stacked dinucleosomes and ~24% fewer nucleosomes with gyre-proximal densities relative to mononucleosomes.

DISCUSSION

At the micron length scale, interphase and mitotic chromatin have large morphological differences. Our study reveals both similarities and differences between G1 and metaphase chromatin from the nanometer to the hundred-nanometer length scales *in situ*. We are also able to compare the 3-D organization of intracellular nucleosomes to those studied in recent *in vitro* chromatin samples. The following discussion starts with the smallest length scale and goes to the largest.

In situ nucleosome structure and its role in higher-order structure

RPE-1 cells have canonical nucleosome class averages that differ in the length of ordered linker-DNA densities. The class averages that have long ordered linker DNA in a crossed configuration resemble the chromatosome, which is a nucleosome with an additional 10 to 25 bp of ordered linker DNA (Simpson, 1978; Zhou et al., 2015). A crystal structure of the chromatosome with 25 extra base pairs of ordered DNA per arm (Garcia-Saez et al., 2018) could be rigid-body docked into the subtomogram average of the nucleosome classes that have long linker DNA, suggesting that their *in situ* structure resembles the *in vitro* one. The averages that have shorter linker densities can arise from nucleosomes that indeed have shorter linker DNA, nucleosomes that have longer but structurally variable linker DNA, or a combination of both. A mononucleosome class average with ultra-short linker DNA was detected in G1 cells but not in metaphase cells, suggesting that linker DNA ordering may be a consequence of chromatin compaction. The class averages of nucleosomes with gyre-proximal densities all have ultra-short linker DNA, in both G1 and metaphase; these averages could result from nucleosomes that have ultra-short linker DNA or those that have more DNA structural heterogeneity. Nucleosome class averages that have short and long ordered linker DNA were also seen in both HeLa and budding yeast cells (Cai et al., 2018a; Tan et al., 2023), though canonical nucleosome class averages (regardless of linker DNA length) are much rarer in yeast.

Because we did not enforce C2 symmetry in our subtomogram analysis, the mononucleosome class averages show linker DNA length asymmetry. This asymmetry is also evident in the *in situ* class averages of HeLa and budding yeast cells (Cai et al., 2018a; Tan et al., 2023). Nucleosomes with asymmetric linker DNA structure have been seen in cryo-EM studies of nucleosomes with histones and DNA from cellular lysates (Arimura et al., 2021); reconstituted oligonucleosomes within small condensates (Zhang et al., 2022); digested native oligonucleosomes (Jentink et al., 2022); decondensed isolated mitotic chromosomes (Beel et al., 2021); and reconstituted chromatosomes (Bednar et al., 2017; Wang et al., 2021b; Zhou et al., 2021). In contrast, nucleosomes with symmetric linker DNA have been found *in vitro* in oligonucleosome arrays assembled from the Widom “601” sequence and that have more than two ordered nucleosomes (Dombrowski et al., 2022; Ekundayo et al., 2017; Garcia-Saez et al., 2018; Jentink et al., 2022; Lewis et al., 2021; Schalch et al., 2005; Song et al., 2014; Zhou et al., 2022). Taking into account the previous cryo-EM studies, our *in situ* data, and mesoscale simulations (Collepardo-Guevara and Schlick, 2014), we suggest that *in*

situ linker DNA conformational variability may suppress the formation of ordered oligonucleosome structures that have more than two nucleosomes.

Type II stacked dinucleosomes are abundant *in situ*

Both G1 and metaphase cells have ordered stacked dinucleosomes, in which DNA gyres and some linker DNA are resolved in both nucleosomes within the same class average. The *in situ* ordered stacked nucleosomes resemble those studied *in vitro* that interact via a Type II interface, (Dombrowski et al., 2022; Garcia-Saez et al., 2018; Song et al., 2014), in which the H4 N-terminal residues from one nucleosome contact the H2A-H2B acidic patch of its neighbor. The absence of symmetry enforcement allowed us to see that in the ordered stacked dinucleosome, the two nucleosomes have a ~10 bp difference in ordered linker DNA. We did not detect ordered trinucleosome stacks, meaning that the orientation and/or position of the third nucleosome is variable. Furthermore, while stacks with three nucleosomes are seen in cryotomographic slices (**Figure 4**) and stacks with up to four non-ordered nucleosomes were seen in remapped models (**Figures 3D, 5D, 6**), such arrangements are rare compared to ordered stacked dinucleosomes. The rarity of ordering beyond two nucleosomes is consistent with the absence of the larger ordered structures (fibers and plates; see below).

Nucleosome stacking has been observed in multiple contexts, with varying degrees of order. Stacking is found in preparations of mononucleosomes (Bilokapic et al., 2018; Dubochet and Noll, 1978; Eltsov et al., 2018; Zhou et al., 2018); reconstituted nucleosome arrays (Dombrowski et al., 2022; Ekundayo et al., 2017; Garcia-Saez et al., 2018; Geiss et al., 2014; Jentink et al., 2022; Lewis et al., 2021; Schalch et al., 2005; Song et al., 2014; Takizawa et al., 2020; Zhou et al., 2022); isolated natural chromatin (*ex vivo*) from chicken erythrocytes, starfish spermatozoids, picoplankton, and budding yeast (Cai et al., 2018c; Scheffer et al., 2012); isolated chicken erythrocyte nuclei (Scheffer et al., 2011); *in situ* in interphase HeLa, KE37, non-mitotic fly brain, and fly embryo cells (Cai et al., 2018a; Eltsov et al., 2018; Fatmaoui et al., 2022). In contrast, nucleosome stacking was not observed in either budding or fission yeast *in situ* (Cai et al., 2018b; Tan et al., 2023). In summary, these observations show that extensive nucleosome stacking is favorable both *in vitro* and *ex vivo* under some buffer conditions; limited nucleosome stacking is favorable *in situ* in RPE-1 cells; and that nucleosome stacking is unfavorable *in situ* in yeasts.

Other structures that have an ordered nucleosome

The detection of only one group of ordered dinucleosome class averages (stacked, Type II) indicates that other kinds of inter-nucleosome interactions – for example those required for side-by-side ordered interactions – are too few to manifest as an unambiguous class average. We did, however, detect multiple mononucleosome classes that have a gyre-proximal density of unknown composition. These densities are not distributed uniformly around the nucleosome disc; instead, their centers of masses occupy ~7 SHL positions. If these densities did occupy all possible positions around the gyres, then we probably would not be able to detect them because of their increased positional heterogeneity. Many nuclear complexes were shown to interact with the nucleosome gyres, including transcription factors (Michael et al., 2020; Nishimura et al.,

2022; Tanaka et al., 2020; Wang et al., 2021a), remodelers (Armache et al., 2019; Bacic et al., 2021; Baker et al., 2021; Chittori et al., 2019; Farnung et al., 2020; Farnung et al., 2017; Liu et al., 2017; Nodelman et al., 2022; Yan et al., 2019), histone-mark interactors (Finogenova et al., 2020; Grau et al., 2021; Kasinath et al., 2021; Liu et al., 2021; Poepsel et al., 2018) and RNA polymerase (Ehara et al., 2019; Ehara et al., 2022; Farnung et al., 2022; Farnung et al., 2018; Kujirai et al., 2018). Other gyre-interacting complexes include those that either ensconce much of the nucleosome or that bind to a distorted nucleosome (Chen et al., 2022b; Dodonova et al., 2020; Eustermann et al., 2018; Farnung et al., 2021; Han et al., 2020; He et al., 2020; Liu et al., 2020; Mashtalir et al., 2020; Patel et al., 2019; Wang et al., 2023; Wang et al., 2022b, Yuan, 2022; Willhoft et al., 2018). Our inspection of remapped subtomogram averages suggest that both nucleosome and non-nucleosome complexes may contribute to these gyre-proximal densities. Because many of these complexes are related to transcription, which is repressed in metaphase and active in G1, we speculate that nucleosomes may contribute more to the gyre-proximal densities in metaphase than in G1 cells.

Canonical nucleosomes are located in irregular domains in G1 but not metaphase
In RPE-1 G1 cell nuclei, most canonical nucleosomes are concentrated within the conspicuous chromatin domains. These domains have been seen in textbook traditional EM images and have been studied with renewed interest using advanced light microscopies (Barth et al., 2020; Cho et al., 2022; Fang et al., 2018; Li et al., 2021; Miron et al., 2020; Nagashima et al., 2019; Nozaki et al., 2017; Otterstrom et al., 2019; Xiang et al., 2018; Xu et al., 2018). Consistent with these super-resolution studies, chromatin domains have irregular shapes throughout the G1 RPE-1 nucleus, in the perinuclear region in a cryotomogram of an interphase HeLa cell cryolamella (Cai et al., 2018a), and in electron spectroscopic images of mouse fibroblast cells (Strickfaden et al., 2020). In contrast, domain-like features are not seen in the popular model yeasts *S. cerevisiae* and *S. pombe*, which have uniform chromatin distributions throughout the interphase nucleoplasm (Cai et al., 2018b; Chen et al., 2016; Tan et al., 2023).

Single-molecule localization studies have revealed the presence of domain-like features in mitotic cells. PALM imaging of mitotic mammalian cells revealed domains ranging from ~140 to 200 nm. (Nozaki et al., 2017). STORM imaging of histones in fixed mitotic cells (Xu et al., 2018) and of DNA in isolated metaphase chromosomes (Wang et al., 2022a) have revealed “nanodomains” – small ~50- to 90-nm granular features corresponding to locally concentrated chromatin. In our cryotomograms of metaphase cells, the canonical nucleosomes are uniformly distributed within the condensed chromosomes (with the exception of pockets; see below), i.e., we did not observe separate domain-like features within the metaphase chromatin. Human metaphase chromatin has also been studied *in situ* in 3-D by Chrom-EMT (Ou et al., 2017) and cryo-ET of cryo-FIB-milled cells (Zhao and Jensen, 2022). Neither of these EM-based studies reported any nanodomain-like features in mitotic chromatin. It is unclear what factors explain the visibility of mitotic chromosome domains and nanodomains in light-microscopy but not in electron microscopy data.

The size and shapes of oligonucleosome condensates have been characterized by both light and electron microscopy (Gibson et al., 2019; Maeshima et al., 2016; Sanulli et al., 2019; Strickfaden et al., 2020; Zhang et al., 2022). Condensates of dodecameric arrays can grow to more than 4 µm (Gibson et al., 2019; Sanulli et al., 2019), which are an order of magnitude larger than G1 chromatin domains but the same order as mitotic chromosomes. Furthermore, condensates of reconstituted arrays have circular profiles, presumably because they are 2-D projections of spherical bodies (Strickfaden et al., 2020). In contrast, condensates of fractionated (natural) chromatin are irregular (Maeshima et al., 2016). Subsequent studies using defined '601' chromatin arrays confirmed that longer arrays (with 62 nucleosome repeats) generate irregular condensates (Chen et al., 2022a) whereas arrays with 17 or fewer nucleosomes form rounded condensates (Chen et al., 2022a; Gibson et al., 2023). Condensates of reconstituted tetranucleosomes appear irregular during the early, spinodal phase of *in vitro* condensation and then fuse into larger round ones (Zhang et al., 2022). In summary, *in vitro* condensates of either natural chromatin, long artificial arrays, or tetranucleosomes at the early stages of compaction more closely resemble *in situ* G1 chromatin domains than condensates of (short) dodecameric arrays. It remains unknown how other nuclear factors, like histone post-translational modifications, remodelers, and chaperones would affect *in vitro* condensates.

Large-scale nucleosome packing is irregular in G1 and metaphase

The earliest *in situ* cryo-EM study of mammalian chromosomes was done on Chinese hamster ovary and HeLa cells. This study proposed that the mitotic chromatin inside these cells is irregular and "liquid-like" (McDowall et al., 1986), not highly ordered like 30-nm fibers (Finch and Klug, 1976). Our cryo-ET results here show that RPE-1 chromatin in both G1 and metaphase is also irregular. We did not observe 30-nm fibers, which have unmistakable dimensions and compact shapes in cryotomograms (Scheffer et al., 2011). The RPE-1 data reported here therefore adds to the growing list of *in situ* cryo-EM and cryo-ET studies in picoalgae, budding yeast, fission yeast, HeLa, T lymphoblast, colorectal adenocarcinoma, and fly neuron cells (Cai et al., 2018a; Cai et al., 2018b; Chen et al., 2016; Eltsov et al., 2018; Eltsov et al., 2008; Fatmaoui et al., 2022; Gan et al., 2013), which all report that frozen-hydrated eukaryotic chromatin packing is irregular *in situ*.

Recent studies of purified metaphase chromosomes proposed additional models of higher-order chromatin structure: metaphase chromatin plates in frozen-hydrated samples, in which nucleosomes are packed edge-to-edge in monolayers (plates), with interdigitation between adjacent plates (Chicano et al., 2019), and 100- to 200-nm periodic structures in fixed and heavy-metal-stained samples (Hayashida et al., 2021), in which the repeat direction is parallel to the chromatid long axis. Our metaphase-cell data did not show evidence of edge-to-edge packing or 100- to 200-nm periodic structures. The simplest explanation for these differences is from structural changes induced by sample preparation (isolated vs. *in situ* chromosomes). Our data does not rule out the alternative possibility in which the plates are irregular, with nucleosomes having large deviations relative to the ordered edge-to-edge arrangement depicted in

the earlier study. For the 100- to 200-nm periodic structures, we do not know alternative hypotheses to explain their absence in our – and others' – cryo-EM and cryo-ET data.

A cryo scanning transmission electron microscopy cryotomography study proposed another higher-order chromatin model that involves long-range ordered packing: sequential nucleosomes make a continuous stack in both interphase and mitosis (Sedat et al., 2022a; Sedat et al., 2022b). In this model, termed "slinky", the linker DNA follows a coiled path along stacks of consecutive nucleosomes akin to the hypernucleosomes of archaeal chromatin (Bowerman et al., 2021; Henneman et al., 2018), which was also seen in reconstituted telomere-like chromatin arrays (Soman et al., 2022). This slinky is proposed to coil into 100- to 300-nm gyruses, leaving a nucleosome-free tunnel in the middle. None of our class averages have the key feature needed for slinkies: linker DNA that is curved enough to connect to sequential nucleosomes in the stack. Furthermore, our cryotomograms do not show any large nucleosome-free regions in either the chromatin domains or metaphase chromosomes that would account for the hole in the middle of a slinky gyrus.

Non-nucleosome features of G1 nuclei and metaphase chromatin

We previously observed irregular intranuclear regions that we termed "pockets" in cryotomograms of *S. pombe* cells. Pockets are conspicuous because they lack macromolecular complexes and megacomplexes. In G1 chromatin domains, we did not find any instances of pockets, but we did find a few unambiguous ones in metaphase chromatin. With the exception of pockets, the RPE-1 metaphase chromatin distribution is uniform and resembles that seen in other cryo-EM and cryo-ET studies of mitotic human cells (Eltsov et al., 2008; Zhao and Jensen, 2022). We did not detect mesh/network-like nucleosome-free regions analogous to the "reticular pattern" of negatively stained cells in a previous study (Ou et al., 2017). Nevertheless, the presence of pockets in metaphase chromosomes suggests that the condensation is not maximized.

No megacomplexes were seen in the interior of the chromatin domains or mitotic chromatin, indicating that the crowding disfavors access by very large complexes. In contrast, mitotic budding and fission yeasts both have megacomplexes mixed with the chromatin (Cai et al., 2018b; Chen et al., 2016; Ng et al., 2019). This molecular-packing difference may be related to differences in mitotic transcription: both yeasts have high levels of mitotic transcription (Cho et al., 1998; Oliva et al., 2005; Peng et al., 2005; Rustici et al., 2004; Spellman et al., 1998) whereas mammalian chromatin undergoes genome-wide transcriptional repression (Flemming, 1880; Prescott and Bender, 1962; Taylor, 1960). Note that mammalian mitotic chromatin exhibits transient access to small complexes such as transcription factors (Teves et al., 2016) and permits very low levels of mitotic transcription (Palozola et al., 2017). Taken together with the known localization of G1 transcription at chromatin domain surfaces, the combined cryo-ET and fluorescence microscopy results confirm that eukaryotic transcription is inversely correlated with macromolecular crowding (Hilbert et al., 2021; Li et al., 2021; Miron et al., 2020; Nagashima et al., 2019; Nozaki et al., 2017).

The G1 nucleoplasm has many heterogeneous structures
Unlike the canonical-nucleosome-rich chromatin domains, the chromatin-poor G1 nucleoplasm is constitutionally heterogeneous. Our subtomogram analysis did not produce canonical nucleosome class averages in the nucleoplasm. There are at least two distinct possible explanations. If the nucleoplasmic nucleosomes have the canonical structure but too few, then the resultant class averages would be either too noisy to be recognizable as canonical nucleosomes or may be mis-classified. Alternatively, if the nucleoplasmic nucleosomes are abundant but have non-canonical structures, then we would miss them because we do not yet know their structures. The linker-filament structures remain to be determined (Li et al., 2021; Miron et al., 2020).

Nuclear bodies that are larger than nucleosomes are abundant in the nucleoplasm. The most conspicuous nucleoplasmic features are the megacomplexes, which have been seen in HeLa and yeast nuclei (Cai et al., 2018a; Cai et al., 2018b; Chen et al., 2016; Ng et al., 2019). Some of the megacomplexes are preribosomes because they have the expected size (~20 to 30 nm) (Erdmann et al., 2021; Lau et al., 2021). Indeed, we have detected one class average that resembles the large ribosomal subunit. The identities of the vast majority of megacomplexes remain to be determined.

The G1 nucleoplasm also contains dense irregular bodies, which have dimensions that exceed 40 nm. Dense irregular bodies are also present in our cryotomogram of an interphase HeLa cell (Cai et al., 2018a) and in *S. cerevisiae* cells (Ng et al., 2019), though we previously did not appreciate their differences from megacomplexes. No such bodies have been observed in *S. pombe* yet. Dense irregular bodies are too big to be preribosomes and are unlikely to harbor canonical nucleosomes because they lack the characteristic double-gyre motifs. Further work is needed to determine the identity of these dense irregular bodies and their relationship to megacomplexes (if any), diverse nuclear condensates that have been studied by light microscopy (Stanek and Fox, 2017; Zhu and Brangwynne, 2015), or ribonucleoprotein complexes (Pacheco-Fiallos et al., 2023).

Metaphase chromosome periphery
The metaphase chromosome's surface, termed the chromosome periphery, is associated with non-nucleosomal complexes such as nucleolar and ribosomal proteins and RNAs (Booth et al., 2016; Nishino et al., 2012; Ohta et al., 2010; Stenstrom et al., 2020). Ribosomes are present on the surface of metaphase chromosomes, reminiscent of those seen adjacent to HeLa and U2OS metaphase chromosomes *in situ* (Eltsov et al., 2008; Zhao and Jensen, 2022) and the ones that co-purify with isolated chromosomes (Nishino et al., 2012). The co-purified ribosomes generate a ~30-nm peak in small-angle X-ray scattering experiments that was previously (and erroneously) attributed to 30-nm chromatin fibers (Langmore and Paulson, 1983; Nishino et al., 2012). The chromosome periphery is organized by the proliferation marker Ki-67, which extends ~100 nm from the chromatin surface and keeps the chromosomes individualized via a surfactant function (Booth et al., 2014; Cuylen et al., 2016). Even though the Ki-67 protein (> 300 kDa) is more massive than a nucleosome (200 kDa) – much of its sequence is predicted to be intrinsically disordered (Remnant et al., 2021),

meaning that it has an extended structure. Long peptide-wide proteins are too thin to see in cryotomograms of cells, which would explain the absence of filamentous densities in chromosome-periphery regions of our cryotomograms. Instead, our cryotomograms show that the macromolecular contents of the nuclear periphery are both heterogeneous and lack order, consistent with the disordered nature of Ki-67.

Conclusions

Our study has revealed *in situ* similarities and differences of G1 and metaphase chromatin across multiple length scales (**Table 2**). Both G1 chromatin domains and metaphase chromosomes are densely packed with canonical nucleosomes and are largely devoid of megacomplexes. Canonical nucleosome class averages have variable ordered-linker-DNA lengths, though only G1 cells have a nucleosome class with ultra-short linker DNA. In both G1 and metaphase, a subset of canonical nucleosome classes has asymmetric linker DNA structure. Both G1 and metaphase chromatin have ordered stacked dinucleosomes classes, but no oligomers with more than two ordered nucleosomes. In detecting these ordered dinucleosomes, we show how to bootstrap a classification workflow to detect oligomers with ordered subunits. Remapping analysis has shown that the additional nucleosomes interact with both other nucleosomes and non-nucleosome complexes at their faces and gyres, and that these interactions are variable as evidenced in the absence of unambiguous class average densities. Metaphase canonical nucleosomes are uniformly distributed: there are no chromatin domains within, which raises the question of how condensation and decondensation proceed in terms of interphase chromatin domains. The structural cell-biology phenotypes presented here give multiple starting points for further nanoscale analysis and additional hypotheses about interphase and mitotic human nuclei and chromatin *in situ*.

MATERIALS AND METHODS

Cell culture

hTERT-RPE-1 cells (human retina epithelium cells immortalized with hTERT; CRL-4000™) were obtained from ATCC (Manassas, VA). The cells were grown in an incubator set to 37°C and 5% CO_2. The cells were cultured in complete medium consisting of DMEM/F-12 with GlutaMAX™ medium (Gibco, 10565-018; Thermo Fisher Scientific (TFS), Waltham, MA) supplemented with 10% fetal bovine serum (Sigma, F9665) and 1% penicillin-streptomycin (Pen-strep) (Gibco, 15140-122). Cell washing was done with PBS+Ca+Mg, consisting of Phosphate-buffered saline (PBS, Vivantis, PB0344-1L; Vivantis Technologies Sdn. Bhd., Selangor Darul Ehsan, Malaysia), 0.1 mg/mL $CaCl_2$ (Sigma, 12095), and 0.1 mg/mL $MgCl_2$ (Sigma, M8266-100G). Details of all the reagents and equipment used are summarized in **Table S1**.

Taxol-arrested cells for pilot experiments

Taxol-arrested cells were prepared following our previous work (Ruan et al., 2019). The cells were first synchronized in G1 as follows. Cells were seeded in culture flasks or dishes and incubated for 24 hours. They were then subject to depleted serum culturing for 24 hours. The cells were then further treated with 3mM thymidine for another 24 hours. To arrest the cells in mitosis, they were released from the thymidine block for 4 hours by replacement of fresh culture medium. Next, the cells were incubated with 800 µM Taxol for 12 hours. The mitotic cells were collected by shake-off.

G1 and metaphase cell-cycle arrest for both LM and cryo-ET of lamellae

The cell-cycle synchronization was done following a published protocol (Scott et al., 2020), with modifications. Adherent cells (destined for G1 arrest) were prepared differently for confocal microscopy versus cryo-ET. For confocal experiments, RPE-1 cells were seeded in a 35 mm µ-dish at a density of 4.8×10^5 cells/mL. After a 24-hour incubation, 1000× palbociclib (Selleckchem, S1116; Selleck Chemicals, Houston, TX), dissolved in 0.22 µm filtered Milli Q water, was added to the medium to a final concentration of 1 µM and then incubated for a further 18 hours. For cryo-ET experiments, gold grids were placed on the cover of a 35 mm Petri dish and exposed to UV light for 15 minutes in a biosafety cabinet. Then the gold grids were washed by incubating 10 minutes in complete medium + Pen-strep in a 35 mm dish, in a shaker at 20 RPM. The complete medium was then discarded and replaced with fresh medium. To arrest cells in G1 phase, RPE-1 cells were seeded in a 35 mm Petri dish where two gold grids were positioned in advance at a density of 2.0×10^5 cells/mL. After a 24-hour incubation, 1000× palbociclib was added to the medium to a final concentration of 1 µM and then followed by an 18-hour incubation. Then, the grids were picked up and immersed in DMEM/F-12 with GlutaMAX™ medium containing 9% DMSO (Sigma, 472301) for 5 seconds as cryoprotectant before plunge-freezing (see below).

Metaphase cells were synchronized the same way for all experiments (confocal microscopy, immunoblots, cryo-ET). RPE-1 cells were plated into a 25 cm^2 flask at a density of 8.0×10^4 cells/mL. After a 24-hour incubation, palbociclib was added to a final concentration of 1 µM and the cells were then incubated for 18 hours (as above). The

medium was then pipetted out and the cells were rinsed three times with 1 mL pre-warmed PBS+Ca+Mg. The cells were then cultured in fresh complete medium for 8 hours. Then nocodazole (Sigma, SML1665) (5 mg/mL stock in DMSO) was added into the medium to a final concentration of 50 ng/mL. After a 12-hour incubation, the cells were harvested by both shaking the flask and tapping it horizontally against the bench. Next, the cell suspension medium was washed four times by centrifugation at 1000 × *g* for 3 minutes, decanting the supernatant, and cell-pellet resuspension with 3 mL PBS+Ca+Mg. The last resuspension was done in complete culture medium with 10 μM MG132 (Sigma, M7449). After a 70-minute incubation, the cells were detached by shake off and flask tapping (see above), centrifuged at 1000 × *g* for 3 minutes. The cell pellet is used for the subsequent experiments.

Immunoblots

Both nocodazole- and MG132-arrested cells were prepared as above. Nocodazole-arrested cells were equally divided into four tubes, corresponding to: no washout and 30, 60, and 120 minutes after nocodazole washout. In a separate experiment, MG132-arrested cells were also equally divided into four tubes, corresponding to: no washout and, 30, 60, and 120 minutes after MG132 washout. The cell washes were done with PBST that was pre-warmed to 37°C in a water bath. Time zero of the nocodazole-washout experiment corresponds to when the first wash started. All cells were washed with ice-cold PBST before the addition of lysis buffer. Ice-cold protein extraction lysis buffer was composed of RIPA (Sigma, R0278), Protease inhibitor cocktail (Sigma, P8340) and Phosphatase Inhibitor Cocktail 3 (Sigma, P0044) with a volume ratio of 100:1:1. One hundred μL lysis buffer was added per 1.0×10^6 cells and mixed by vortexing for 6 seconds. In total, 5 vortex cycles were done with a 6 minute wait between each vortex. The lysate mixture was centrifuged at 16,000 × *g* for 20 minutes. The supernatant was aspirated into a clean tube and stored in −80°C until all groups were ready for total protein concentration determination via BCA assay (TFS, 23227). An equal volume of 2× Laemmli buffer was added into the cell lysates and mixed by vortexing briefly for less than 5 seconds. The mixture was boiled at 95°C for 5 minutes, then centrifuged at 16,000 × *g* for 5 minutes. The denatured protein mixture was divided into aliquots of about 20 μg for either immediate electrophoresis or storage in −80°C.

Twenty μg of protein was loaded in each well of a Mini-protean TGX gel (Bio-Rad 4561083; Hercules, CA) with Precision Plus Protein Dual Color Standards (Bio-Rad 1610374) or MagicMark™ XP Western Protein Standard (TFS, LC5602) as the protein ladder. Electrophoresis was done using constant voltage at 90 V for 30 minutes, followed by 120 V for another 30 minutes until the blue dye almost reached the bottom of the gel. The ladder and proteins in the gel were western transferred to the PVDF membrane (Bio-Rad 1704156) by the semi-dry method, with constant current 2.5 A for 3 minutes. The membrane was blocked in 1× TBST (Tris-buffered saline with 0.1% Tween 20) containing 5% nonfat milk at 23°C for 1 hour. Next, the membrane was rinsed with TBST for 5 seconds, then incubated with primary rabbit polyclonal antibody to beta tubulin (Abcam ab6046; Cambridge, United Kingdom), rabbit polyclonal anti-phospho-histone H3 (Ser10) antibody (Abcam, ab5176), or cyclin B1 (GNS1) mouse monoclonal IgG1 (Santa Cruz, sc-245; Dallas, TX) overnight at 4°C. All antibodies were diluted

1:500 in blocking buffer. After three sequential 5-minute washes with TBST, the membrane previously incubated with anti-Cyclin B1 antibody was incubated with m-IgGκ BP-HRP secondary antibody (Santa Cruz, sc-516102) for 1 hour at 23°C, and membranes previously incubated with anti-beta tubulin antibody or anti-phospho-histone H3 (Ser10) antibody were incubated with mouse anti-rabbit IgG-HRP secondary antibody (Santa Cruz, sc-2357) for 1 hour at 23°C. After 3 sequential 5-minute washes in TBST, the membranes were incubated with Clarity Western ECL substrate solution (Bio-Rad 1705061) at 23°C for 5 minutes, then imaged with ImageQuant LAS4000 system (Cytiva, Marlborough, MA). Full, uncropped blots are shown in **Figure S24**. A summary of all the antibodies used is in **Table S2**.

Conventional fluorescence microscopy

For morphological analysis, RPE-1 cells were imaged using a Nikon Eclipse Ti microscope (Nikon Instruments Inc., Tokyo, Japan) equipped with a Plan Fluor 10× Ph1 objective lens. To obtain fields of view of multiple cells, Z-stack images were acquired on an LSM 900 AiryScan microscope controlled by ZEN 3.1 software, using a 20× 0.8 NA Plan-Apochromat under confocal mode (Zeiss, Jena, Germany). Z-projection at maximum intensity was done in FIJI (Schindelin et al., 2012).

Immunofluorescence

All washes were done as follows. Attached cells were washed 3 times with PBST (PBS+Ca+Mg with 0.1% Tween 20 (Sinopharm, T20087687, Beijing, China)) for 5 minutes on a shaker at 20 RPM. Suspended cells were washed 3 times with PBST for 5 minutes, except the first wash after fixation (see fixation protocol below), in which PBST was replaced with PBST containing 0.5% BSA (Sigma, A9647). For each wash, the suspended cells were centrifuged at 600 × *g* for 3 minutes, then supernatant was decanted, the cell pellet was resuspended with 1 mL PBST using a P1000 micropipette, and then incubated 2 minutes on a rotator at 20 RPM.

Palbociclib-synchronized G1 (attached) cells were washed three times with PBS+Ca+Mg after the completion of the drug treatment. The cells were then fixed with 4% paraformaldehyde (Electron Microscopy Sciences, 15714, Hatfield, PA) in PBS for 10 minutes at 23°C, then washed 3 times for 5 minutes each in PBST, then permeabilized with 0.25% Triton X-100 (TFS, Alfa Aesar A16046) in PBS for 10 minutes at 23°C. To block non-specific binding, the cells were then washed 3 × 5 minutes with PBST, then incubated with PBST containing 1% BSA and 22.5 mg/mL glycine (Bio-Rad 1610718) for 30 minutes at 23°C. Next, the cells were immunostained with primary antibodies: rabbit polyclonal to RNAPII CTD repeat YSPTSPS (phospho S2) (1:300, Abcam ab5095), rabbit polyclonal to RNAPII CTD repeat YSPTSPS (phospho S5) (1:300, Abcam ab5131)), or Alexa Fluor-conjugated antibody (Alexa Fluor® 647) mouse monoclonal anti-histone H3 (phospho S10) antibody (1:250, Abcam ab196698)), in PBST with 1% BSA, on a rotator with slow rotation, overnight at 4°C. The cells were then incubated with Alexa Fluor 488 goat anti-rabbit IgG (H+L) secondary antibody (1:500, TFS A-11008) in Milli Q purified water containing 1% BSA for 1 hour at 23°C. Finally, the cells were incubated with 300 nM 4′,6-diamidino-2-phenylindole (DAPI, TFS

D1306) in PBS for 5 minutes. After three sequential 5-minute washes with PBST, the cells were ready for imaging.

To harvest nocodazole- and MG132-arrested cells after the completion of the drug treatment, the flasks were shaken and tapped against the bench. The detached cells were collected in a 15 mL tube and centrifuged at 600 × *g* for 3 minutes. Cell pellets were resuspended with 1 mL PBST and transferred to a 1.5 mL microfuge tube for all following incubations and washes, which are different from the G1 cells (attached to the dish). After the last wash before imaging, most of the supernatant was removed, leaving about 20 µL. The cell pellets were resuspended in this remaining supernatant with a micropipette using a 200 µL tip. Finally, 5 µL of this cell suspension was mounted on a 20 mm Ø coverslip (Paul Marienfeld GmbH & Co. KG, 0112600, Lauda-Königshofen, Germany) with 15 µL Prolong Gold antifade reagent and then cured 20 to 24 hours prior to imaging. All treatments between the harvesting and blocking steps were done in 15 mL conical tubes. After blocking, the washing was done in 1.5 mL microfuge tubes. All reagents including their concentrations and incubation durations were the same as above G1 cells.

To obtain a large field of view containing multiple cells, Z-stacks were acquired with a Zeiss LSM 900 confocal microscope (see above). To observe details of single cells, Z-stacks were acquired with the same microscope, but using a 63× 1.4 NA Plan-Apochromat oil-immersion objective and operated in Airyscan super-resolution mode. Z-stacks (3-D) were projected using Fiji's "3D Project" brightest point method. All the confocal microscopy details are summarized in **Table S3**.

Self-pressurized freezing

Taxol-treated RPE-1 cells were scraped or shaken off in 1× PBS. The cells were further pelleted by centrifugation at 600 × *g* for 10 minutes. For 100 µL cell pellets, 25 µL 50% w/v dextran 6000 (Sigma 31388) was added and mixed gently as the extracellular cryoprotectant, yielding a final concentration of 12.5% dextran. The cells were loaded into copper tubes, which were sealed and then dropped into liquid ethane for self-pressurized freezing.

Vitreous sectioning

Cryomicrotomy was done in an UC7/FC7 cryomicrotome (Leica Microsystems, Vienna, Austria). RPE-1 cells were cut into 100-nm-thick (nominal) cryosections using a 35° diamond knife (Diatome Cryo35, Nidau, Switzerland). We used the dual-micromanipulator method (Ladinsky et al., 2006; Ng et al., 2020; Studer et al., 2014). The cryosections were attached to a continuous carbon grid (EMS CF200-Cu-UL, Hatfield, PA) using a Crion device (Leica) in "charge" mode.

Plunge-freezing of oligonucleosomes

HeLa oligonucleosomes (EpiCypher 16-0003, Durham, NC; sold as "polynucleosomes") in storage buffer (20 mM HEPES, pH 7.5, 1 mM EDTA) was diluted 1:1 in a buffer containing 20 mM HEPES-KOH, pH 7.8, 2 mM $MgCl_2$. The additional $MgCl_2$ was added to keep the oligonucleosomes slightly condensed to facilitate targeting but was of

insufficient concentration; since the same $MgCl_2$-containing buffer was used in all the cryoprotectant test samples, the conclusions were independent of $MgCl_2$. For preparations containing cryoprotectant, the sample was also supplemented with DMSO to a final concentration of 9% (v/v). Each glow-discharged Quantifoil R2/4 200 mesh copper grid (Quantifoil Micro Tools GmbH, Jena, Germany) was then deposited with 4 µL sample and plunge-frozen in liquid ethane using a Vitrobot Mark IV (TFS) operated at 22°C and 100% humidity.

Plunge-freezing of RPE-1 cells

RPE-1 cells were plunge-frozen in 63/37 propane-ethane mixture (Tivol et al., 2008) using a Vitrobot Mark IV (TFS) operated at 100% humidity and 37°C. For G1-arrested RPE-1 cells that were grown on a C-flat 2/4 200 mesh gold grid (Protochips, Morrisville, NC), the grid was held with a Vitrobot tweezer and then immersed for 5 seconds in DMEM/F12 with GlutaMAX™ medium that was supplemented with 9% DMSO as cryoprotectant. The grid was then loaded on the Vitrobot and manually blotted from the back using Whatman® Grade 1 filter paper before being plunge-frozen. Metaphase-arrested RPE-1 cells were first harvested as a suspension and concentrated to 1.5×10^6 cells/mL. Immediately before plunge freezing, the cell suspension was mixed with an equal volume of fresh DMEM/F12 with GlutaMAX™ medium containing 18% DMSO, bringing the final DMSO concentration to 9%. C-flat 2/4 200 mesh gold grids (without any coatings) were glow discharged at 15 mA for 15 seconds, and then deposited with 4 µL of the sample, before being manually back-blotted and plunge-frozen as described above.

Cryo-FIB milling

Cryolamellae of plunge-frozen RPE-1 cells were prepared using a Helios NanoLab 600 DualBeam (TFS) equipped with a PolarPrep 2000 Cryo Transfer System (Quorum Technologies, Laughton, UK) (Medeiros et al., 2018). The samples were first coated with a layer of organometallic platinum using an in-chamber gas injection system that was positioned 9 mm from the grid center and operated for approximately 10 to 18 seconds flow time at 28°C (Hayles et al., 2007). Cryo-FIB milling was then performed with the Helios stage tilted to 12°. The bulk of the cellular material was first removed using the FIB at 30 kV 2.8 nA, followed by further thinning of the cryolamellae at a lower current of 0.28 nA. The cryolamellae were then polished to a final nominal thickness of ~150 nm at 48 pA.

Electron cryotomography

A summary of the cryo-ET sample preparation, imaging, and processing parameters are reported in **Table S4**. Additional details of each tilt series are reported in **Table S5**. Cryo-ET data of both RPE-1 cryolamellae and purified HeLa oligonucleosome samples were collected using SerialEM (Mastronarde, 2005) on a Titan Krios (TFS) equipped with a K3 camera (AMETEK, Berwyn, PA) and a BioContinuum energy filter (AMETEK) operating in zero-loss mode with a 20 eV slit width. Tilt series were acquired in super-resolution mode with a bin ×1 pixel size of 3.4 Å at the specimen level. These data were collected in the dose-symmetric tilt scheme and using either defocus phase contrast at −5 µm defocus or Volta phase contrast at −0.5 µm defocus (both nominal values). The

K3 data was collected after TFS changed their Volta phase plate design, requiring that the phase-plate heater be operated at ~370 mW power.

To speed up the setup of the tilt series collection on SerialEM, we used the Python scripts described by Weis *et. al* (Weis et al., 2021) to generate virtual maps of regions of interest from low-magnification montage images of cryolamellae or grid squares. HeLa oligonucleosome samples were imaged using a tilt range of ±60° and a tilt increment of 2°, for a nominal total dose of 120 $e^-/Å^2$ per tilt series. For cryolamellae samples, a stage pre-tilt of −14° was applied so that the cryolamellae are approximately perpendicular to the electron-optical axis when the first image is recorded. This pre-tilt angle was determined by trial-and-error. Cryolamellae tilt series were collected using a tilt range of −70° to +42° and a 2° tilt increment. The nominal total dose per tilt series for cryolamellae samples was 110 $e^-/Å^2$.

To more accurately target regions of interest for cryolamellae imaging, we first generated longer exposure (~0.1 $e^-/Å^2$ per tile) low-magnification montage images of our samples. Montage tiles were acquired at −90 µm defocus using an unbinned pixel size of 19.2 Å (4,800× magnification) and a 2-second exposure time. In this imaging condition, chromosome regions and cytoplasm of metaphase-arrested RPE-1 cells show different density features (**Figure S18**). Microtubules are also frequently seen surrounding the chromosome regions. For G1-arrested cells, nuclear regions were identified based on cytological cues. The nucleus periphery regions were found based on the presence of the nuclear envelope. If the nuclear envelope was not visible, imaging positions were selected based on the absence of the cytoplasmic components listed above.

Super-resolution movie frames were aligned and Fourier cropped to 3.4 Å pixel size using MotionCor2 (Zheng et al., 2017). Tilt series stacks were aligned by patch tracking and reconstructed into cryotomograms at 6.8 Å voxel size using the IMOD program *Etomo* (Kremer et al., 1996; Mastronarde, 1997; Mastronarde and Held, 2017). All subsequent template matching and subtomogram analyses were performed using cryotomograms at 6.8 Å voxel size. For visualization purposes, cryotomographic slices shown in **Figures 2, 3, 4 and 5** were denoised using cryo-CARE (Buchholz et al., 2019).

Automated segmentation of chromatin regions in the cryotomograms was performed using EMAN2 (Chen et al., 2017). For the convolutional neural network training, 64 x 64 tiles containing either G1 chromatin domains or metaphase chromosome regions were extracted from the cryotomograms (binned to a voxel size of 13.5 Å) and used as positive training examples. Tiles from the cytoplasm, nucleoplasm and lamella surface contaminants were used as negative examples.

For the cryosection pilot experiments, both defocus phase-contrast and Volta phase contrast tilt series were collected using the same Titan Krios as above, but with a Falcon II camera (TFS) in integration mode at a 12.4 or 7.3 Å pixel size as the specimen level, all controlled with Tomo4 (TFS). A nominal defocus of −10 µm (defocus phase

contrast) or −0.5 µm (VPP) was applied. Bi-directional tilt series, starting at 0°, were collected with a ±60° tilt range and 2° tilt increment. These data were collected before TFS implemented a change in Volta phase plate design, so the phase-plate heater was operated at lower than 150 mW power.

Denoising for visualization

A subset of cryotomograms were denoised for visualization purposes; the subtomogram analysis steps in the following sections were done on non-denoised data. MotionCor2 was used to generate tilt series images where either the odd- or even-numbered raw movie frames was excluded. The odd- and even-frames only tilt series stacks were then reconstructed at 6.8 Å voxel size in IMOD and used as the input for denoising in cryo-CARE (Buchholz et al., 2019). The default parameters were used for cryo-CARE, with the exception of the "n_tiles" value in the prediction settings which was changed to 5. All cryotomogram slices shown in **Figures 2 – 5** were created from denoised data. A copy of these figures was also created using non-denoised data and can be found as **Figures S25 – S28**.

Template matching

Candidate nucleosome subtomograms were picked from bin ×2 cryotomograms (6.8 Å pixel size; low-pass filtered using *mtffilter* with mean and sigma values of 0.17 and 0.05, respectively, with the roll-off starting at 40 Å resolution) by template matching using the PEET package (Heumann, 2023; Heumann et al., 2011; Nicastro et al., 2006). A featureless soft-edged cylinder ~10 nm diameter and ~5.5 nm tall was generated as the template-matching reference using the Bsoft program *beditimg* (Heymann, 2022). Cryotomograms of interest were seeded with a grid of points (from which translational searches initialize) that were spaced ~7 nm apart using the PEET program *gridInit*. For efficiency, we excluded seeded points that were located outside chromatin domains or metaphase chromosome regions by using the segmented version of the cryotomograms as masks. At the end of the PEET template matching run, duplicate removal was performed on the candidate points, with a distance threshold of ~5.5 nm.

Globular complexes such as ribosomes and preribosomes were picked using PEET, as described above with three differences: 1) A featureless sphere of ~24 nm diameter was used as the reference. 2) The initial grid of points seeded were ~21 nm apart. 3) Duplicate removal was performed with a 13.5 nm distance threshold.

The coordinates of the template matching subtomograms (candidate nucleosomes/ribosomes/preribosomes) were then exported to RELION for subtomogram averaging, classification, and refinement. The remaining “junk” subtomograms were excluded at the end of each classification run.

Subtomogram analysis of mononucleosomes

Classification and subtomogram averaging were performed using RELION 3 (Kimanius et al., 2016; Zivanov et al., 2018). A summary of the workflow is shown in **Figures S12 and S20**. 64×64×64 voxel subtomograms corresponding to the template-matching coordinates in PEET were extracted in RELION and subjected to 3-D classification. To

analyze for mononucleosomes, the subtomograms were classified using a featureless cylinder as the reference and a 110 Å-diameter spherical mask (**Figures S12A & S20A**).

To analyze for ordered stacked dinucleosomes, the same set of extracted subtomograms from the mononucleosome PEET run were subjected to 3-D classification, using a double-stacked featureless cylinder as the reference and a larger 240 Å-diameter spherical mask. The resulting nucleosome classes from the double-cylinder 3-D classification run were selected and subjected to a second round of 3-D classification, where an ordered stacked dinucleosome class was observed (**Figures S12 & S20, B & C**). In an attempt to pick up more nucleosome particles, the original set of extracted subtomograms were again subjected to 3-D classification, this time using the ordered stacked dinucleosome average as the reference, low-pass filtered to 60 Å in RELION (**Figures S12D & S20D**). Nucleosome averages from this classification run were manually placed into three groups: 1) mononucleosomes; 2) ordered stacked dinucleosomes; and 3) mononucleosomes with an additional proximal density. Subtomograms from each of these three groups were subjected to a second round of 3-D classification separately (**Figures S12E & S20E**). For Group 1, the resulting mononucleosome classes were manually separated into two further groups corresponding to the presence of either short or long linker DNA densities and then subjected to 3-D refinement separately. 3-D classification for Group 2 resulted in several ordered stacked dinucleosome classes, which were refined as a single group. For Group 3, we detected several mononucleosome classes with an additional density at different positions around the DNA gyres. Each of these Group 3 classes were subjected to separate 3-D refinements (**Figures S13 and S21**). The details are summarized in **Table S6 and S7**.

Subtomogram analysis of other nucleosome and multi-nucleosome structures
To detect the presence of ordered side-by-side dinucleosomes and stacked tri-/tetra-nucleosomes, further 3-D classification was performed on the nucleosome particles in Groups 2 and 3 (**Figures S13 and S21**, panels B and C), respectively. Custom masks were generated to include the nucleosome densities seen in the subtomogram averages; and to enclose additional volume where we anticipate more nucleosomes may be found. **Figures S14 and S22** show a rendering of the reference and mask combination used for each of the 3-D classification runs. These custom masks were created in UCSF Chimera (Pettersen et al., 2004) by manually positioning multiple featureless cylinders of 15 nm-diameter and 10 nm-height, and then combining them into a single volume using the following Chimera commands:

```
vop new empty size 64 gridSpacing 6.766
vop maximum [cyl #1] [cyl #2] [cyl #3] onGrid [empty #]
```

The multi-cylinder masks' edges were then smoothed by Gaussian filtering:

```
vop gaussian [combined cylinder #] sDev 67.66
```

References used during these 3-D classification runs were subtomogram averages generated during the refinement step from either Group 2 or 3, all low-pass filtered to 60

Å in RELION. The angular search range was restricted to ±15° for these 3-D classification runs.

Subtomogram analysis of ribosomes and preribosomes
Template matching hits for candidate ribosomes in the cytoplasm were subjected to direct 3-D classification using a 24-nm-diameter sphere as a reference. The unambiguous ribosome class averages were pooled and then subjected to refinement. For preribosome subtomogram averaging, template matching hits from both the nuclear region and the cytoplasm was included during RELION classification. Candidate preribosomes were first 2-D classified, whereupon classes that did not have large complexes were removed. Next, 3-D classification was performed on the remaining particles, using the refined ribosome class average generated in the previous step as a reference. An initial low-pass filter of 60 Å was applied to the ribosome reference in RELION, during the 3-D classification run.

Docking of nucleosome crystal structures
The docking of nucleosome crystal structures into our refined subtomogram averages was performed using UCSF Chimera. The nucleosome crystal structure (PDB 1AOI) (Luger et al., 1997) was docked into nucleosome subtomogram averages that have short linker DNAs. The chromatosome crystal structure (PDB 5NL0) (Garcia-Saez et al., 2018) was docked into subtomogram averages with longer linker DNAs. The histone tails were removed from the atomic models prior to docking into our subtomogram averages. Briefly, the corresponding atomic model was manually aligned into the subtomogram average, and then the fit-in-map function was executed. For the fit-in-map function, the option to simulate a density map from the atomic model at 20 Å was used.

For the stacked dinucleosome averages, the Chimera “hide dust” function was used to hide the nucleosome density with the shorter linker DNA. PDB 5NL0 was then fitted to the remaining visible nucleosome. The hidden nucleosome density was next rendered visible using the command “`sop invertShown`”, and then docked by PDB 1AOI. For the mononucleosome subtomogram averages that have an additional proximal density, PDB 1AOI was fitted to the nucleosome region, with the proximal density still rendered.

The fitting correlation coefficients for the G1 nucleosomes subtomogram averages were as follows: mononucleosome, short linker = 0.78; mononucleosome, long linker = 0.78; stacked dinucleosome, nucleosome 1 = 0.71; stacked dinucleosome, nucleosome 2 = 0.67; nucleosome with proximal densities = 0.65 – 0.73. For the metaphase nucleosome subtomogram averages: mononucleosome, short linker = 0.77; mononucleosome, long linker = 0.77; stacked dinucleosome, nucleosome 1 = 0.68; stacked dinucleosome, nucleosome 2 = 0.66; nucleosome with proximal densities = 0.70 – 0.72.

Simulation of ribosome densities
Coordinates for the single-particle reconstruction of human ribosomes (PDB 4UG0) (Khatter et al., 2015) were used as input for density map simulations. The EMAN2 program *e2pdb2mrc.py* was used to create an .mrc file using the following command:

```
e2pdb2mrc.py --apix 6.766 --box 64 --res [res] --center 4UG0.pdb
4UG0.mrc
```
The option [res] corresponds to the resolution of the output map. Three maps were created, covering resolutions (25 – 35Å) typical of averages of the order of ~1,000 subtomograms, such as the one obtained from the G1 cell cryotomograms.

Remapping
Remapping of nucleosome, ribosome, and preribosome particles was performed using a custom python script *ot_remap_v2.py* (available at https://github.com/anaphaze/ot-tools). The coordinate and orientation information for each particle from the RELION refined .star files was imposed on the corresponding subtomogram average, which was then written into a new .mrc file. Remapped models were visualized using UCSF Chimera.

Data sharing
A copy of all the tilt series raw data and cryotomograms presented in this paper (**Table S5**) was deposited in EMPIAR (Iudin et al., 2016) as EMPIAR-#####. Subtomogram averages of the RPE-1 nucleosomes, dinucleosomes, nucleosomes with gyre-proximal densities (**Figures 3A – C and 5A – C**), cytoplasmic ribosomes (**Figure S9B**), and preribosomes (**Figure S10B**) have been deposited at EMDB. The EMD serial numbers are shown in **Tables S6 – S8**.

Contributions
JC, TL, SC, WR, CTN - experiments, project design, writing; US - project design, writing; JS - training; LG - project design, writing, training.

ACKNOWLEDGEMENTS
We thank the CBIS microscopy staff for support and training. We thank Paulo D'Avino for advice on RPE-1 synchronization. JC, TL, and LG were supported by a Singapore Ministry of Education grant MOE2019-T2-1-140. WR and US were funded by the Biomedical Research Council of A*STAR (Agency for Science, Technology and Research), Singapore.

REFERENCES

Arimura, Y., R.M. Shih, R. Froom, and H. Funabiki. 2021. Structural features of nucleosomes in interphase and metaphase chromosomes. *Mol Cell*. 81:4377-4397 e4312.

Armache, J.P., N. Gamarra, S.L. Johnson, J.D. Leonard, S. Wu, G.J. Narlikar, and Y. Cheng. 2019. Cryo-EM structures of remodeler-nucleosome intermediates suggest allosteric control through the nucleosome. *Elife*. 8.

Bacic, L., G. Gaullier, A. Sabantsev, L.C. Lehmann, K. Brackmann, D. Dimakou, M. Halic, G. Hewitt, S.J. Boulton, and S. Deindl. 2021. Structure and dynamics of the chromatin remodeler ALC1 bound to a PARylated nucleosome. *Elife*. 10.

Baker, R.W., J.M. Reimer, P.J. Carman, B. Turegun, T. Arakawa, R. Dominguez, and A.E. Leschziner. 2021. Structural insights into assembly and function of the RSC chromatin remodeling complex. *Nat Struct Mol Biol*. 28:71-80.

Barth, R., K. Bystricky, and H.A. Shaban. 2020. Coupling chromatin structure and dynamics by live super-resolution imaging. *Sci Adv*. 6.

Bäuerlein, F.J.B., J.C. Pastor-Pareja, and R. Fernández-Busnadiego. 2022. Cryo-electron tomography of native Drosophila tissues vitrified by plunge freezing. *bioRxiv*.

Bednar, J., I. Garcia-Saez, R. Boopathi, A.R. Cutter, G. Papai, A. Reymer, S.H. Syed, I.N. Lone, O. Tonchev, C. Crucifix, H. Menoni, C. Papin, D.A. Skoufias, H. Kurumizaka, R. Lavery, A. Hamiche, J.J. Hayes, P. Schultz, D. Angelov, C. Petosa, and S. Dimitrov. 2017. Structure and Dynamics of a 197 bp Nucleosome in Complex with Linker Histone H1. *Mol Cell*. 66:384-397 e388.

Bednar, J., R.A. Horowitz, S.A. Grigoryev, L.M. Carruthers, J.C. Hansen, A.J. Koster, and C.L. Woodcock. 1998. Nucleosomes, linker DNA, and linker histone form a unique structural motif that directs the higher-order folding and compaction of chromatin. *Proc Natl Acad Sci U S A*. 95:14173-14178.

Beel, A.J., M. Azubel, P.J. Mattei, and R.D. Kornberg. 2021. Structure of mitotic chromosomes. *Mol Cell*. 81:4369-4376 e4363.

Bilokapic, S., M. Strauss, and M. Halic. 2018. Cryo-EM of nucleosome core particle interactions in trans. *Sci Rep*. 8:7046.

Booth, D.G., A.J. Beckett, O. Molina, I. Samejima, H. Masumoto, N. Kouprina, V. Larionov, I.A. Prior, and W.C. Earnshaw. 2016. 3D-CLEM Reveals that a Major Portion of Mitotic Chromosomes Is Not Chromatin. *Mol Cell*. 64:790-802.

Booth, D.G., M. Takagi, L. Sanchez-Pulido, E. Petfalski, G. Vargiu, K. Samejima, N. Imamoto, C.P. Ponting, D. Tollervey, W.C. Earnshaw, and P. Vagnarelli. 2014. Ki-67 is a PP1-interacting protein that organises the mitotic chromosome periphery. *Elife*. 3:e01641.

Bowerman, S., J. Wereszczynski, and K. Luger. 2021. Archaeal chromatin 'slinkies' are inherently dynamic complexes with deflected DNA wrapping pathways. *Elife*. 10.

Buchholz, T.-O., A. Krull, R. Shahidi, G. Pigino, G. Jékely, and F. Jug. 2019. Content-aware image restoration for electron microscopy. *In* Methods in Cell Biology. Vol. 152. T. Müller-Reichert and G. Pigino, editors. Academic Press. 277-289.

Cai, S., D. Böck, M. Pilhofer, and L. Gan. 2018a. The in situ structures of mono-, di-, and trinucleosomes in human heterochromatin. *Mol Biol Cell*. 29:2450-2457.

Cai, S., C. Chen, Z.Y. Tan, Y. Huang, J. Shi, and L. Gan. 2018b. Cryo-ET reveals the macromolecular reorganization of S. pombe mitotic chromosomes in vivo. *Proc Natl Acad Sci U S A*. 115:10977-10982.

Cai, S., Y. Song, C. Chen, J. Shi, and L. Gan. 2018c. Natural chromatin is heterogeneous and self-associates in vitro. *Mol Biol Cell*. 29:1652-1663.

Cai, S., Z.Y. Tan, X. Nie, J. Shi, and L. Gan. 2020. Macromolecular and biochemical changes of G0 fission yeast nuclei. *bioRxiv*.

Cai, S., Y. Wu, A. Guillen-Samander, W. Hancock-Cerutti, J. Liu, and P. De Camilli. 2022. In situ architecture of the lipid transport protein VPS13C at ER-lysosome membrane contacts. *Proc Natl Acad Sci U S A*. 119:e2203769119.

Chen, C., H.H. Lim, J. Shi, S. Tamura, K. Maeshima, U. Surana, and L. Gan. 2016. Budding yeast chromatin is dispersed in a crowded nucleoplasm in vivo. *Mol Biol Cell*. 27:3357-3368.

Chen, M., W. Dai, S.Y. Sun, D. Jonasch, C.Y. He, M.F. Schmid, W. Chiu, and S.J. Ludtke. 2017. Convolutional neural networks for automated annotation of cellular cryo-electron tomograms. *Nature methods*. 14:983-985.

Chen, Q., L. Zhao, A. Soman, A.Y. Arkhipova, J. Li, H. Li, Y. Chen, X. Shi, and L. Nordenskiold. 2022a. Chromatin Liquid-Liquid Phase Separation (LLPS) Is Regulated by Ionic Conditions and Fiber Length. *Cells*. 11.

Chen, X., X. Wang, W. Liu, Y. Ren, X. Qu, J. Li, X. Yin, and Y. Xu. 2022b. Structures of +1 nucleosome-bound PIC-Mediator complex. *Science*. 378:62-68.

Chicano, A., E. Crosas, J. Oton, R. Melero, B.D. Engel, and J.R. Daban. 2019. Frozen-hydrated chromatin from metaphase chromosomes has an interdigitated multilayer structure. *EMBO J*. 38.

Chittori, S., J. Hong, Y. Bai, and S. Subramaniam. 2019. Structure of the primed state of the ATPase domain of chromatin remodeling factor ISWI bound to the nucleosome. *Nucleic Acids Res*. 47:9400-9409.

Cho, N.H., K.C. Cheveralls, A.D. Brunner, K. Kim, A.C. Michaelis, P. Raghavan, H. Kobayashi, L. Savy, J.Y. Li, H. Canaj, J.Y.S. Kim, E.M. Stewart, C. Gnann, F. McCarthy, J.P. Cabrera, R.M. Brunetti, B.B. Chhun, G. Dingle, M.Y. Hein, B. Huang, S.B. Mehta, J.S. Weissman, R. Gomez-Sjoberg, D.N. Itzhak, L.A. Royer, M. Mann, and M.D. Leonetti. 2022. OpenCell: Endogenous tagging for the cartography of human cellular organization. *Science*. 375:eabi6983.

Cho, R.J., M.J. Campbell, E.A. Winzeler, L. Steinmetz, A. Conway, L. Wodicka, T.G. Wolfsberg, A.E. Gabrielian, D. Landsman, D.J. Lockhart, and R.W. Davis. 1998. A genome-wide transcriptional analysis of the mitotic cell cycle. *Mol Cell*. 2:65-73.

Collepardo-Guevara, R., and T. Schlick. 2014. Chromatin fiber polymorphism triggered by variations of DNA linker lengths. *Proc Natl Acad Sci U S A*. 111:8061-8066.

Cuylen, S., C. Blaukopf, A.Z. Politi, T. Muller-Reichert, B. Neumann, I. Poser, J. Ellenberg, A.A. Hyman, and D.W. Gerlich. 2016. Ki-67 acts as a biological surfactant to disperse mitotic chromosomes. *Nature*. 535:308-312.

Danev, R., B. Buijsse, M. Khoshouei, J.M. Plitzko, and W. Baumeister. 2014. Volta potential phase plate for in-focus phase contrast transmission electron microscopy. *Proc Natl Acad Sci U S A*. 111:15635-15640.

Dodonova, S.O., F. Zhu, C. Dienemann, J. Taipale, and P. Cramer. 2020. Nucleosome-bound SOX2 and SOX11 structures elucidate pioneer factor function. *Nature*. 580:669-672.

Dombrowski, M., M. Engeholm, C. Dienemann, S. Dodonova, and P. Cramer. 2022. Histone H1 binding to nucleosome arrays depends on linker DNA length and trajectory. *Nat Struct Mol Biol*. 29:493-501.

Dubochet, J., M. Adrian, J.J. Chang, J.C. Homo, J. Lepault, A.W. McDowall, and P. Schultz. 1988. Cryo-electron microscopy of vitrified specimens. *Quarterly reviews of biophysics*. 21:129-228.

Dubochet, J., and M. Noll. 1978. Nucleosome arcs and helices. *Science*. 202:280-286.

Ehara, H., T. Kujirai, Y. Fujino, M. Shirouzu, H. Kurumizaka, and S.I. Sekine. 2019. Structural insight into nucleosome transcription by RNA polymerase II with elongation factors. *Science*. 363:744-747.

Ehara, H., T. Kujirai, M. Shirouzu, H. Kurumizaka, and S.I. Sekine. 2022. Structural basis of nucleosome disassembly and reassembly by RNAPII elongation complex with FACT. *Science*. 377:eabp9466.

Ekundayo, B., T.J. Richmond, and T. Schalch. 2017. Capturing Structural Heterogeneity in Chromatin Fibers. *J Mol Biol*. 429:3031-3042.

Eltsov, M., D. Grewe, N. Lemercier, A. Frangakis, F. Livolant, and A. Leforestier. 2018. Nucleosome conformational variability in solution and in interphase nuclei evidenced by cryo-electron microscopy of vitreous sections. *Nucleic Acids Res*.

Eltsov, M., K.M. MacLellan, K. Maeshima, A.S. Frangakis, and J. Dubochet. 2008. Analysis of cryo-electron microscopy images does not support the existence of 30-nm chromatin fibers in mitotic chromosomes in situ. *Proceedings of the National Academy of Sciences*. 105:19732-19737.

Erdmann, P.S., Z. Hou, S. Klumpe, S. Khavnekar, F. Beck, F. Wilfling, J.M. Plitzko, and W. Baumeister. 2021. In situ cryo-electron tomography reveals gradient organization of ribosome biogenesis in intact nucleoli. *Nat Commun*. 12:5364.

Eustermann, S., K. Schall, D. Kostrewa, K. Lakomek, M. Strauss, M. Moldt, and K.P. Hopfner. 2018. Structural basis for ATP-dependent chromatin remodelling by the INO80 complex. *Nature*. 556:386-390.

Fang, K., X. Chen, X. Li, Y. Shen, J. Sun, D.M. Czajkowsky, and Z. Shao. 2018. Super-Resolution Imaging of Individual Human Sub-Chromosomal Regions In Situ Reveals Nanoscopic Building Blocks of Higher-Order Structure. *ACS Nano*.

Farnung, L., M. Ochmann, and P. Cramer. 2020. Nucleosome-CHD4 chromatin remodeler structure maps human disease mutations. *Elife*. 9.

Farnung, L., M. Ochmann, M. Engeholm, and P. Cramer. 2021. Structural basis of nucleosome transcription mediated by Chd1 and FACT. *Nat Struct Mol Biol*. 28:382-387.

Farnung, L., M. Ochmann, G. Garg, S.M. Vos, and P. Cramer. 2022. Structure of a backtracked hexasomal intermediate of nucleosome transcription. *Mol Cell*. 82:3126-3134 e3127.

Farnung, L., S.M. Vos, and P. Cramer. 2018. Structure of transcribing RNA polymerase II-nucleosome complex. *Nat Commun*. 9:5432.

Farnung, L., S.M. Vos, C. Wigge, and P. Cramer. 2017. Nucleosome-Chd1 structure and implications for chromatin remodelling. *Nature*. 550:539-542.

Fatmaoui, F., P. Carrivain, D. Grewe, B. Jakob, J.-M. Victor, A. Leforestier, and M. Eltsov. 2022. Cryo-electron tomography and deep learning denoising reveal native chromatin landscapes of interphase nuclei. *bioRxiv*.

Finch, J.T., and A. Klug. 1976. Solenoidal model for superstructure in chromatin. *Proc Natl Acad Sci U S A*. 73:1897-1901.

Finogenova, K., J. Bonnet, S. Poepsel, I.B. Schafer, K. Finkl, K. Schmid, C. Litz, M. Strauss, C. Benda, and J. Muller. 2020. Structural basis for PRC2 decoding of active histone methylation marks H3K36me2/3. *Elife*. 9.

Flemming, W. 1880. Beiträge zur Kenntniss der Zelle und Ihrer Lebenserscheinungen. *Archiv für mikroskopische Anatomie*. 18:151-259.

Fukuda, Y., U. Laugks, V. Lucic, W. Baumeister, and R. Danev. 2015. Electron cryotomography of vitrified cells with a Volta phase plate. *J Struct Biol*. 190:143-154.

Gan, L., M.S. Ladinsky, and G.J. Jensen. 2013. Chromatin in a marine picoeukaryote is a disordered assemblage of nucleosomes. *Chromosoma*. 122:377-386.

Garcia-Saez, I., H. Menoni, R. Boopathi, M.S. Shukla, L. Soueidan, M. Noirclerc-Savoye, A. Le Roy, D.A. Skoufias, J. Bednar, A. Hamiche, D. Angelov, C. Petosa, and S. Dimitrov. 2018. Structure of an H1-Bound 6-Nucleosome Array Reveals an Untwisted Two-Start Chromatin Fiber Conformation. *Mol Cell*. 72:902-915 e907.

Geiss, C.P., D. Keramisanou, N. Sekulic, M.P. Scheffer, B.E. Black, and A.S. Frangakis. 2014. CENP-A arrays are more condensed than canonical arrays at low ionic strength. *Biophys J*. 106:875-882.

Gibson, B.A., C. Blaukopf, T. Lou, L. Chen, L.K. Doolittle, I. Finkelstein, G.J. Narlikar, D.W. Gerlich, and M.K. Rosen. 2023. In diverse conditions, intrinsic chromatin condensates have liquid-like material properties. *Proc Natl Acad Sci U S A*. 120:e2218085120.

Gibson, B.A., L.K. Doolittle, M.W.G. Schneider, L.E. Jensen, N. Gamarra, L. Henry, D.W. Gerlich, S. Redding, and M.K. Rosen. 2019. Organization of Chromatin by Intrinsic and Regulated Phase Separation. *Cell*. 179:470-484 e421.

Grau, D., Y. Zhang, C.H. Lee, M. Valencia-Sanchez, J. Zhang, M. Wang, M. Holder, V. Svetlov, D. Tan, E. Nudler, D. Reinberg, T. Walz, and K.J. Armache. 2021. Structures of monomeric and dimeric PRC2:EZH1 reveal flexible modules involved in chromatin compaction. *Nat Commun*. 12:714.

Han, H.M., J. Huebinger, and M. Grabenbauer. 2012. Self-pressurized rapid freezing (SPRF) as a simple fixation method for cryo-electron microscopy of vitreous sections. *J Struct Biol*. 178:84-87.

Han, Y., A.A. Reyes, S. Malik, and Y. He. 2020. Cryo-EM structure of SWI/SNF complex bound to a nucleosome. *Nature*. 579:452-455.

Harapin, J., M. Bormel, K.T. Sapra, D. Brunner, A. Kaech, and O. Medalia. 2015. Structural analysis of multicellular organisms with cryo-electron tomography. *Nature methods*. 12:634-636.

Harlen, K.M., and L.S. Churchman. 2017. The code and beyond: transcription regulation by the RNA polymerase II carboxy-terminal domain. *Nat Rev Mol Cell Biol*. 18:263-273.

Hayashida, M., R. Phengchat, M. Malac, K. Harada, T. Akashi, N. Ohmido, and K. Fukui. 2021. Higher-Order Structure of Human Chromosomes Observed by Electron Diffraction and Electron Tomography. *Microsc Microanal*. 27:149-155.

Hayles, M.F., D.J. Stokes, D. Phifer, and K.C. Findlay. 2007. A technique for improved focused ion beam milling of cryo-prepared life science specimens. *J Microsc*. 226:263-269.

He, S., Z. Wu, Y. Tian, Z. Yu, J. Yu, X. Wang, J. Li, B. Liu, and Y. Xu. 2020. Structure of nucleosome-bound human BAF complex. *Science*. 367:875-881.

Henneman, B., C. van Emmerik, H. van Ingen, and R.T. Dame. 2018. Structure and function of archaeal histones. *PLoS Genet*. 14:e1007582.

Heumann, J.M. 2023. PEET. University of Colorado Boulder.

Heumann, J.M., A. Hoenger, and D.N. Mastronarde. 2011. Clustering and variance maps for cryo-electron tomography using wedge-masked differences. *J Struct Biol*. 175:288-299.

Hewish, D.R., and L.A. Burgoyne. 1973. Chromatin sub-structure. The digestion of chromatin DNA at regularly spaced sites by a nuclear deoxyribonuclease. *Biochem Biophys Res Commun*. 52:504-510.

Heymann, B.J. 2022. Bsoft: Image Processing for Structural Biology. *Bio Protoc*. 12:e4393.

Hilbert, L., Y. Sato, K. Kuznetsova, T. Bianucci, H. Kimura, F. Julicher, A. Honigmann, V. Zaburdaev, and N.L. Vastenhouw. 2021. Transcription organizes euchromatin via microphase separation. *Nat Commun*. 12:1360.

Huxley, H.E., and G. Zubay. 1961. Preferential staining of nucleic acid-containing structures for electron microscopy. *J Biophys Biochem Cytol*. 11:273-296.

Itoh, Y., E.J. Woods, K. Minami, K. Maeshima, and R. Collepardo-Guevara. 2021. Liquid-like chromatin in the cell: What can we learn from imaging and computational modeling? *Current opinion in structural biology*. 71:123-135.

Iudin, A., P.K. Korir, J. Salavert-Torres, G.J. Kleywegt, and A. Patwardhan. 2016. EMPIAR: a public archive for raw electron microscopy image data. *Nature methods*. 13:387-388.

Jentink, N., C. Purnell, B. Kable, M. Swulius, and S.A. Grigoryev. 2022. Cryo-electron tomography reveals the multiplex anatomy of condensed native chromatin and its unfolding by histone citrullination. *bioRxiv*.

Kamasaki, T., E. O'Toole, S. Kita, M. Osumi, J. Usukura, J.R. McIntosh, and G. Goshima. 2013. Augmin-dependent microtubule nucleation at microtubule walls in the spindle. *J Cell Biol*. 202:25-33.

Kasinath, V., C. Beck, P. Sauer, S. Poepsel, J. Kosmatka, M. Faini, D. Toso, R. Aebersold, and E. Nogales. 2021. JARID2 and AEBP2 regulate PRC2 in the presence of H2AK119ub1 and other histone modifications. *Science*. 371.

Khatter, H., A.G. Myasnikov, S.K. Natchiar, and B.P. Klaholz. 2015. Structure of the human 80S ribosome. *Nature*. 520:640-645.

Kimanius, D., B.O. Forsberg, S.H. Scheres, and E. Lindahl. 2016. Accelerated cryo-EM structure determination with parallelisation using GPUs in RELION-2. *Elife*. 5.

Komarnitsky, P., E.J. Cho, and S. Buratowski. 2000. Different phosphorylated forms of RNA polymerase II and associated mRNA processing factors during transcription. *Genes Dev*. 14:2452-2460.

Kornberg, R.D. 1974. Chromatin structure: a repeating unit of histones and DNA. *Science*. 184:868-871.

Kremer, J.R., D.N. Mastronarde, and J.R. McIntosh. 1996. Computer visualization of three-dimensional image data using IMOD. *Journal of Structural Biology*. 116:71-76.

Kujirai, T., H. Ehara, Y. Fujino, M. Shirouzu, S.I. Sekine, and H. Kurumizaka. 2018. Structural basis of the nucleosome transition during RNA polymerase II passage. *Science*. 362:595-598.

Ladinsky, M.S., J.M. Pierson, and J.R. McIntosh. 2006. Vitreous cryo-sectioning of cells facilitated by a micromanipulator. *J Microsc*. 224:129-134.

Langmore, J.P., and J.R. Paulson. 1983. Low angle x-ray diffraction studies of chromatin structure in vivo and in isolated nuclei and metaphase chromosomes. *J Cell Biol*. 96:1120-1131.

Lau, B., J. Cheng, D. Flemming, G. La Venuta, O. Berninghausen, R. Beckmann, and E. Hurt. 2021. Structure of the Maturing 90S Pre-ribosome in Association with the RNA Exosome. *Mol Cell*. 81:293-303 e294.

Lewis, T.S., V. Sokolova, H. Jung, H. Ng, and D. Tan. 2021. Structural basis of chromatin regulation by histone variant H2A.Z. *Nucleic Acids Res*. 49:11379-11391.

Li, Y., A. Eshein, R.K.A. Virk, A. Eid, W. Wu, J. Frederick, D. VanDerway, S. Gladstein, K. Huang, A.R. Shim, N.M. Anthony, G.M. Bauer, X. Zhou, V. Agrawal, E.M. Pujadas, S. Jain, G. Esteve, J.E. Chandler, T.Q. Nguyen, R. Bleher, J.J. de Pablo, I. Szleifer, V.P. Dravid, L.M. Almassalha, and V. Backman. 2021. Nanoscale chromatin imaging and analysis platform bridges 4D chromatin organization with molecular function. *Sci Adv*. 7.

Liu, X., M. Li, X. Xia, X. Li, and Z. Chen. 2017. Mechanism of chromatin remodelling revealed by the Snf2-nucleosome structure. *Nature*. 544:440-445.

Liu, Y., Y. Zhang, H. Xue, M. Cao, G. Bai, Z. Mu, Y. Yao, S. Sun, D. Fang, and J. Huang. 2021. Cryo-EM structure of SETD2/Set2 methyltransferase bound to a nucleosome containing oncohistone mutations. *Cell Discov*. 7:32.

Liu, Y., K. Zhou, N. Zhang, H. Wei, Y.Z. Tan, Z. Zhang, B. Carragher, C.S. Potter, S. D'Arcy, and K. Luger. 2020. FACT caught in the act of manipulating the nucleosome. *Nature*. 577:426-431.

Luger, K., A.W. Mader, R.K. Richmond, D.F. Sargent, and T.J. Richmond. 1997. Crystal structure of the nucleosome core particle at 2.8 A resolution. *Nature*. 389:251-260.

Ma, O.X., W.G. Chong, J.K.E. Lee, S. Cai, C.A. Siebert, A. Howe, P. Zhang, J. Shi, U. Surana, and L. Gan. 2022. Cryo-ET detects bundled triple helices but not ladders in meiotic budding yeast. *PLoS One*. 17:e0266035.

Maeshima, K., R. Rogge, S. Tamura, Y. Joti, T. Hikima, H. Szerlong, C. Krause, J. Herman, E. Seidel, J. DeLuca, T. Ishikawa, and J.C. Hansen. 2016. Nucleosomal arrays self-assemble into supramolecular globular structures lacking 30-nm fibers. *EMBO J*. 35:1115-1132.

Mahamid, J., S. Pfeffer, M. Schaffer, E. Villa, R. Danev, L.K. Cuellar, F. Forster, A.A. Hyman, J.M. Plitzko, and W. Baumeister. 2016. Visualizing the molecular sociology at the HeLa cell nuclear periphery. *Science*. 351:969-972.

Marko, M., C. Hsieh, W. Moberlychan, C.A. Mannella, and J. Frank. 2006. Focused ion beam milling of vitreous water: prospects for an alternative to cryo-ultramicrotomy of frozen-hydrated biological samples. *J Microsc*. 222:42-47.

Mashtalir, N., H. Suzuki, D.P. Farrell, A. Sankar, J. Luo, M. Filipovski, A.R. D'Avino, R. St Pierre, A.M. Valencia, T. Onikubo, R.G. Roeder, Y. Han, Y. He, J.A. Ranish, F. DiMaio, T. Walz, and C. Kadoch. 2020. A Structural Model of the Endogenous Human BAF Complex Informs Disease Mechanisms. *Cell*. 183:802-817 e824.

Mastronarde, D.N. 1997. Dual-axis tomography: an approach with alignment methods that preserve resolution. *J Struct Biol*. 120:343-352.

Mastronarde, D.N. 2005. Automated electron microscope tomography using robust prediction of specimen movements. *J Struct Biol*. 152:36-51.

Mastronarde, D.N., and S.R. Held. 2017. Automated tilt series alignment and tomographic reconstruction in IMOD. *J Struct Biol*. 197:102-113.

McDowall, A.W., J.M. Smith, and J. Dubochet. 1986. Cryo-electron microscopy of vitrified chromosomes in situ. *EMBO J*. 5:1395-1402.

Medeiros, J.M., D. Bock, G.L. Weiss, R. Kooger, R.A. Wepf, and M. Pilhofer. 2018. Robust workflow and instrumentation for cryo-focused ion beam milling of samples for electron cryotomography. *Ultramicroscopy*. 190:1-11.

Michael, A.K., R.S. Grand, L. Isbel, S. Cavadini, Z. Kozicka, G. Kempf, R.D. Bunker, A.D. Schenk, A. Graff-Meyer, G.R. Pathare, J. Weiss, S. Matsumoto, L. Burger, D. Schubeler, and N.H. Thoma. 2020. Mechanisms of OCT4-SOX2 motif readout on nucleosomes. *Science*. 368:1460-1465.

Miron, E., R. Oldenkamp, J.M. Brown, D.M.S. Pinto, C.S. Xu, A.R. Faria, H.A. Shaban, J.D.P. Rhodes, C. Innocent, S. de Ornellas, H.F. Hess, V. Buckle, and L. Schermelleh. 2020. Chromatin arranges in chains of mesoscale domains with nanoscale functional topography independent of cohesin. *Sci Adv*. 6.

Nagashima, R., K. Hibino, S.S. Ashwin, M. Babokhov, S. Fujishiro, R. Imai, T. Nozaki, S. Tamura, T. Tani, H. Kimura, M. Shribak, M.T. Kanemaki, M. Sasai, and K. Maeshima. 2019. Single nucleosome imaging reveals loose genome chromatin networks via active RNA polymerase II. *J Cell Biol*. 218:1511-1530.

Ng, C.T., L. Deng, C. Chen, H.H. Lim, J. Shi, U. Surana, and L. Gan. 2019. Electron cryotomography analysis of Dam1C/DASH at the kinetochore-spindle interface in situ. *J Cell Biol*. 218:455–473.

Ng, C.T., and L. Gan. 2020. Investigating eukaryotic cells with cryo-ET. *Mol Biol Cell*. 31:87-100.

Ng, C.T., M.S. Ladinsky, and L. Gan. 2020. Serial Cryomicrotomy of Saccharomyces cerevisiae for Serial Electron Cryotomography. *Bio Protoc*. 10:e3831.

Nicastro, D., C. Schwartz, J. Pierson, R. Gaudette, M.E. Porter, and J.R. McIntosh. 2006. The molecular architecture of axonemes revealed by cryoelectron tomography. *Science*. 313:944-948.

Nishimura, M., Y. Takizawa, K. Nozawa, and H. Kurumizaka. 2022. Structural basis for p53 binding to its nucleosomal target DNA sequence. *PNAS Nexus*. 1:pgac177.

Nishino, Y., M. Eltsov, Y. Joti, K. Ito, H. Takata, Y. Takahashi, S. Hihara, A.S. Frangakis, N. Imamoto, T. Ishikawa, and K. Maeshima. 2012. Human mitotic chromosomes consist predominantly of irregularly folded nucleosome fibres without a 30-nm chromatin structure. *The EMBO journal*. 31:1644-1653.

Nodelman, I.M., S. Das, A.M. Faustino, S.D. Fried, G.D. Bowman, and J.P. Armache. 2022. Nucleosome recognition and DNA distortion by the Chd1 remodeler in a nucleotide-free state. *Nat Struct Mol Biol*. 29:121-129.

Nozaki, T., R. Imai, M. Tanbo, R. Nagashima, S. Tamura, T. Tani, Y. Joti, M. Tomita, K. Hibino, M.T. Kanemaki, K.S. Wendt, Y. Okada, T. Nagai, and K. Maeshima. 2017. Dynamic Organization of Chromatin Domains Revealed by Super-Resolution Live-Cell Imaging. *Mol Cell*. 67:282-293 e287.

Ohta, S., J.C. Bukowski-Wills, L. Sanchez-Pulido, L. Alves Fde, L. Wood, Z.A. Chen, M. Platani, L. Fischer, D.F. Hudson, C.P. Ponting, T. Fukagawa, W.C. Earnshaw, and J. Rappsilber. 2010. The protein composition of mitotic chromosomes determined using multiclassifier combinatorial proteomics. *Cell*. 142:810-821.

Olins, A.L., and D.E. Olins. 1974. Spheroid chromatin units (v bodies). *Science*. 183:330-332.

Oliva, A., A. Rosebrock, F. Ferrezuelo, S. Pyne, H. Chen, S. Skiena, B. Futcher, and J. Leatherwood. 2005. The cell cycle-regulated genes of Schizosaccharomyces pombe. *PLoS Biol*. 3:e225.

Otterstrom, J., A. Castells-Garcia, C. Vicario, P.A. Gomez-Garcia, M.P. Cosma, and M. Lakadamyali. 2019. Super-resolution microscopy reveals how histone tail acetylation affects DNA compaction within nucleosomes in vivo. *Nucleic Acids Res*. 47:8470-8484.

Ou, H.D., S. Phan, T.J. Deerinck, A. Thor, M.H. Ellisman, and C.C. O'Shea. 2017. ChromEMT: Visualizing 3D chromatin structure and compaction in interphase and mitotic cells. *Science*. 357.

Pacheco-Fiallos, B., M.K. Vorlander, D. Riabov-Bassat, L. Fin, F.J. O'Reilly, F.I. Ayala, U. Schellhaas, J. Rappsilber, and C. Plaschka. 2023. mRNA recognition and packaging by the human transcription-export complex. *Nature*. 616:828-835.

Palozola, K.C., G. Donahue, H. Liu, G.R. Grant, J.S. Becker, A. Cote, H. Yu, A. Raj, and K.S. Zaret. 2017. Mitotic transcription and waves of gene reactivation during mitotic exit. *Science*. 358:119-122.

Patel, A.B., C.M. Moore, B.J. Greber, J. Luo, S.A. Zukin, J. Ranish, and E. Nogales. 2019. Architecture of the chromatin remodeler RSC and insights into its nucleosome engagement. *Elife*. 8.

Peng, X., R.K. Karuturi, L.D. Miller, K. Lin, Y. Jia, P. Kondu, L. Wang, L.S. Wong, E.T. Liu, M.K. Balasubramanian, and J. Liu. 2005. Identification of cell cycle-regulated genes in fission yeast. *Mol Biol Cell*. 16:1026-1042.

Pettersen, E.F., T.D. Goddard, C.C. Huang, G.S. Couch, D.M. Greenblatt, E.C. Meng, and T.E. Ferrin. 2004. UCSF Chimera--a visualization system for exploratory research and analysis. *J Comput Chem*. 25:1605-1612.

Poepsel, S., V. Kasinath, and E. Nogales. 2018. Cryo-EM structures of PRC2 simultaneously engaged with two functionally distinct nucleosomes. *Nat Struct Mol Biol*. 25:154-162.

Prescott, D.M., and M.A. Bender. 1962. Synthesis of RNA and protein during mitosis in mammalian tissue culture cells. *Exp Cell Res*. 26:260-268.

Remnant, L., N.Y. Kochanova, C. Reid, F. Cisneros-Soberanis, and W.C. Earnshaw. 2021. The intrinsically disorderly story of Ki-67. *Open Biol*. 11:210120.

Ricci, M.A., C. Manzo, M.F. Garcia-Parajo, M. Lakadamyali, and M.P. Cosma. 2015. Chromatin fibers are formed by heterogeneous groups of nucleosomes in vivo. *Cell*. 160:1145-1158.

Rigort, A., F.J. Bauerlein, A. Leis, M. Gruska, C. Hoffmann, T. Laugks, U. Bohm, M. Eibauer, H. Gnaegi, W. Baumeister, and J.M. Plitzko. 2010. Micromachining tools and correlative approaches for cellular cryo-electron tomography. *J Struct Biol*. 172:169-179.

Ruan, W., G. Venkatachalam, R.M. Sobota, L. Chen, L.C. Wang, A. Jacobson, K. Paramasivam, and U. Surana. 2019. Resistance to anti-microtubule drug-induced cell death is determined by regulation of BimEL expression. *Oncogene*. 38:4352-4365.

Rustici, G., J. Mata, K. Kivinen, P. Lio, C.J. Penkett, G. Burns, J. Hayles, A. Brazma, P. Nurse, and J. Bahler. 2004. Periodic gene expression program of the fission yeast cell cycle. *Nat Genet*. 36:809-817.

Sanulli, S., M.J. Trnka, V. Dharmarajan, R.W. Tibble, B.D. Pascal, A.L. Burlingame, P.R. Griffin, J.D. Gross, and G.J. Narlikar. 2019. HP1 reshapes nucleosome core to promote phase separation of heterochromatin. *Nature*. 575:390-394.

Schaffer, M., B.D. Engel, T. Laugks, J. Mahamid, J.M. Plitzko, and W. Baumeister. 2015. Cryo-focused Ion Beam Sample Preparation for Imaging Vitreous Cells by Cryo-electron Tomography. *Bio Protoc*. 5.

Schalch, T., S. Duda, D.F. Sargent, and T.J. Richmond. 2005. X-ray structure of a tetranucleosome and its implications for the chromatin fibre. *Nature*. 436:138-141.

Scheffer, M.P., M. Eltsov, J. Bednar, and A.S. Frangakis. 2012. Nucleosomes stacked with aligned dyad axes are found in native compact chromatin in vitro. *J Struct Biol*. 178:207-214.

Scheffer, M.P., M. Eltsov, and A.S. Frangakis. 2011. Evidence for short-range helical order in the 30-nm chromatin fibers of erythrocyte nuclei. *Proc Natl Acad Sci U S A*. 108:16992-16997.

Schindelin, J., I. Arganda-Carreras, E. Frise, V. Kaynig, M. Longair, T. Pietzsch, S. Preibisch, C. Rueden, S. Saalfeld, B. Schmid, J.Y. Tinevez, D.J. White, V. Hartenstein, K. Eliceiri, P. Tomancak, and A. Cardona. 2012. Fiji: an open-source platform for biological-image analysis. *Nature methods*. 9:676-682.

Scott, S.J., K.S. Suvarna, and P.P. D'Avino. 2020. Synchronization of human retinal pigment epithelial-1 cells in mitosis. *J Cell Sci*. 133.

Sedat, J., A. McDonald, H. Cang, J. Lucas, M. Arigovindan, Z. Kam, C. Murre, and M. Elbaum. 2022a. A proposed unified interphase nucleus chromosome structure: Preliminary preponderance of evidence. *Proc Natl Acad Sci U S A*. 119:e2119101119.

Sedat, J., A. McDonald, H. Kasler, E. Verdin, H. Cang, M. Arigovindan, C. Murre, and M. Elbaum. 2022b. A proposed unified mitotic chromosome architecture. *Proc Natl Acad Sci U S A*. 119:e2119107119.

Simpson, R.T. 1978. Structure of the chromatosome, a chromatin particle containing 160 base pairs of DNA and all the histones. *Biochemistry*. 17:5524-5531.

Soman, A., S.Y. Wong, N. Korolev, W. Surya, S. Lattmann, V.K. Vogirala, Q. Chen, N.V. Berezhnoy, J. van Noort, D. Rhodes, and L. Nordenskiold. 2022. Columnar structure of human telomeric chromatin. *Nature*. 609:1048-1055.

Song, F., P. Chen, D. Sun, M. Wang, L. Dong, D. Liang, R.M. Xu, P. Zhu, and G. Li. 2014. Cryo-EM study of the chromatin fiber reveals a double helix twisted by tetranucleosomal units. *Science*. 344:376-380.

Spellman, P.T., G. Sherlock, M.Q. Zhang, V.R. Iyer, K. Anders, M.B. Eisen, P.O. Brown, D. Botstein, and B. Futcher. 1998. Comprehensive identification of cell cycle-regulated genes of the yeast Saccharomyces cerevisiae by microarray hybridization. *Mol Biol Cell*. 9:3273-3297.

Stanek, D., and A.H. Fox. 2017. Nuclear bodies: news insights into structure and function. *Current opinion in cell biology*. 46:94-101.

Stenstrom, L., D. Mahdessian, C. Gnann, A.J. Cesnik, W. Ouyang, M.D. Leonetti, M. Uhlen, S. Cuylen-Haering, P.J. Thul, and E. Lundberg. 2020. Mapping the nucleolar proteome reveals a spatiotemporal organization related to intrinsic protein disorder. *Mol Syst Biol*. 16:e9469.

Strickfaden, H., T.O. Tolsma, A. Sharma, D.A. Underhill, J.C. Hansen, and M.J. Hendzel. 2020. Condensed Chromatin Behaves like a Solid on the Mesoscale In Vitro and in Living Cells. *Cell*. 183:1772-1784 e1713.

Studer, D., A. Klein, I. Iacovache, H. Gnaegi, and B. Zuber. 2014. A new tool based on two micromanipulators facilitates the handling of ultrathin cryosection ribbons. *J Struct Biol*. 185:125-128.

Takizawa, Y., C.H. Ho, H. Tachiwana, H. Matsunami, W. Kobayashi, M. Suzuki, Y. Arimura, T. Hori, T. Fukagawa, M.D. Ohi, M. Wolf, and H. Kurumizaka. 2020. Cryo-EM Structures of Centromeric Tri-nucleosomes Containing a Central CENP-A Nucleosome. *Structure*. 28:44-53 e44.

Tan, Z.Y., S. Cai, A.J. Noble, J.K. Chen, J. Shi, and L. Gan. 2023. Heterogeneous non-canonical nucleosomes predominate in yeast cells in situ. *Elife*. 12.

Tanaka, H., Y. Takizawa, M. Takaku, D. Kato, Y. Kumagawa, S.A. Grimm, P.A. Wade, and H. Kurumizaka. 2020. Interaction of the pioneer transcription factor GATA3 with nucleosomes. *Nat Commun*. 11:4136.

Tang, G., L. Peng, P.R. Baldwin, D.S. Mann, W. Jiang, I. Rees, and S.J. Ludtke. 2007. EMAN2: an extensible image processing suite for electron microscopy. *J Struct Biol*. 157:38-46.

Taylor, J.H. 1960. Nucleic acid synthesis in relation to the cell division cycle. *Ann N Y Acad Sci*. 90:409-421.

Teves, S.S., L. An, A.S. Hansen, L. Xie, X. Darzacq, and R. Tjian. 2016. A dynamic mode of mitotic bookmarking by transcription factors. *Elife*. 5.

Tivol, W.F., A. Briegel, and G.J. Jensen. 2008. An improved cryogen for plunge freezing. *Microsc Microanal*. 14:375-379.

Villa, E., M. Schaffer, J.M. Plitzko, and W. Baumeister. 2013. Opening windows into the cell: focused-ion-beam milling for cryo-electron tomography. *Current opinion in structural biology*. 23:771-777.

Wang, H., S. Schilbach, M. Ninov, H. Urlaub, and P. Cramer. 2023. Structures of transcription preinitiation complex engaged with the +1 nucleosome. *Nat Struct Mol Biol*. 30:226-232.

Wang, H., L. Xiong, and P. Cramer. 2021a. Structures and implications of TBP-nucleosome complexes. *Proc Natl Acad Sci U S A*. 118.

Wang, J., C. Hu, X. Chen, Y. Li, J. Sun, D.M. Czajkowsky, and Z. Shao. 2022a. Single-Molecule Micromanipulation and Super-Resolution Imaging Resolve Nanodomains Underlying Chromatin Folding in Mitotic Chromosomes. *ACS Nano*. 16:8030-8039.

Wang, L., J. Yu, Z. Yu, Q. Wang, W. Li, Y. Ren, Z. Chen, S. He, and Y. Xu. 2022b. Structure of nucleosome-bound human PBAF complex. *Nat Commun*. 13:7644.

Wang, S., V.K. Vogirala, A. Soman, N.V. Berezhnoy, Z.B. Liu, A.S.W. Wong, N. Korolev, C.J. Su, S. Sandin, and L. Nordenskiold. 2021b. Linker histone defines structure and self-association behaviour of the 177 bp human chromatosome. *Sci Rep*. 11:380.

Weis, F., W.J.H. Hagen, M. Schorb, and S. Mattei. 2021. Strategies for Optimization of Cryogenic Electron Tomography Data Acquisition. *J Vis Exp*.

Willhoft, O., M. Ghoneim, C.L. Lin, E.Y.D. Chua, M. Wilkinson, Y. Chaban, R. Ayala, E.A. McCormack, L. Ocloo, D.S. Rueda, and D.B. Wigley. 2018. Structure and dynamics of the yeast SWR1-nucleosome complex. *Science*. 362.

Xiang, W., M.J. Roberti, J.K. Heriche, S. Huet, S. Alexander, and J. Ellenberg. 2018. Correlative live and super-resolution imaging reveals the dynamic structure of replication domains. *J Cell Biol*. 217:1973-1984.

Xu, J., H. Ma, J. Jin, S. Uttam, R. Fu, Y. Huang, and Y. Liu. 2018. Super-Resolution Imaging of Higher-Order Chromatin Structures at Different Epigenomic States in Single Mammalian Cells. *Cell Rep*. 24:873-882.

Yakovlev, S., and K.H. Downing. 2011. Freezing in sealed capillaries for preparation of frozen hydratedsections. *J Microsc*. 244:235-247.

Yan, L., H. Wu, X. Li, N. Gao, and Z. Chen. 2019. Structures of the ISWI-nucleosome complex reveal a conserved mechanism of chromatin remodeling. *Nat Struct Mol Biol*. 26:258-266.

Zhang, M., C. Diaz-Celis, B. Onoa, C. Canari-Chumpitaz, K.I. Requejo, J. Liu, M. Vien, E. Nogales, G. Ren, and C. Bustamante. 2022. Molecular organization of the early stages of nucleosome phase separation visualized by cryo-electron tomography. *Mol Cell*.

Zhao, W., and G.J. Jensen. 2022. In situ architecture of human kinetochore-microtubule interface visualized by cryo-electron tomography. *bioRxiv*.

Zheng, S.Q., E. Palovcak, J.P. Armache, K.A. Verba, Y. Cheng, and D.A. Agard. 2017. MotionCor2: anisotropic correction of beam-induced motion for improved cryo-electron microscopy. *Nature methods*. 14:331-332.

Zhou, B.R., H. Feng, S. Kale, T. Fox, H. Khant, N. de Val, R. Ghirlando, A.R. Panchenko, and Y. Bai. 2021. Distinct Structures and Dynamics of Chromatosomes with Different Human Linker Histone Isoforms. *Mol Cell*. 81:166-182 e166.

Zhou, B.R., J. Jiang, H. Feng, R. Ghirlando, T.S. Xiao, and Y. Bai. 2015. Structural Mechanisms of Nucleosome Recognition by Linker Histones. *Mol Cell*. 59:628-638.

Zhou, B.R., J. Jiang, R. Ghirlando, D. Norouzi, K.N. Sathish Yadav, H. Feng, R. Wang, P. Zhang, V. Zhurkin, and Y. Bai. 2018. Revisit of Reconstituted 30-nm Nucleosome Arrays Reveals an Ensemble of Dynamic Structures. *J Mol Biol*. 430:3093-3110.

Zhou, K., G. Gaullier, and K. Luger. 2019. Nucleosome structure and dynamics are coming of age. *Nat Struct Mol Biol*. 26:3-13.

Zhou, K., M. Gebala, D. Woods, K. Sundararajan, G. Edwards, D. Krzizike, J. Wereszczynski, A.F. Straight, and K. Luger. 2022. CENP-N promotes the compaction of centromeric chromatin. *Nat Struct Mol Biol*. 29:403-413.

Zhu, L., and C.P. Brangwynne. 2015. Nuclear bodies: the emerging biophysics of nucleoplasmic phases. *Current opinion in cell biology*. 34:23-30.

Zivanov, J., T. Nakane, B.O. Forsberg, D. Kimanius, W.J. Hagen, E. Lindahl, and S.H. Scheres. 2018. New tools for automated high-resolution cryo-EM structure determination in RELION-3. *Elife*. 7.

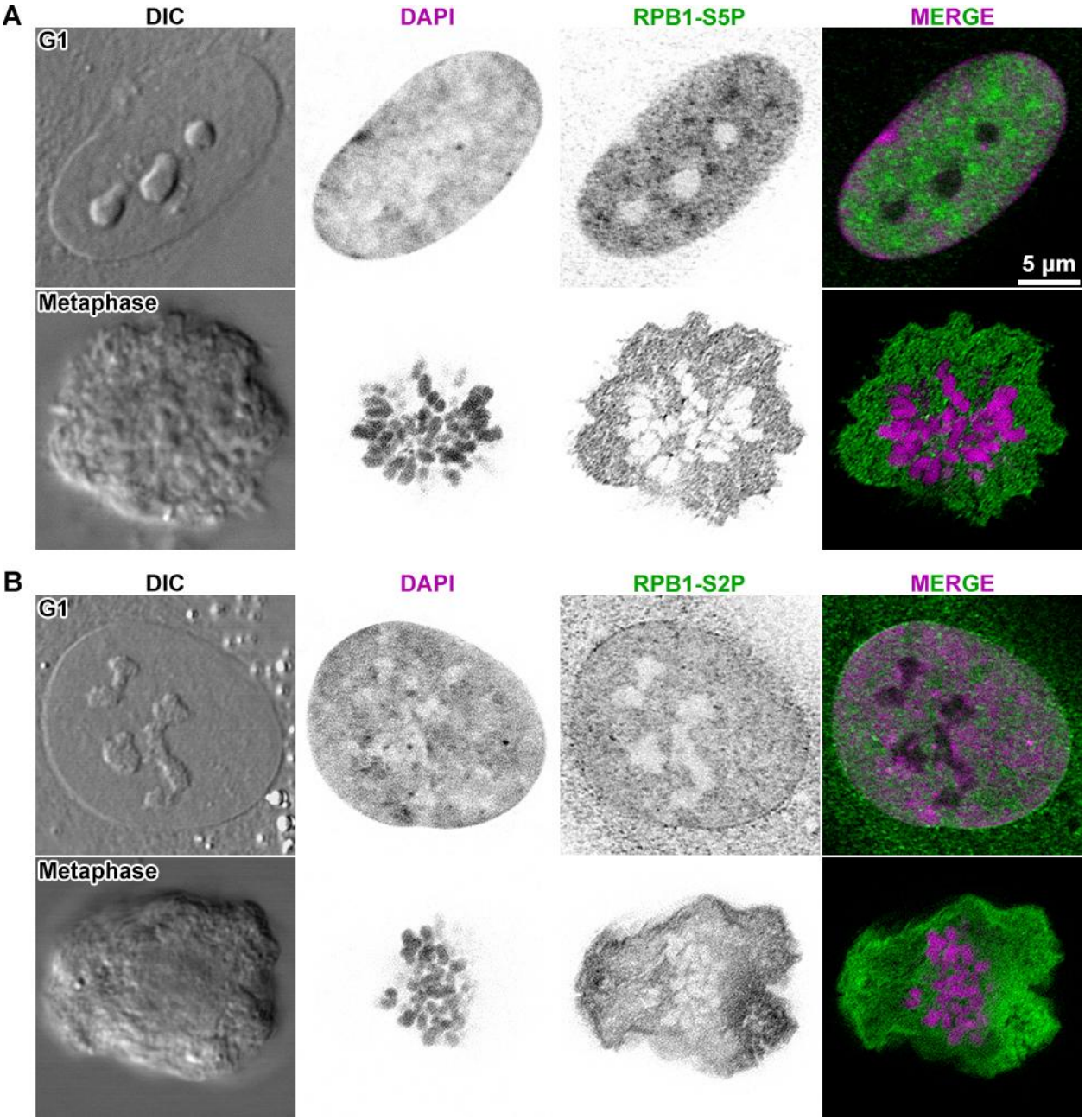

Figure 1. Metaphase chromosomes are depleted of RNA polymerase II
Differential interference contrast (DIC) images of representative G1 and metaphase cells that were stained to detect DNA (stained with DAPI) and immunofluorescent detection of (A) initiating RNA polymerase II (RNAPII) phosphorylated at serine 5 of the RPB1 subunit's C-terminal tail heptad repeats (RPB1-S5P) and (B) elongating RNAPII phosphorylated at serine 2 of the RPB1 subunit's C-terminal tail heptad repeats (RPB1-S2P). In the two middle columns, the DAPI and immunofluorescence signals are shown in inverted contrast for clarity.

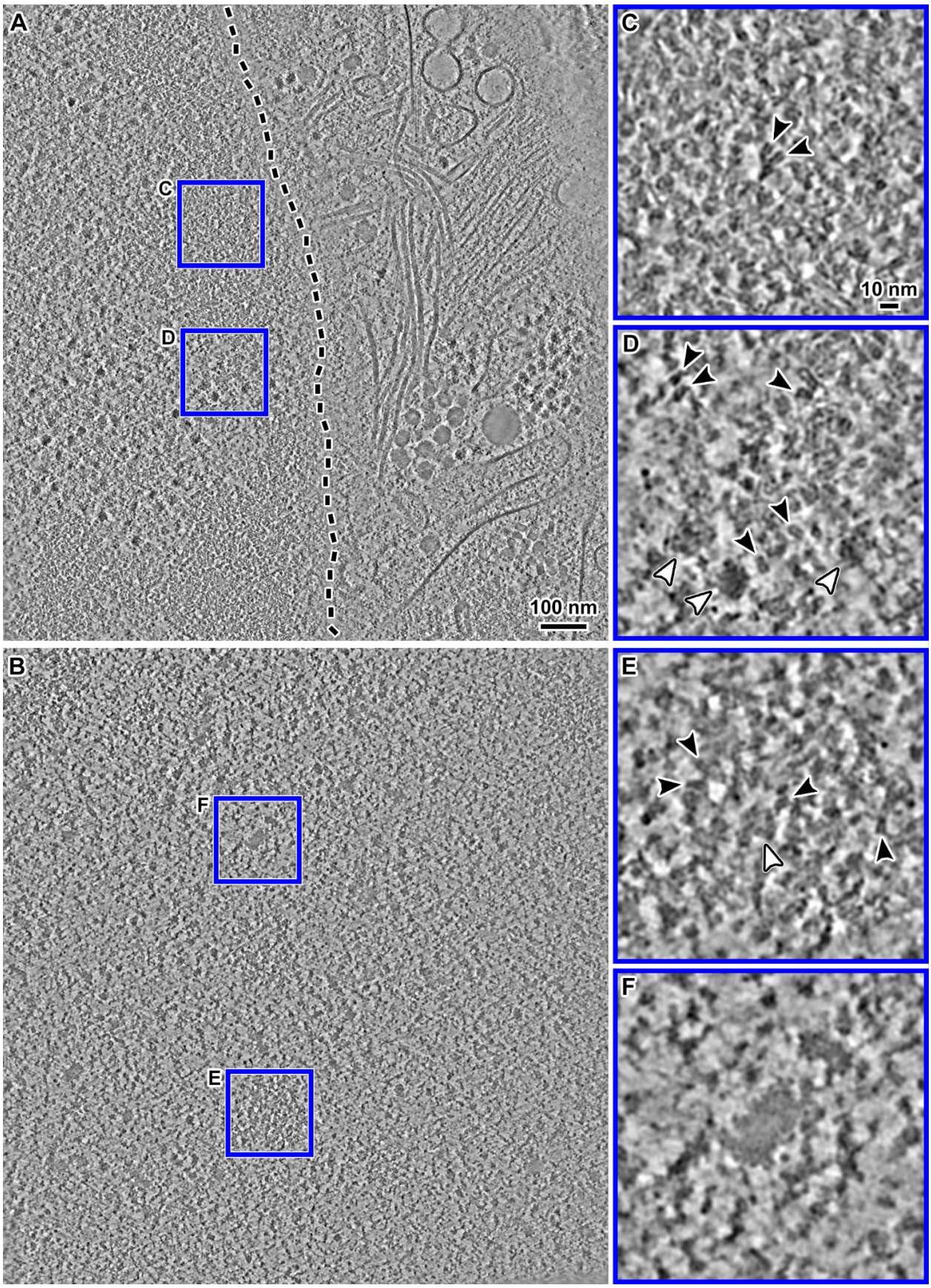
A
C
D
100 nm
B
F
E
C
10 nm
D
E
F

Figure 2. Cryo-ET of G1 chromatin *in situ*
(A) Cryotomographic slice (10 nm) of the perinuclear region. The nuclear envelope is oblique to the milling direction and is therefore not visible. Its approximate center is indicated by the dashed line. **(B)** Cryotomographic slice (10 nm) of a region deeper inside the nucleus. **(C)** Enlargement (4-fold) of one region boxed in panel A, showing a perinuclear chromatin domain. **(D)** Enlargement of a megacomplex-rich nucleoplasm region boxed in panel A. (**E)** Enlargement of the chromatin domain boxed in panel B. **(F)** Enlargement (4-fold) of a “dense irregular body" in panel B. In all insets, nucleosomes are indicated by black arrowheads and megacomplexes are indicated by white arrowheads. These images are from cryotomograms denoised by CryoCARE (Buchholz et al., 2019). Non-denoised versions are shown in Figure S25.

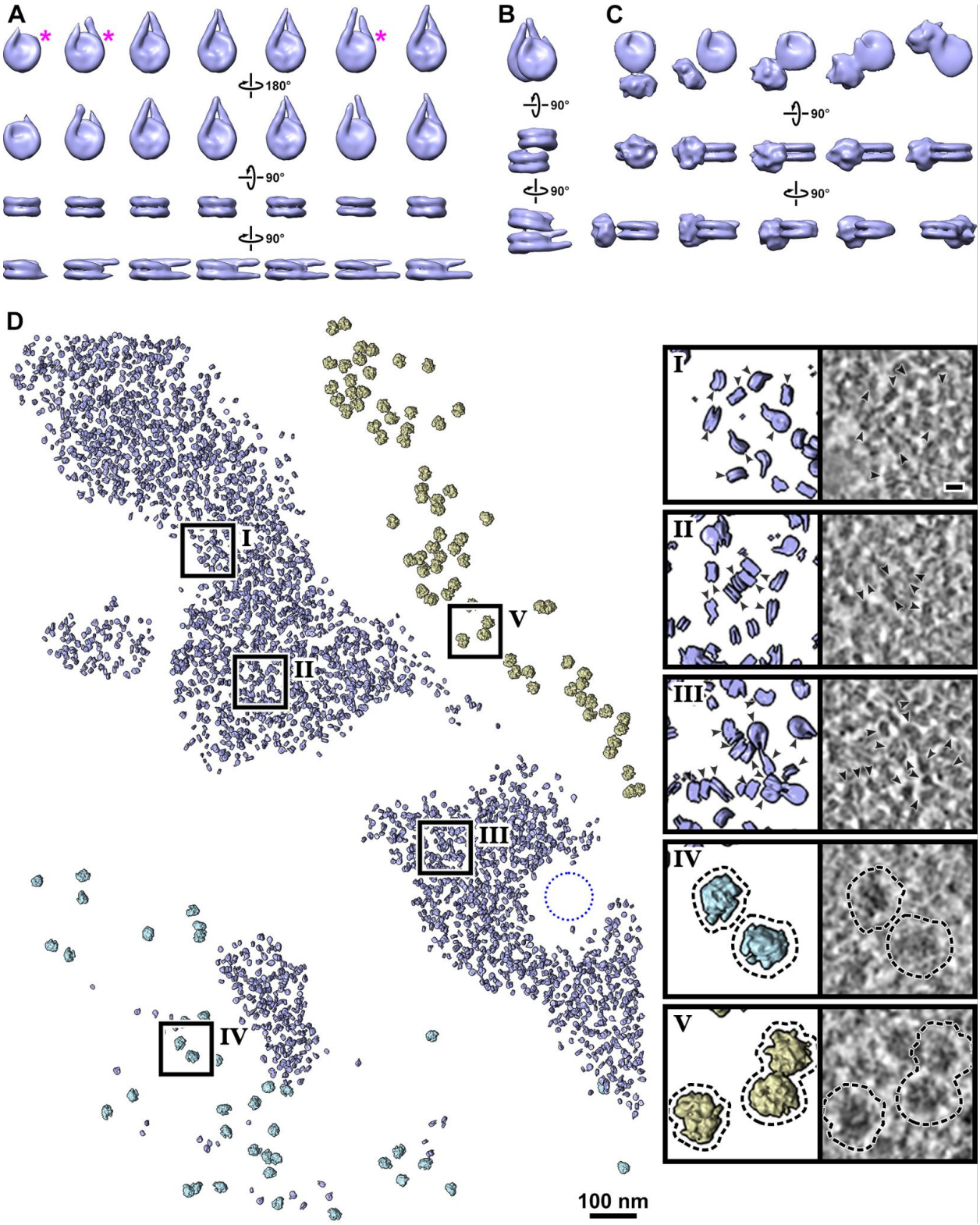

Figure 3. Subtomogram analysis of G1 nucleosomes

(**A**) Subtomogram averages of mononucleosomes in G1 cells, shown in the (top to bottom) disc, disc, gyre, and side views, respectively. They are ordered (left to right) from those having the shortest to the longest ordered linker DNA. Classes marked with a magenta asterisk have noticeably asymmetric linker DNA length. (**B**) Subtomogram average of ordered stacked dinucleosomes. (**C**) Subtomogram averages of nucleosomes with disordered gyre-proximal densities; to show this extra density, these averages are rendered at a lower contour level than those of panels A and B. Some of the images in panels A – C are reproduced from Figure S13; the structures are also shown in Movie S1. (**D**) Remapped model of nucleosomes (blue) in the chromatin domains, preribosomes (light blue), and cytoplasmic ribosomes (yellow). The remapped model includes nucleosome classes shown in panels A – C. To facilitate the visualization of the nucleosomes, the proximal densities are hidden in the remapped model by a combination of higher contour level and the UCSF Chimera “hide dust” tool. The remapped model spans the entire thickness of the lamella (~90 nm). The left insets show 3-fold enlargements of the regions boxed on the left and right inset shows a cryotomographic slice (10 nm) of the same remapped region. The circular gap in the lower-right group of nucleosomes is volume occupied by a nuclear pore complex (approximate position indicated by a 100-nm dotted circle). See also Movie S2. The cryotomographic slices in panel D are from cryotomograms denoised by Cryo-CARE (Buchholz et al., 2019). This figure is reproduced with non-denoised cryotomographic slices in Figure S26.

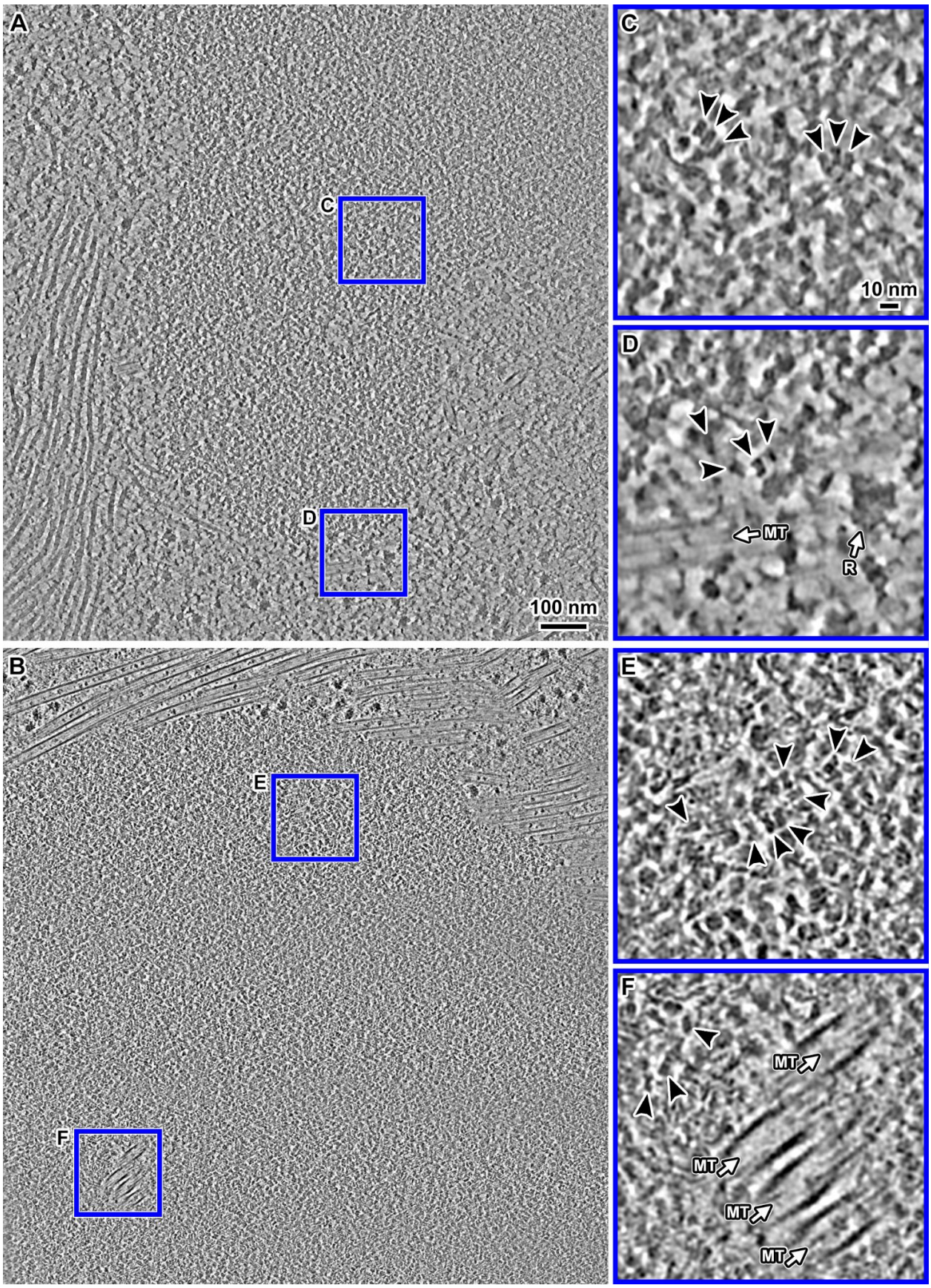
A
C
D
100 nm
B
E
F
C
10 nm
D
MT
R
E
F
MT
MT
MT
MT

Figure 4. Cryo-ET of metaphase chromatin *in situ*
(A and B) Cryotomographic slice (10 nm) overview of portions of two metaphase chromosomes. (**C and D**) Enlargements (4-fold) of two regions boxed in panel A. (**E and F**) Enlargements (4-fold) of two regions boxed in panel B. **Panel E** shows an enlargement of a region of the chromosome boundary. **Panel F** shows an enlargement of microtubules embedded in the chromosome. In all the insets, the nucleosome-like densities (double-gyre motifs and top-views) are indicated by arrowheads. Note that there are stacked nucleosomes in panels C and E. Microtubules (MT) and ribosomes (R) are also indicated in the insets. These images are from cryotomograms denoised by Cryo-CARE (Buchholz et al., 2019). Non-denoised versions are shown in Figure S27.

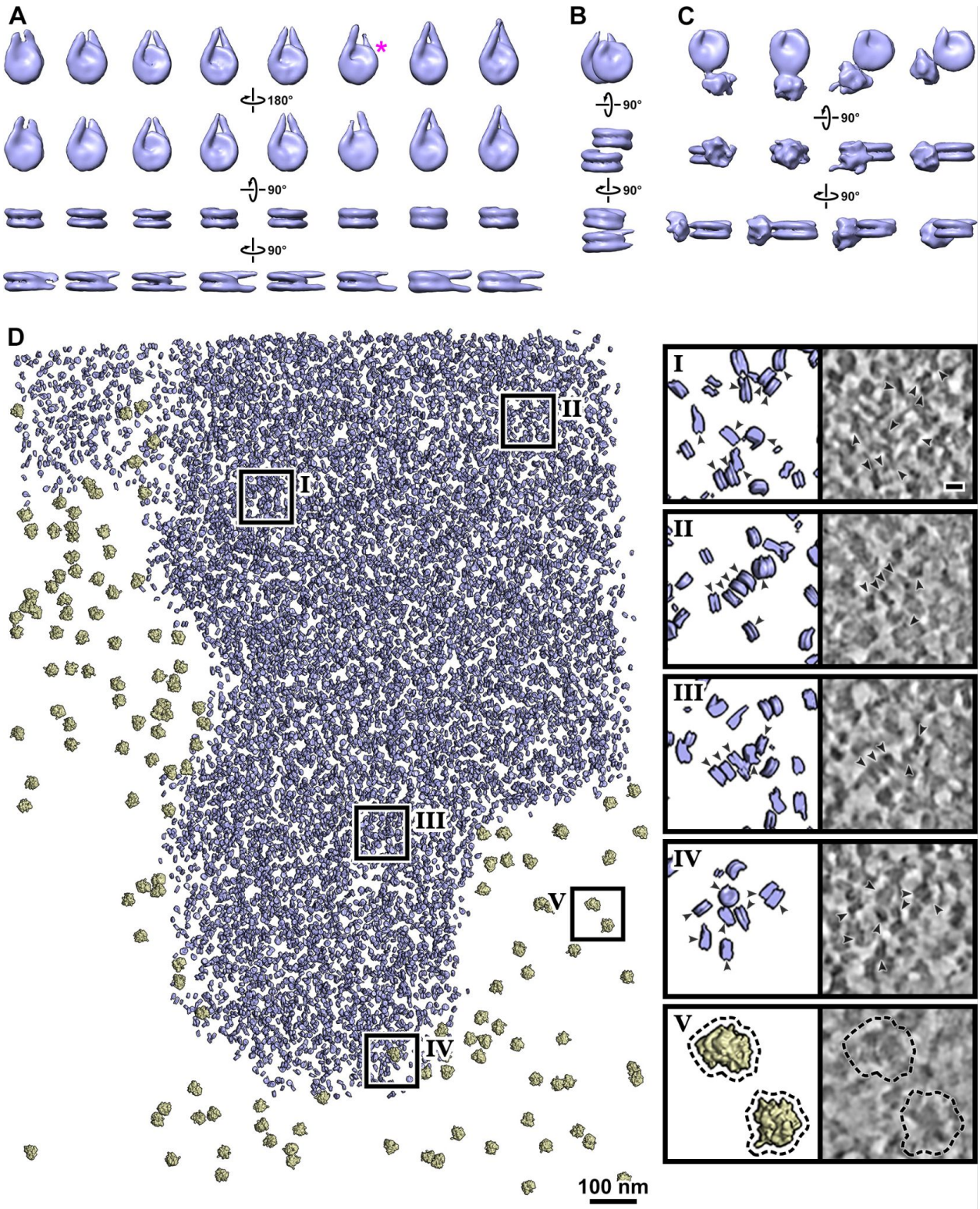

Figure 5. Subtomogram analysis of metaphase nucleosomes
(**A**) Subtomogram averages of mononucleosomes in metaphase cells, shown in the (top to bottom) disc, disc, gyre, and side views, respectively. They are ordered (left to right) from those having the shortest to the longest ordered linker DNA. The class marked with a magenta asterisk has noticeably asymmetric linker DNA length. (**B**)

Subtomogram average of ordered stacked dinucleosomes. (**C**) Subtomogram averages of nucleosomes with disordered gyre-proximal densities; to show this extra density, these averages are rendered at a lower contour level than those of panels A and B. Some of the images in panels A – C are reproduced from Figure S21; the structures are also shown in Movie S3. (**D**) Remapped model of nucleosomes (blue) and ribosomes (yellow). The remapped model includes nucleosome classes shown in panels A – C. Nucleosomes with gyre-proximal densities are not rendered in the remapped model. The remapped volume contains all Z slices of the reconstructed lamella (~140 nm thick). The left insets show 3-fold enlargements of the regions boxed on the left and the right insets show cryotomographic slices (10 nm) of the same remapped region. See also Movie S4. The cryotomographic slices in panel D are from cryotomograms denoised by Cryo-CARE (Buchholz et al., 2019). This figure is reproduced with non-denoised cryotomographic slices in Figure S28.

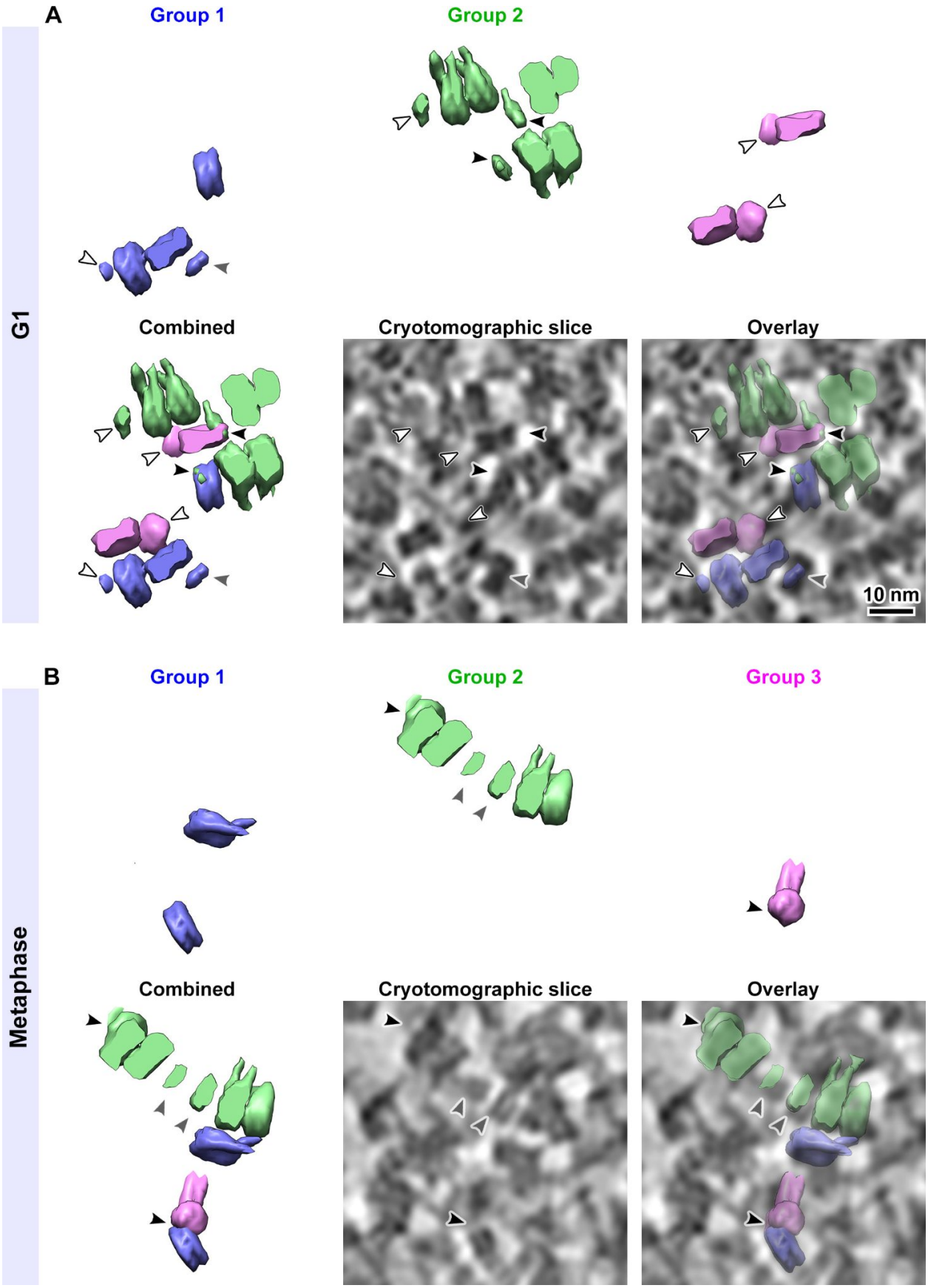
A
Group 1
Group 2
G1
Combined
Cryotomographic slice
Overlay
10 nm
B
Group 1
Group 2
Group 3
Metaphase
Combined
Cryotomographic slice
Overlay

Figure 6. Example of partial overlaps between subtomogram class averages. The panels here show remapped nucleosomes and a 10-nm cryotomographic slice from a region of a (A) G1 and (B) metaphase cell cryotomogram. In the upper panels, the remapped mononucleosomes (Group 1, blue), ordered stacked dinucleosomes (Group 2, green) and nucleosomes with gyre-proximal densities (Group 3, magenta) are rendered separately; and combined in the lower left panel. The remapped models shown here were generated using the nucleosome classes shown in Figures 3 and 5, panels A – C. To facilitate the visualization of the remapped densities, the UCSF Chimera "hide dust" tool was used to hide the small noisy densities. Note that all the nucleosomes in the remapped models here are rendered at a lower contour level to display the extra densities. Comparison of the remapped model with the cryotomographic slice from the same region show that some of the extra densities are indeed located over nucleosomes with side views. Black arrowheads indicate extra densities that partially overlap with a neighboring remapped nucleosome. White arrowheads indicate extra densities that do not appear to overlap any remapped nucleosome. Gray arrowheads indicate an overlap between an extra density with a tomographic slice feature that resembles a nucleosome side view. Possible explanations are that these densities are not nucleosomes or that they are nucleosomes but were misclassified. The cryotomographic slices shown here are from cryotomograms that were denoised using cryo-CARE. This figure is reproduced with non-denoised cryotomographic slices in **Figure S29**.

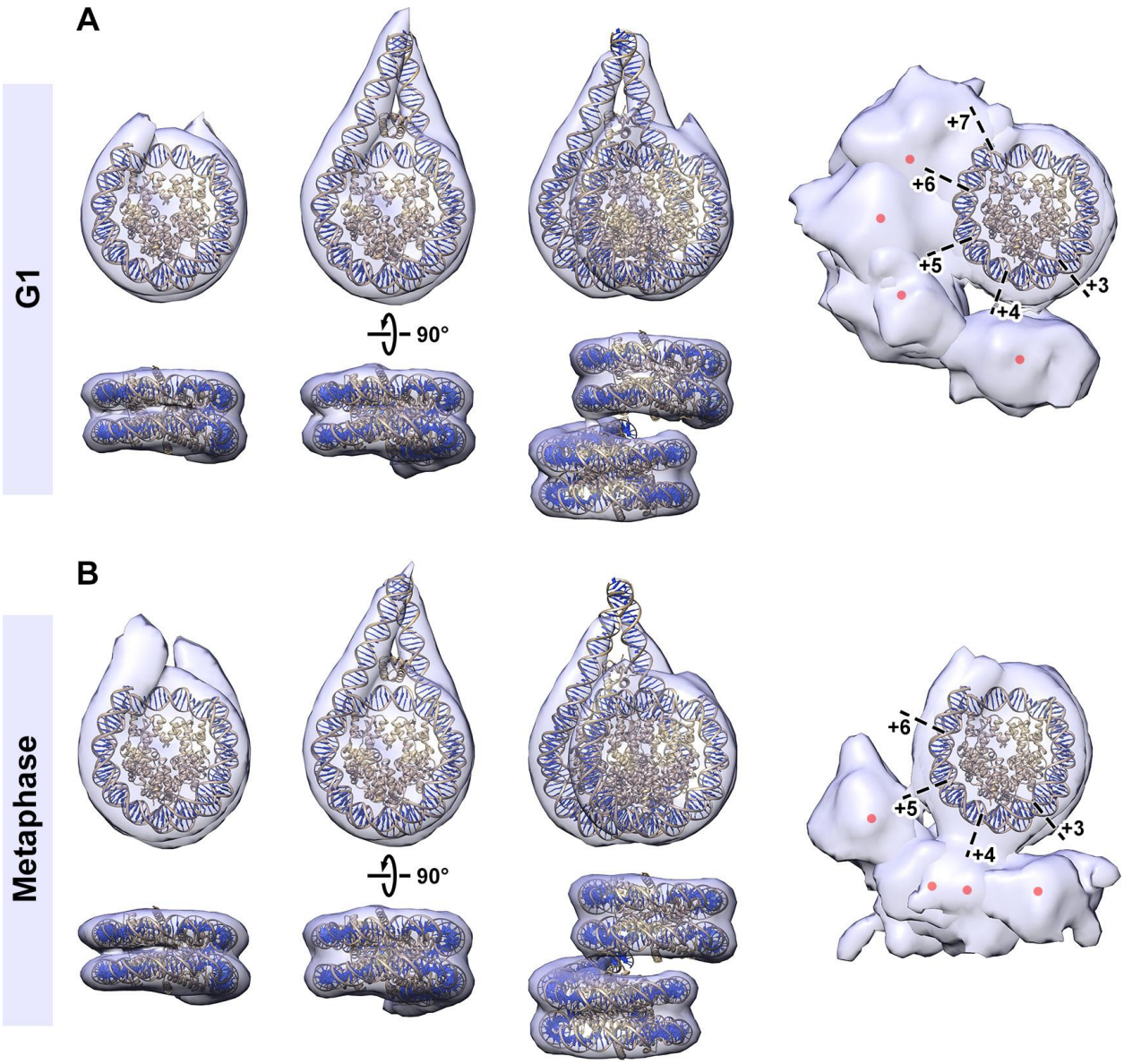

Figure 7. Comparison of G1 and metaphase nucleosomes
Crystal structures of the nucleosome core particle (PDB 1AOI) and the chromatosome (PDB 5NL0) docked into the *in situ* nucleosome subtomogram averages (transparent blue) with shorter and longer ordered linker DNA, respectively, for (**A**) G1 and (**B**) metaphase nucleosomes. For the mononucleosome and chromatosomes averages, the subtomograms from group 1 were pooled as either the shorter or longer linker nucleosomes (separately for G1 and metaphase), then jointly refined. The DNA is rendered dark blue and gold while the histones are rendered gold. The histone N-terminal tails have been omitted for clarity. For the model containing the chromatosome, the linker histone H1 was included, though the resolution of the density map is insufficient to resolve the linker histone. The nucleosome density envelopes in the right column appear larger than in the other columns because a lower contour level is used to visualize the gyre-proximal densities. Dashed black lines and numbers indicate the super-helical locations. They also have poorer definition than in earlier figures because

multiple classes are superposed here. The red dots are the approximate centers of masses of gyre-proximal densities.

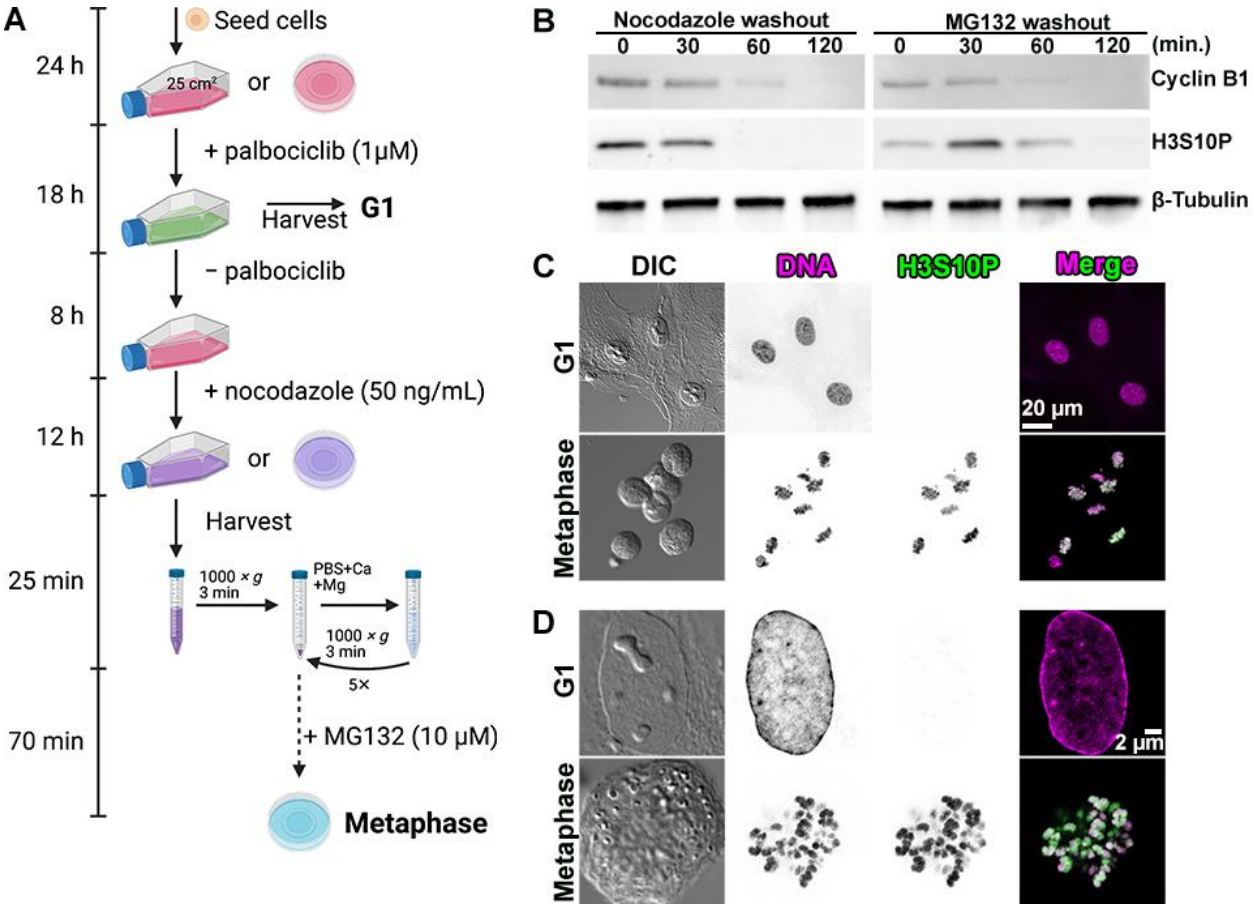

Figure S1. Synchronization scheme.
(A) Schematic of RPE-1 G1 and metaphase cell-cycle synchronization. Created with BioRender.com. (B) Immunoblot analysis showing decrease of mitotic markers cyclin B1 and histone H3 phosphorylated at serine 10 (H3S10P) 0 – 120 minutes following washout of nocodazole and MG132. β-Tubulin is the loading control. The uncropped blots are shown in **Figure S24**. (C) Differential interference contrast (DIC) and immunofluorescence images of G1 and metaphase cells. The chromatin is stained with DAPI (DNA). Immunostaining for histone H3 phosphorylated at serine 10 (H3S10P). The fluorescence contrast is inverted for better visibility. (D) Airyscan sections of a G1 and a metaphase cell, showing the localization of H3S10P in the metaphase chromosomes.

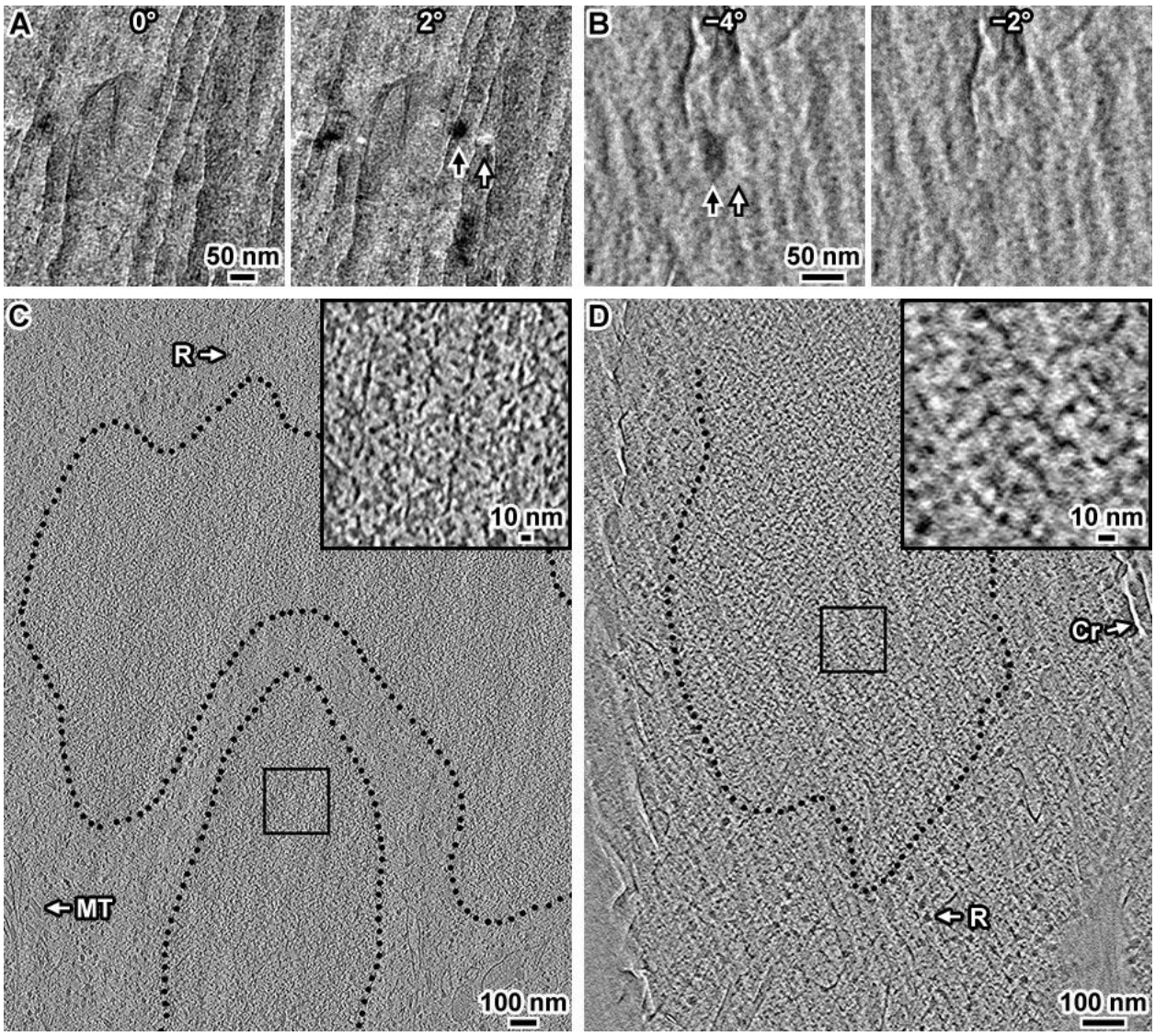

Figure S2. Cryosections of RPE-1 cells in metaphase
(A and B) Pairs of tilt series images of two RPE-1 cells. In each panel, the two images correspond to a 2° difference in tilt angle. The black and white arrows indicated diffraction contrast features that arise from crystalline ice within the cellular cryosection. The linear vertical features are crevasses. (C and D) Cryotomographic slices (12 nm) of the cells in panels A and B, respective. Cytological features such as ribosomes (R) and a microtubule (MT) are indicated. (Cr) indicates a crevasse feature. Black dotted lines indicate the approximate boundary that encloses the condensed chromosomes. The insets show 4-fold enlargements of the boxed areas in the chromosomes.

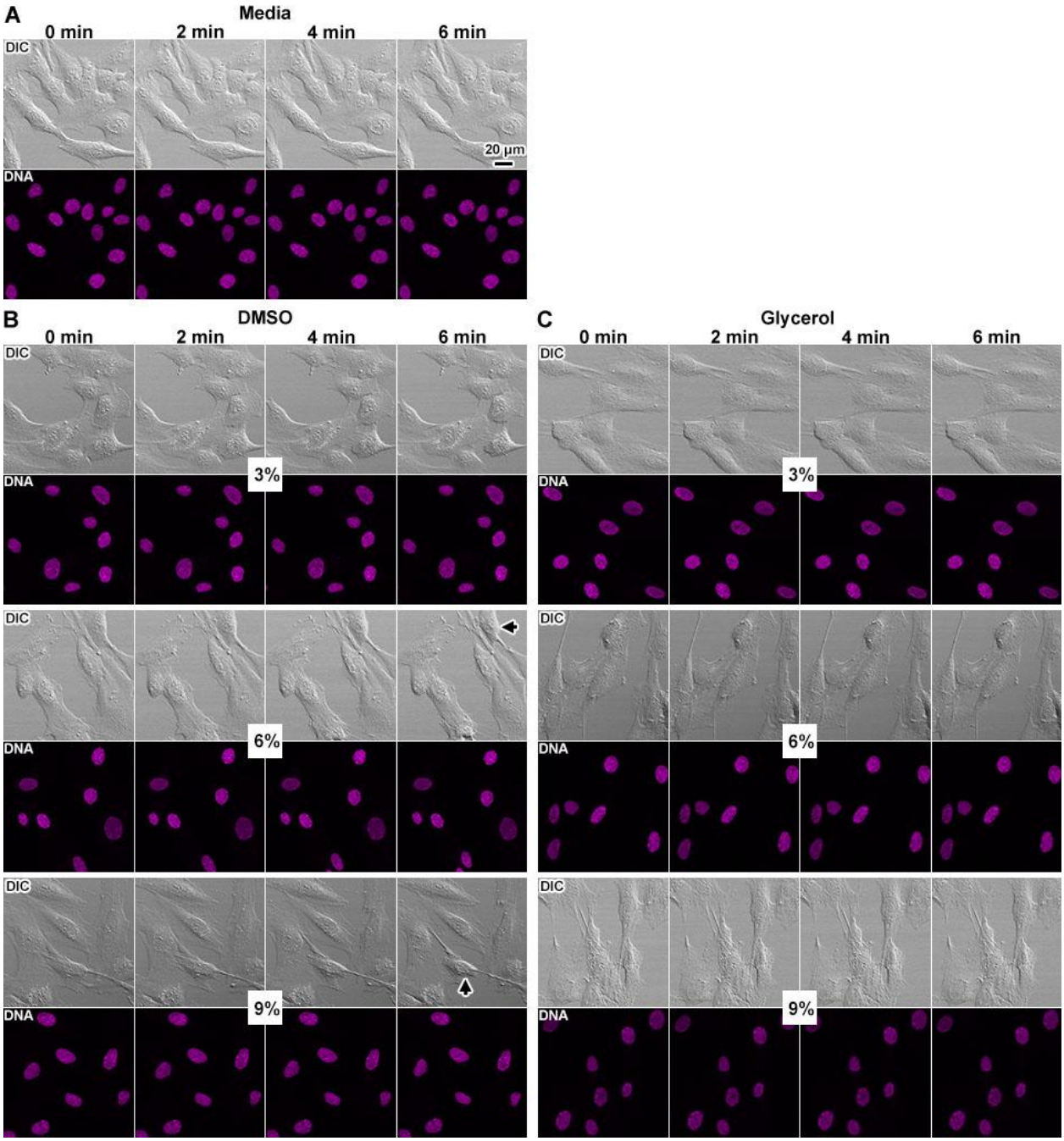

Figure S3. Screen of cryoprotectants in live cells
(A) Control timelapse images of unsynchronized RPE-1 cells in complete media and stained with Hoechst 33342, imaged every 2 minutes for 6 minutes. Images were acquired in the DIC (upper row) and Hoechst 33342 (lower row) channels. The experimental delay between the addition of cryoprotectant and the acquisition of the first image is estimated to be 1 minute. Timelapse imaging was done for cells in either (B) DMSO or (C) glycerol, at three different concentrations (3%, 6%, and 9%). The short arrows in panel B indicate cells that have started to detach.

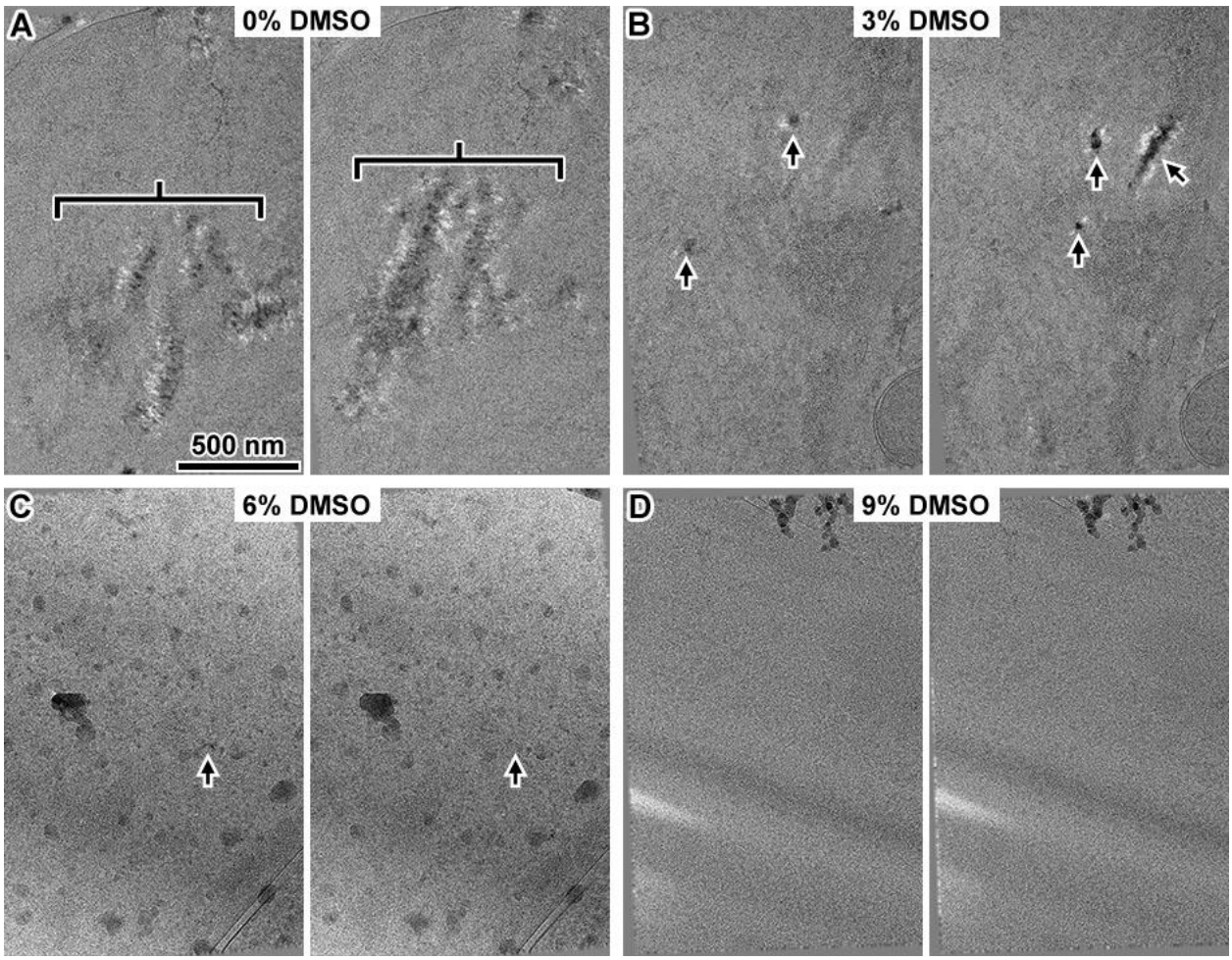

Figure S4. Test of DMSO as a cryoprotectant for cryolamellae
Example G1-arrested RPE-1 cells, grown on EM grids, were briefly dipped in PBS+Ca+Mg supplemented with (A) 0%, (B) 3%, (C) 6%, or (D) 9% DMSO. The cells were then plunge-frozen, cryo-FIB milled, and imaged as a tilt series. To ensure that all four freezing conditions were tested on samples of similar thickness, the tilt series were collected at the nuclear periphery. Distinct nuclear double membranes (nuclear envelope) were observed for all tilt series, indicating that the sampled heights were indeed at the nuclear periphery. Note that the double membranes are not clear in panels B and D but are visible in the reconstructed cryotomograms. For each image pair, the tilt angle differed by 2°. The ice-crystal diffraction-contrast features are indicated by the brackets in panel A and short arrows in panel B. In panel C, the dense ~100- to 200-nm rounded features are ice-crystal contaminants on the lamella's surface. In panel D, the bright and dark streaks oriented 10 to 4 o'clock are from uneven milling.

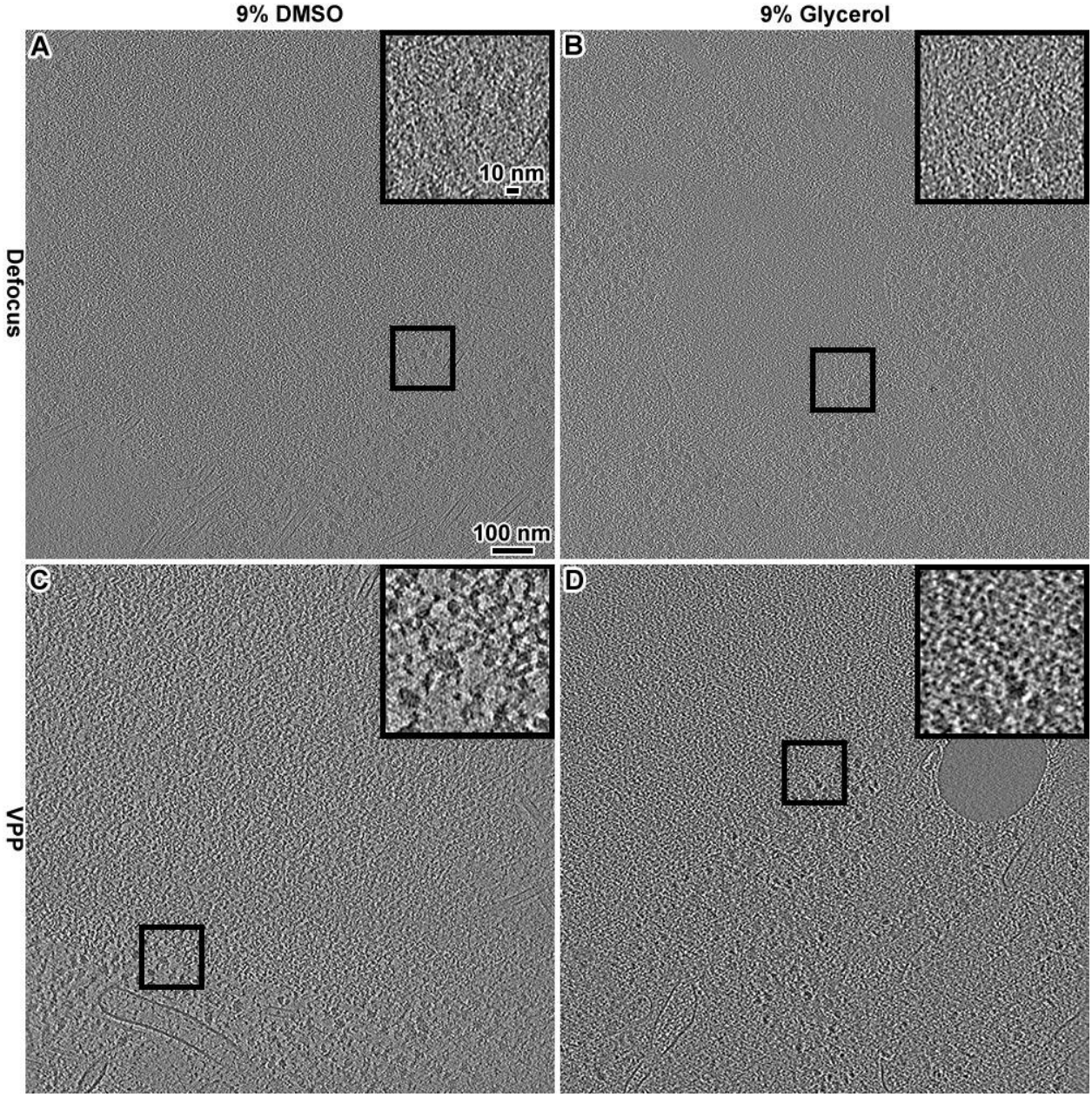

Figure S5. Tests of intracellular cryo-ET contrast in cryoprotectants
Cryotomographic slices (12 nm) of metaphase-arrested RPE-1 cells frozen in (A) 9% DMSO and imaged by defocus phase contrast (Defocus), (B) 9% Glycerol and imaged by defocus phase contrast, (C) 9% DMSO and imaged with a Volta phase plate (VPP), (D) 9% Glycerol and imaged with a VPP. The fitted defocus was −5 µm in panels A and B and the nominal defocus was −0.5 µm in panels C and D. Insets show 3-fold enlargements of the corresponding boxed areas. A region that has both ribosomes and chromatin was chosen for each inset.

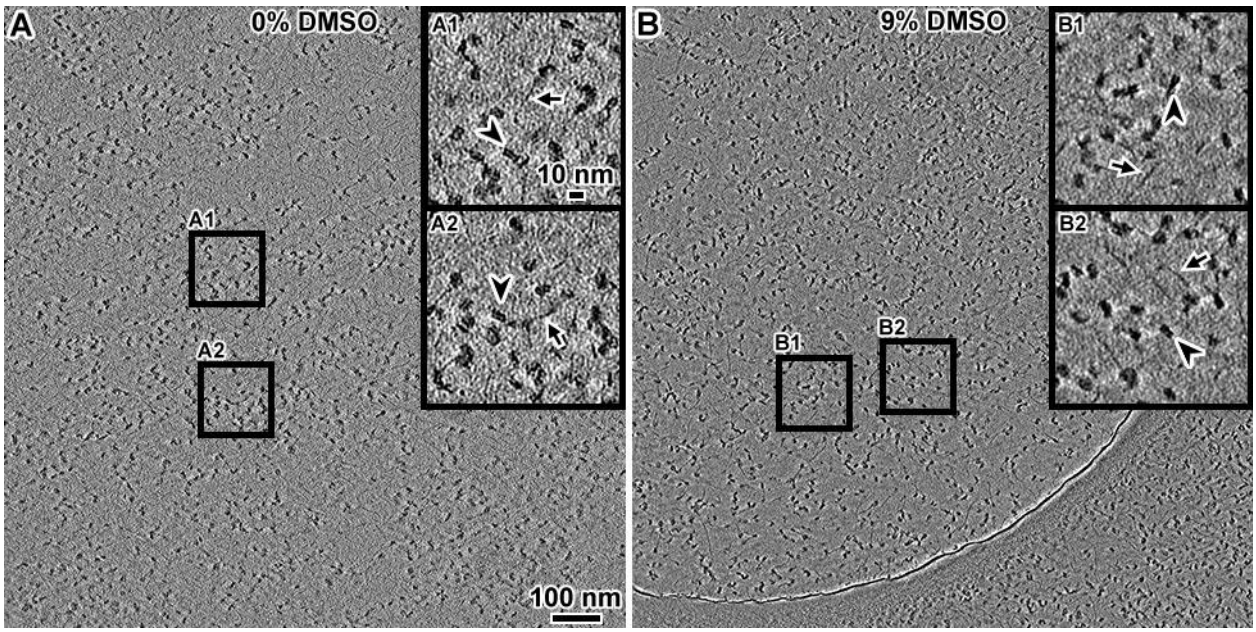

Figure S6. Control cryo-ET of oligonucleosomes in DMSO cryoprotectant
Volta cryotomographic slices (10 nm) of HeLa oligonucleosomes in (A) storage buffer and (B) storage buffer plus 9% v/v DMSO. The granular densities are the nucleosomes. The large arc-shaped feature in the lower portion of panel B is the edge of the holey-carbon support film. The insets show 3-fold enlargements of boxed regions. Stretches of naked DNA (short arrows) and nucleosome double-gyre motifs (arrowheads) are indicated.

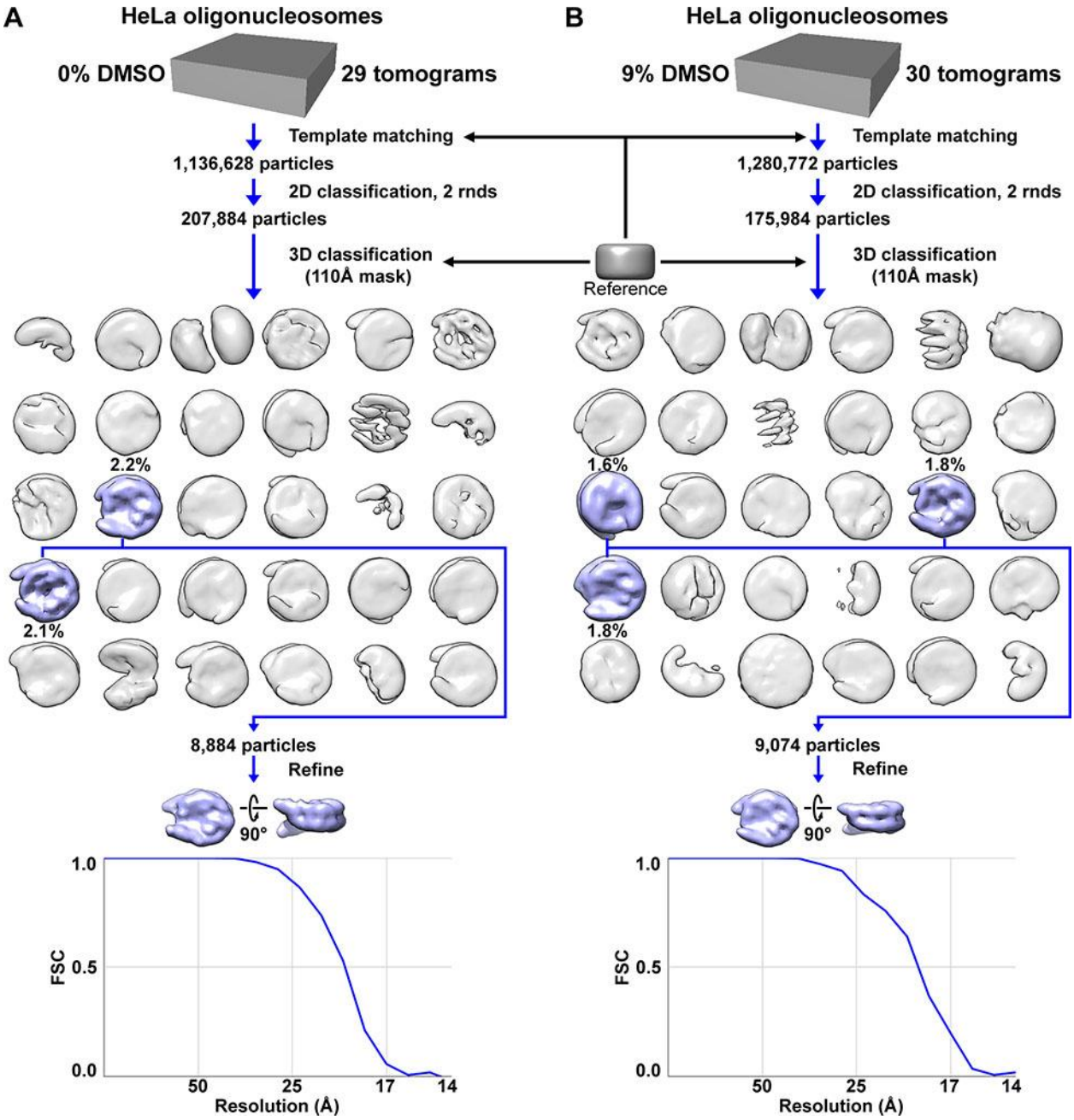

Figure S7. Classification of HeLa oligonucleosomes in 0% and 9% DMSO
Classification and subtomogram analysis of oligonucleosomes in (A) 0% DMSO control and (B) 9% DMSO. Nucleosome-like particles were template matched using a 10-nm-wide, 6-nm-thick smooth cylindrical reference. Then two sequential rounds of 2-D classification were performed. The second round is shown, with the selected nucleosome-like particles boxed in red. One round of 3-D classification using k = 30 classes was done. The canonical nucleosomes with the higher-resolution features (those that didn't have smooth surfaces) were combined for 3-D refinement. Based on the Fourier shell correlation (FSC) = 0.5 cutoff criterion, the resolution of the 0% and 9%-DMSO-treated oligonucleosomes class averages were 19 Å and 19.5 Å, respectively.

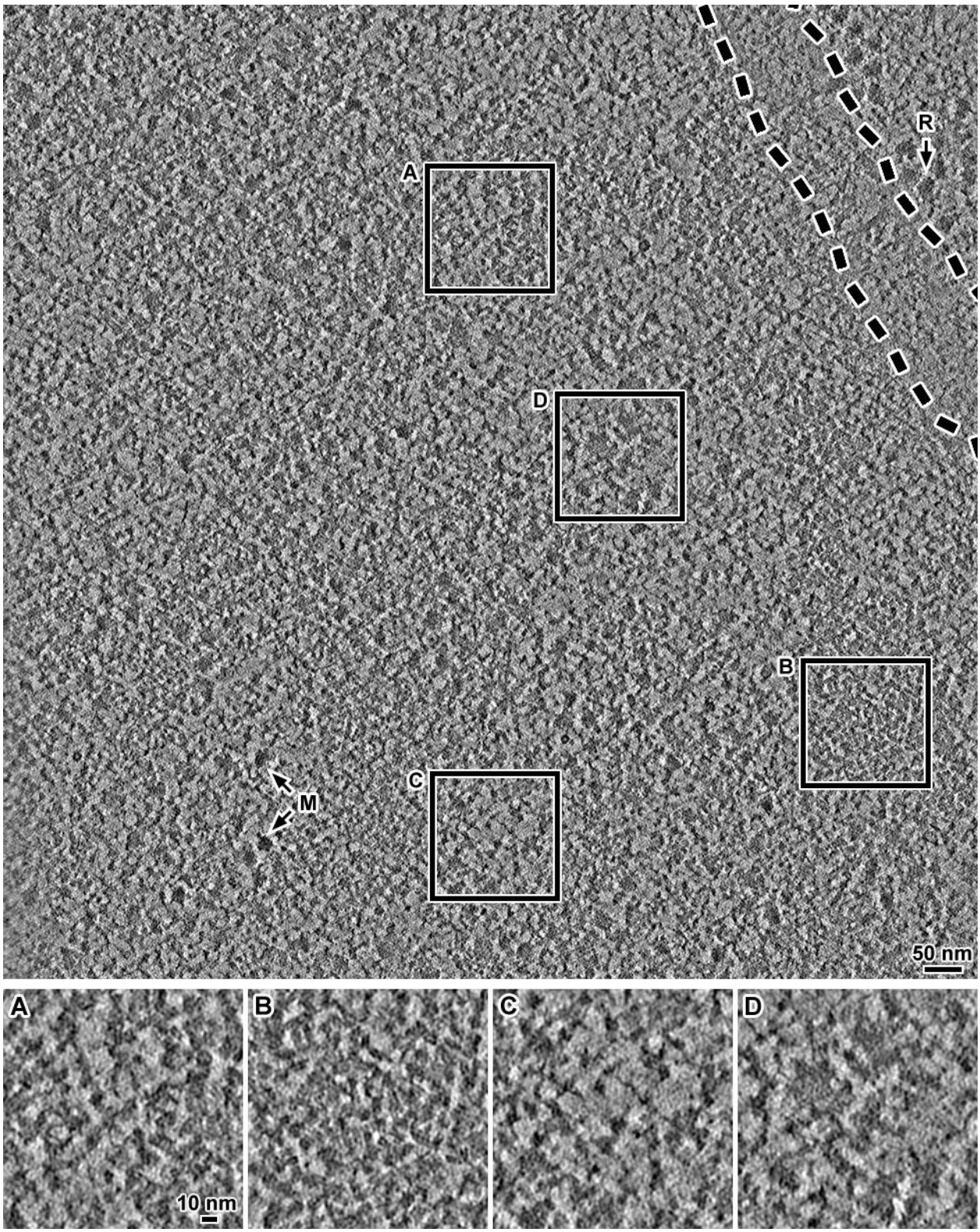

Figure S8. Additional example Volta cryotomographic slice of a G1 cell
Cryotomographic slice (20 nm) of nuclear densities centered near the nuclear envelope of an RPE-1 cell. Rendered with low JPEG compression. Insets show 2-fold enlargements of (A and B) portions of chromatin domains, (C) region with fewer

macromolecular complexes, and (D) a region with many megacomplexes. Cytological features are highlighted: megacomplex (M); ribosome (R). The region between the two dashed lines is the lumen of the nuclear envelope, which is oriented obliquely to the milling direction. As such, the nuclear envelope membranes are not visible.

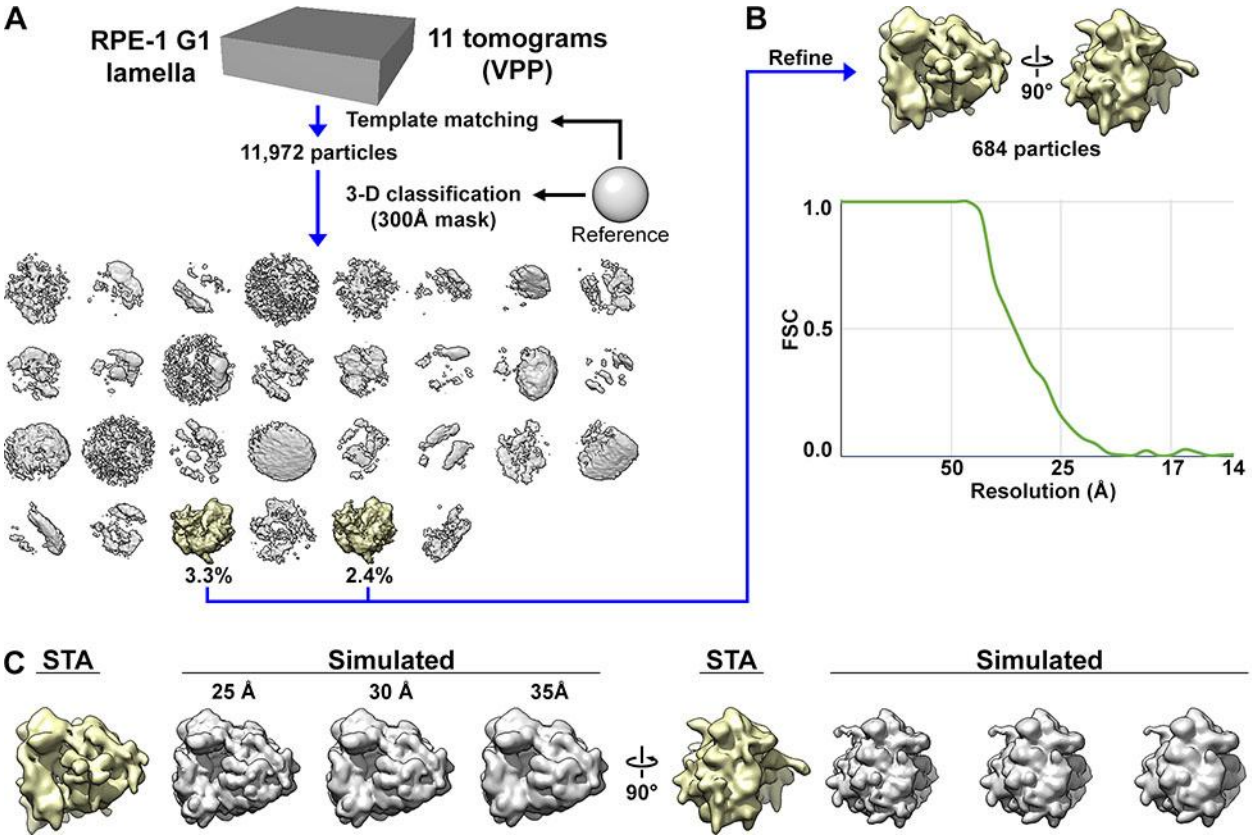

Figure S9. Controls subtomogram analysis of ribosomes *in situ*
(A) Template matching was done only on the cytoplasmic regions, using a spherical reference. The template-matching hits were then subjected to direct 3-D classification (also using a spherical reference), revealing numerous non-ribosome class averages (gray) and two 80S ribosome class averages (yellow). (B) The particles of these two class averages were combined and refined to ~33 Å resolution, based on the FSC = 0.5 criterion. (C) The (yellow) refined *in situ* 80S ribosome density map reproduced from panel B, alongside (gray) density maps of purified human ribosomes (4UG0) (Khatter et al., 2015) simulated at different resolutions.

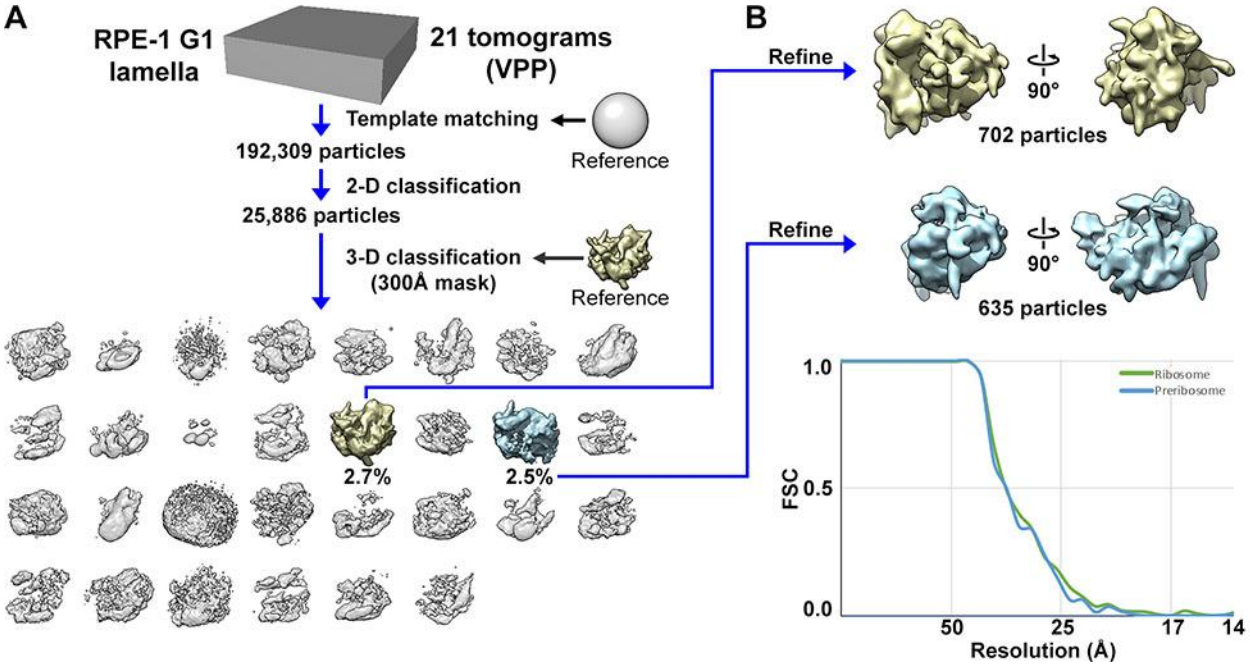

Figure S10. Subtomogram analysis of preribosomes
(A) Template matching for preribosomes was performed on all cryotomograms containing nuclear regions, using a spherical reference. The candidate hits were then subjected to 2-D classification; classes that contain subtomograms that do not correspond to large complexes were removed. The remaining subtomograms were then subjected to 3-D classification, using the ribosome refined class average shown in Figure S9B as the reference, but low-pass filtered to 60 Å resolution. (B) The preribosome (blue) class average was refined to ~32 Å resolution, based on the FSC = 0.5 criterion. The 80S ribosome average (yellow) is also shown for comparison purposes. The preribosome resembles the 60S subunit of the mature ribosome and is oriented to better show their similarities.

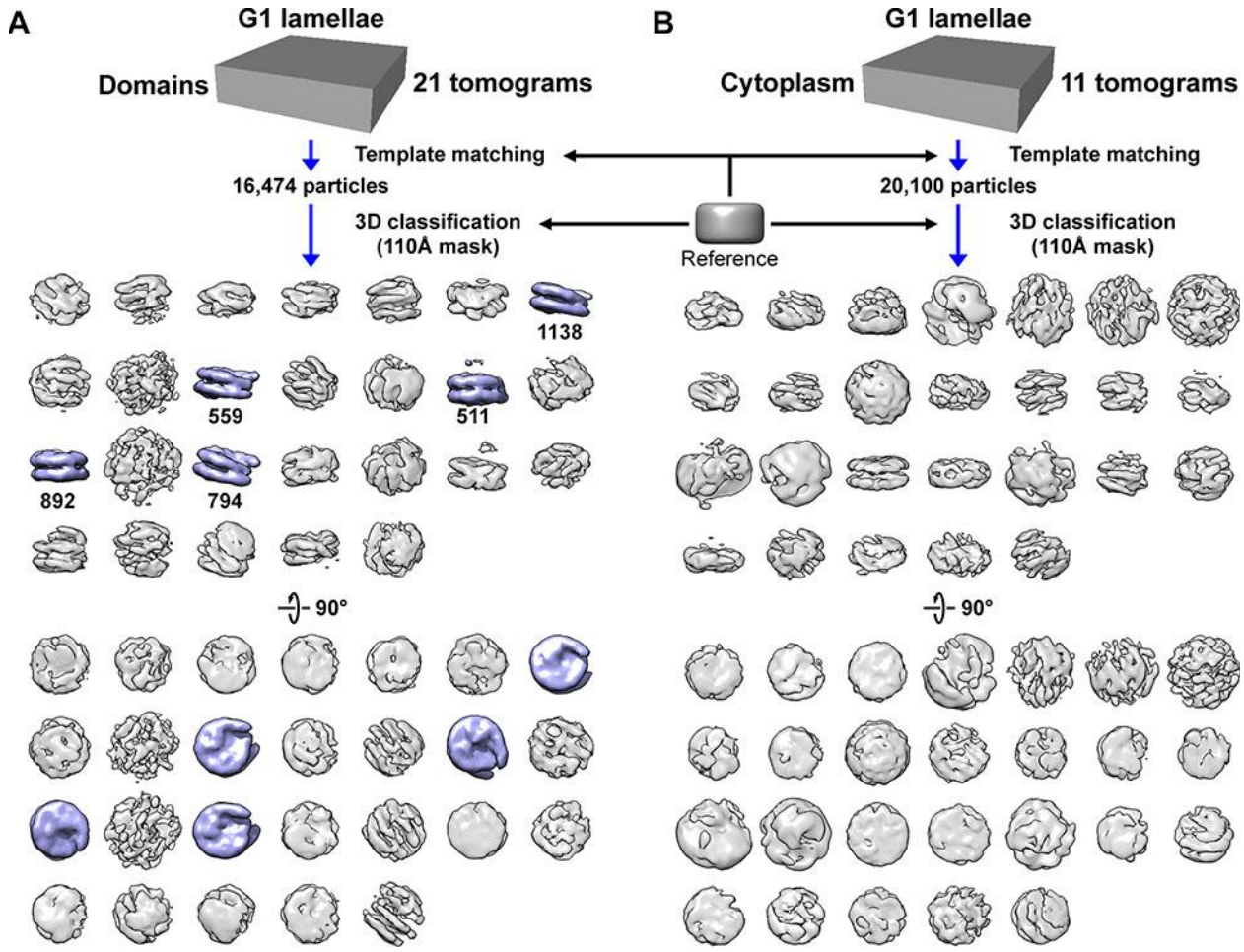

Figure S11. Controls for nucleosome 3-D classification *in situ*.
(A) Subtomogram analysis of G1 chromatin domains. (B) Subtomogram analysis of G1 cytoplasm. Template matching was done with a featureless cylinder reference and a 110 Å spherical mask. The grid spacing for both template matching experiments was 21 nm. The same reference and mask were used for both datasets. Canonical nucleosome class averages are shaded in blue while ambiguous class averages are shaded in gray. Classification was done using 30 classes for each experiment. Some classes had too few particles and were therefore not shown.

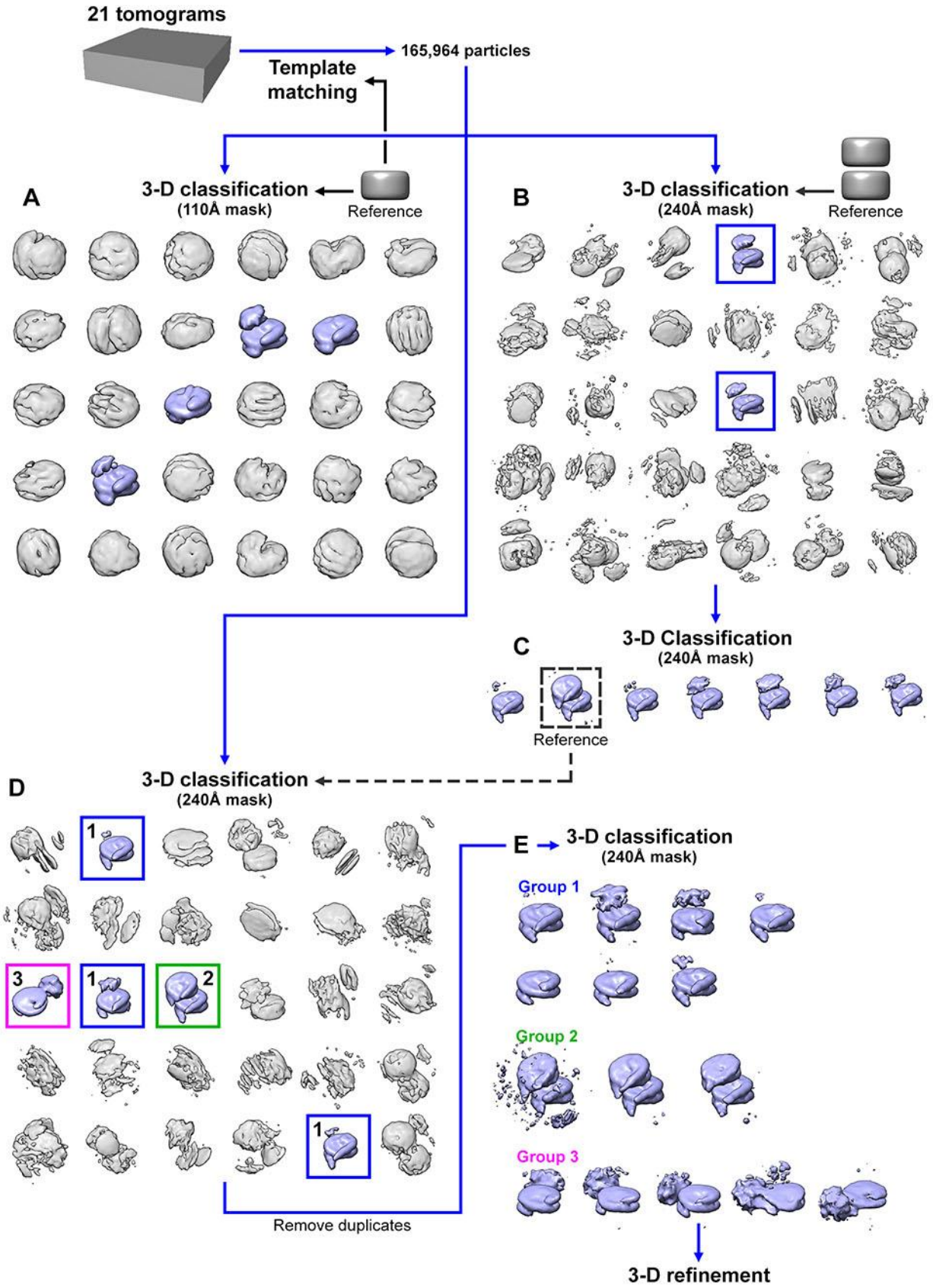
21 tomograms
165,964 particles
Template matching
A
3-D classification
(110Å mask)
Reference
B
3-D classification
(240Å mask)
Reference
C
3-D Classification
(240Å mask)
Reference
D
3-D classification
(240Å mask)
1
3
1
2
1
Remove duplicates
E
3-D classification
(240Å mask)
Group 1
Group 2
Group 3
3-D refinement

Figure S12. Classification flowchart of G1 chromatin domains
(A) G1 candidate nucleosome subtomograms that were template matched with a cylindrical reference were directly classified in 3-D, using a cylindrical reference and a 110 Å spherical mask. Note that there are more template-matching hits in this set of experiments than that of Figure S11 because a smaller grid spacing was used here. (B) In parallel, the same set of subtomograms were directly classified in 3-D using a stacked cylinder reference and a larger spherical mask. (C) A second round of classification using a nucleosome class average from panel B as the reference and the larger mask yielded mononucleosomes with extra densities at their face plus an unambiguous dinucleosome class. (D) Direct 3-D classification was done on the original set of subtomograms using a larger mask and the stacked dinucleosome class average from panel C as the reference. Three groups of class averages were obtained, corresponding to (1) mononucleosome, (2) stacked dinucleosome, and (3) mononucleosome with a gyre-proximal density. (E) These three groups of class averages were subjected to a third round of classification using either a mononucleosome, stacked dinucleosome or mononucleosome with a gyre-proximal density from C as the reference and large spherical mask.

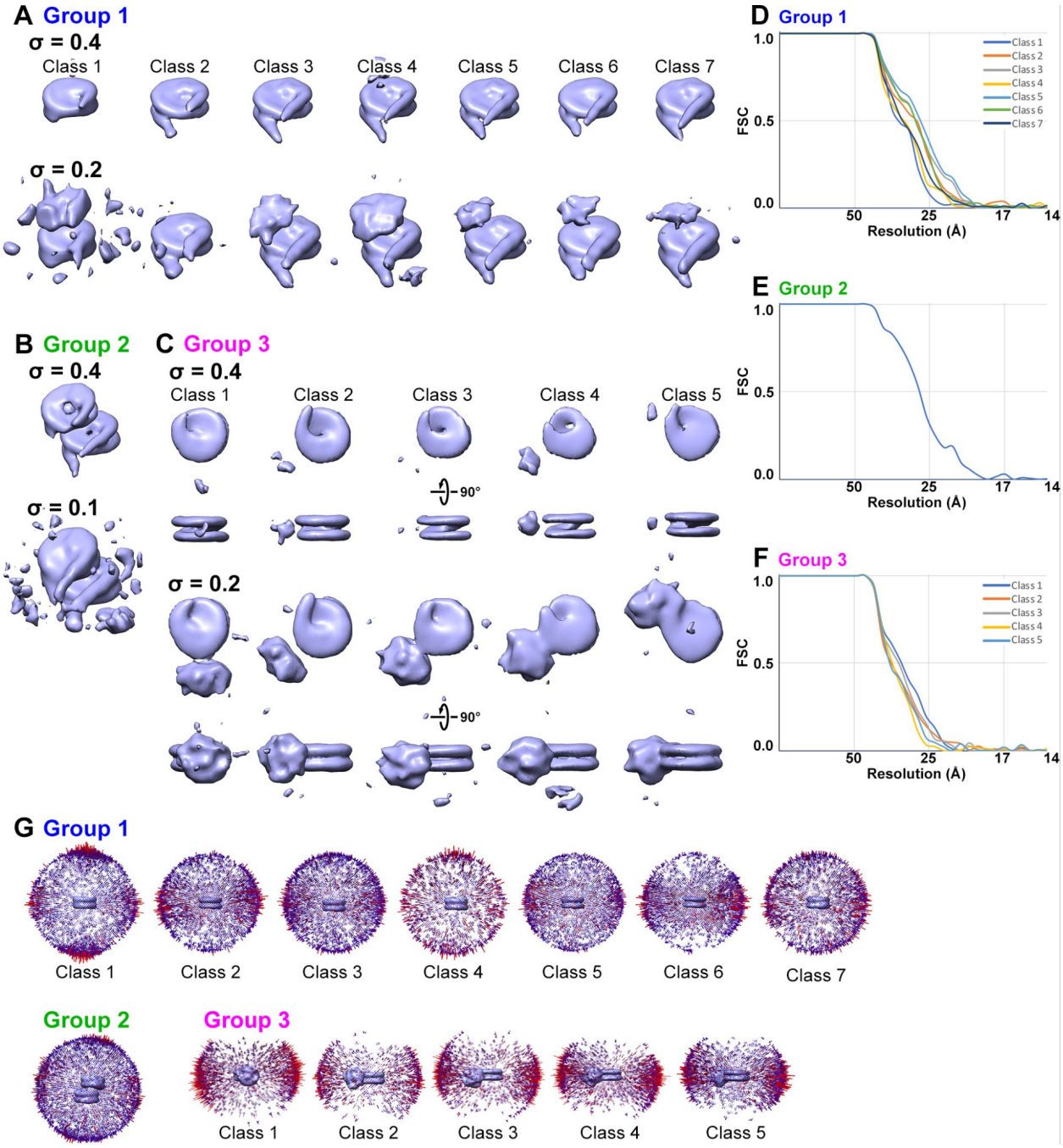

Figure S13. Refinement of G1 mononucleosomes and dinucleosomes. Refined class averages for (A) mononucleosomes, (B) stacked dinucleosomes, and (C) mononucleosomes with a gyre-proximal density. Two contour levels are shown for each class average. (D, E, F) FSC plots and (G) angular distribution of the refined density maps. For panels A – C, the hide dust feature in UCSF Chimera was disabled.

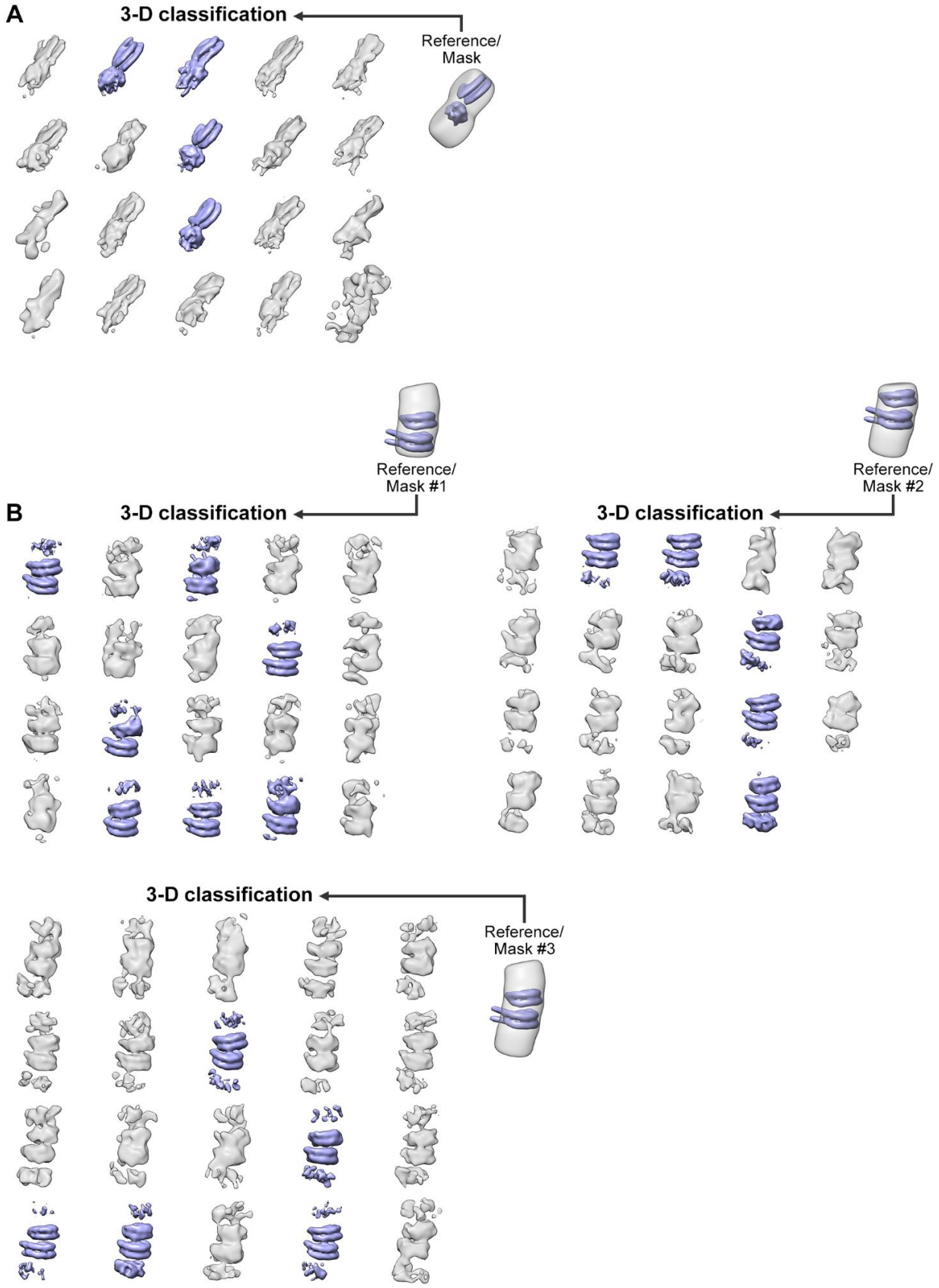
A
3-D classification
Reference/
Mask
B
3-D classification
Reference/
Mask #1
3-D classification
Reference/
Mask #2
3-D classification
Reference/
Mask #3

Figure S14. Subtomogram analysis of alternative ordered nucleosome packing motifs in G1 cells

Nucleosome particles from Groups 2 and 3 (Figures S13 B and C, respectively) were subjected to an additional round of 3-D classification, using custom masks that enclose volumes where an additional complex may reside. Since the particles were already aligned from the previous refinement step, a restricted angular search range was imposed for these runs. The “reference/mask” models in the figure depicts the location of the volume masked-in (gray), relative to the reference (blue) used for each classification run. The masks used for these 3-D classification runs were optimized for (A) side-by-side nucleosomes and (B) ordered trinucleosomes and tetranucleosomes. Class averages that contain at least one ordered nucleosome are shaded blue.

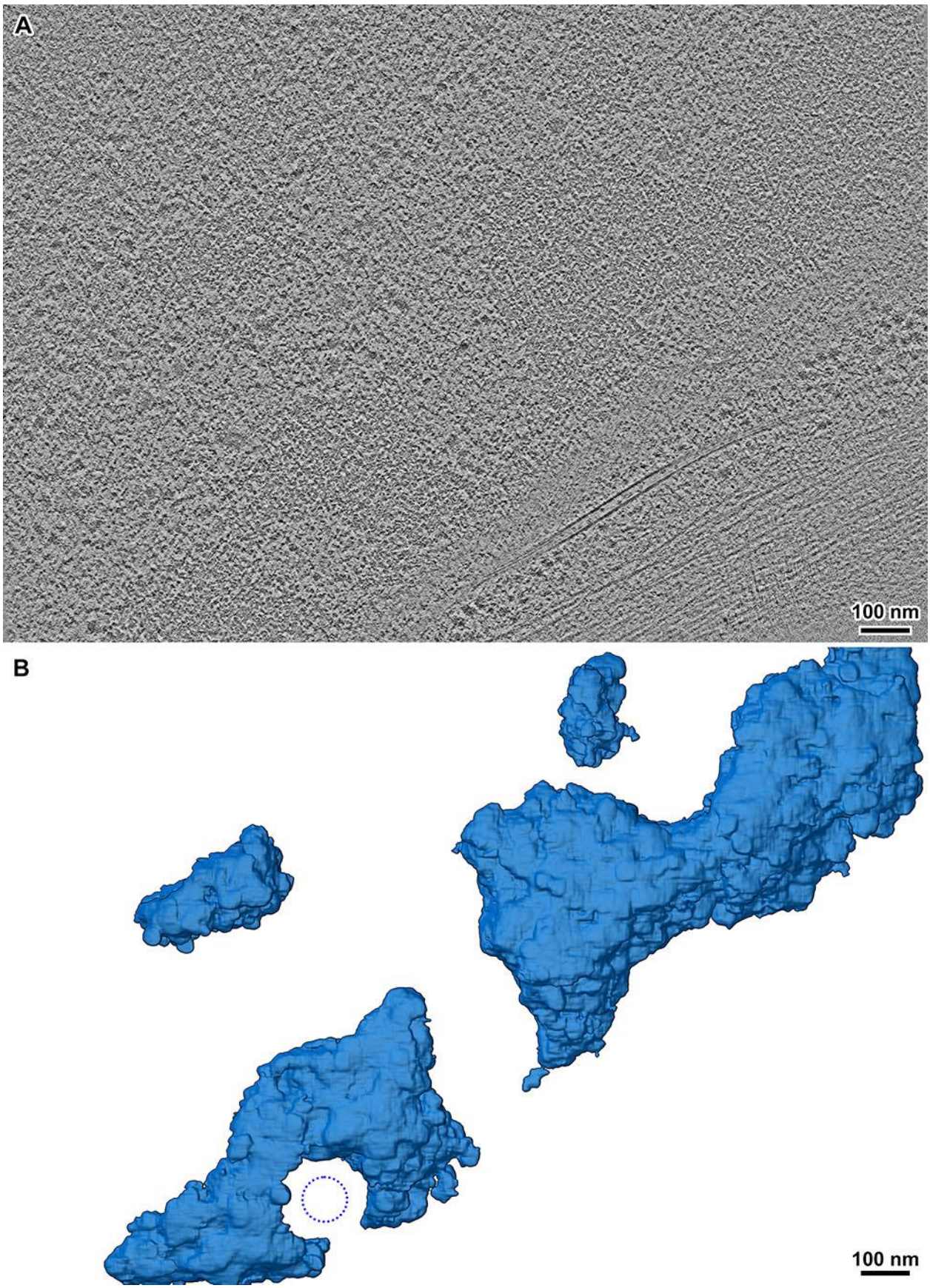
A
100 nm
B
100 nm

Figure S15. G1 chromatin domains are irregular
(A) Cryotomographic slice a region near the nuclear envelope. (B) Convolutional neural network (CNN) based segmentation of the region in panel A. For clarity, the CNN segmentation rendering shows the entire ~90 nm thickness of the lamella whereas the cryotomographic slice shows the central 10 nm. Because of this difference, the CNN segmentation shows more chromatin than is visible in the cryotomographic slice. The dotted blue circle indicates the approximate position of the nuclear pore complex (not segmented).

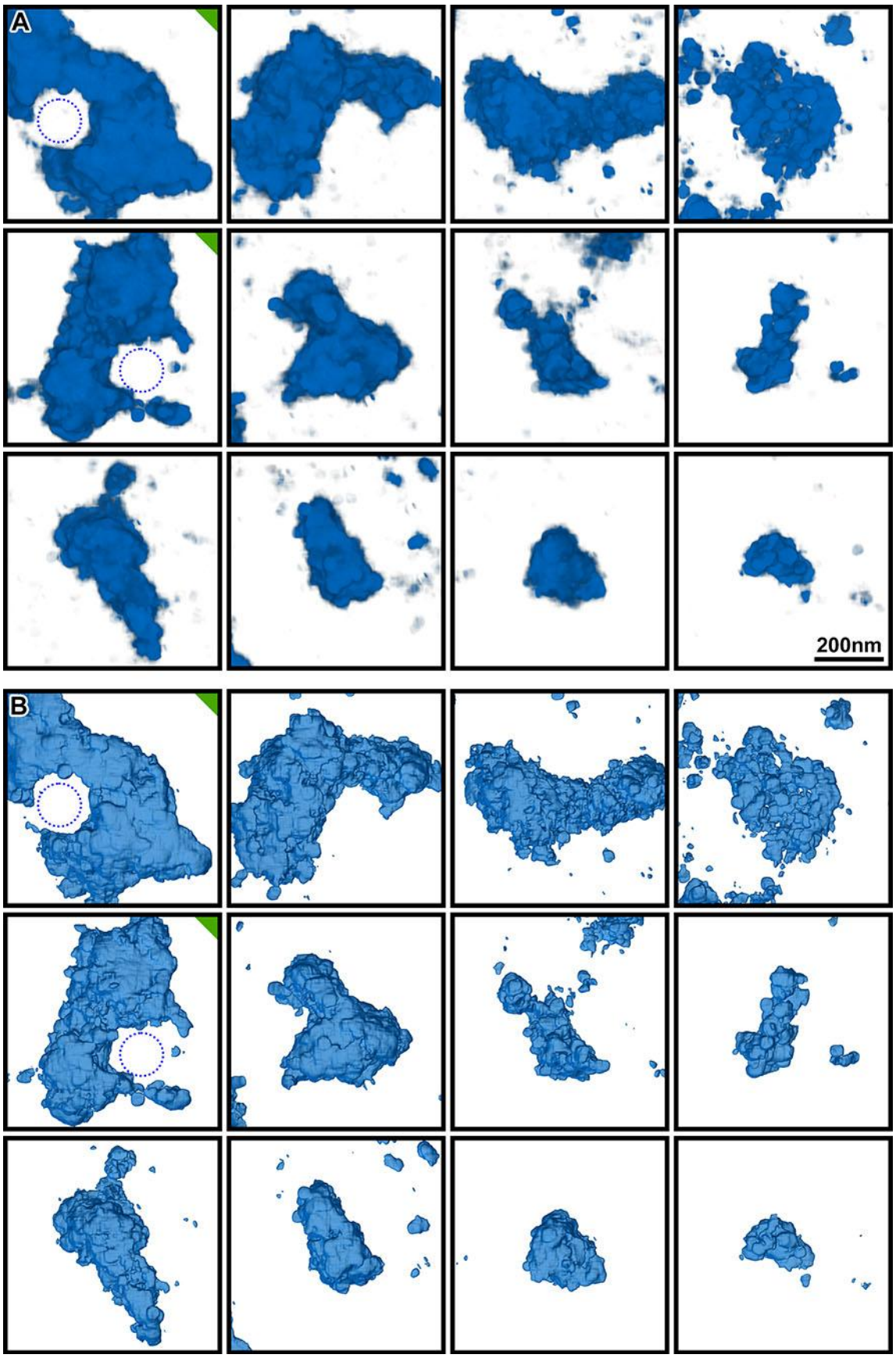
A
200nm
B

Figure S16. Additional CNN annotations of chromatin domains in G1 nuclei.
(A) Volume and (B) isosurface renderings of chromatin domains. Panels marked with a green triangle contain perinuclear chromatin domains. The dotted blue circles indicate the approximate positions of nuclear pore complexes (not segmented).

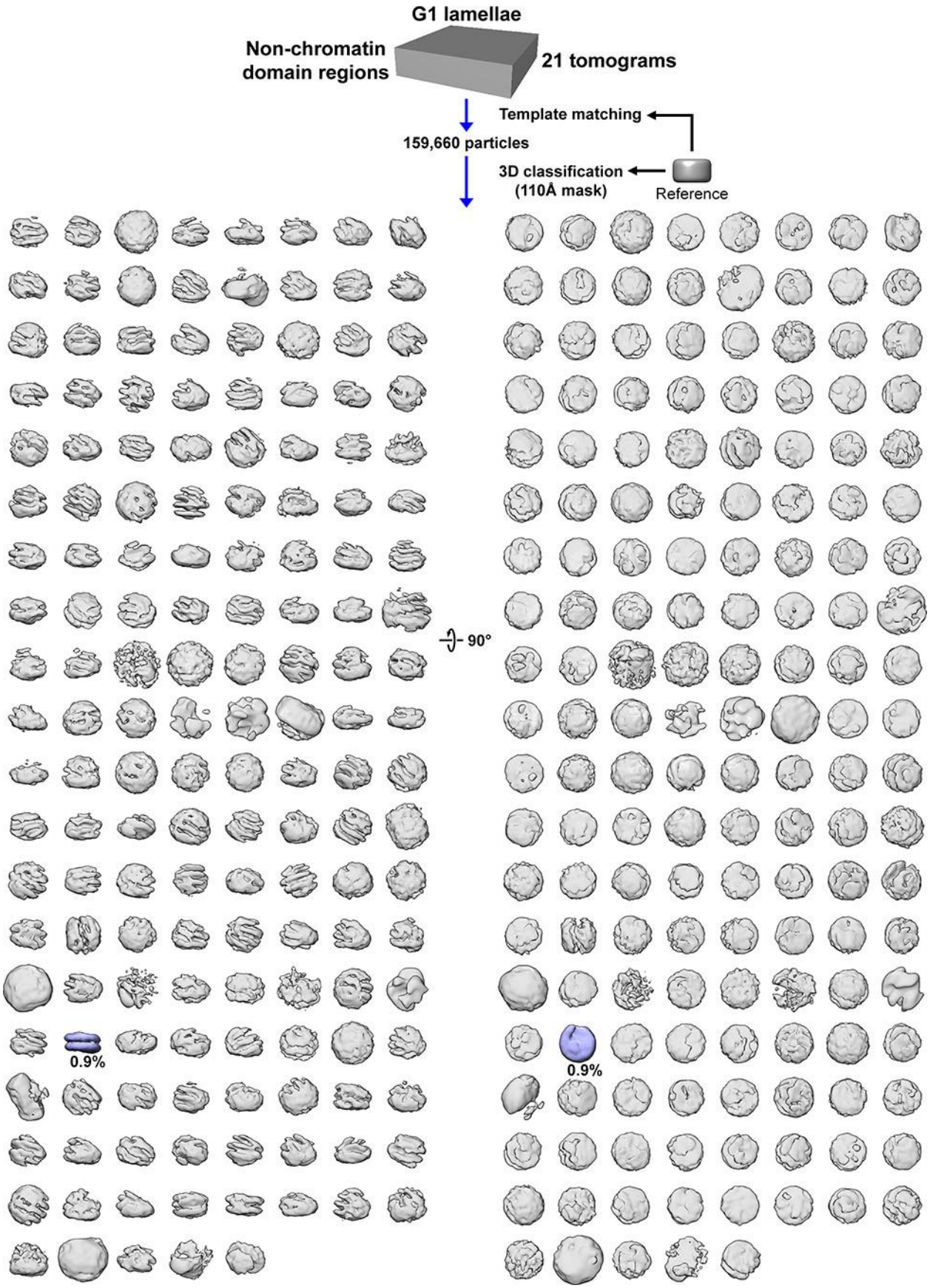
G1 lamellae
Non-chromatin domain regions
21 tomograms
Template matching
159,660 particles
3D classification (110Å mask)
Reference
90°
0.9%
0.9%

Figure S17. Subtomogram analysis of the G1 nucleoplasm
The regions outside the chromatin domains were template matched with a featureless cylinder reference. The template-matching hits were then subjected to direct 3-D classification with 200 classes using the same featureless cylinder as the reference. Out of the 157 non-empty classes, the vast majority do not resemble canonical nucleosomes (gray). Only one canonical nucleosome class average was detected (blue), but the subtomograms from this class were mostly located at the periphery of chromatin domains.

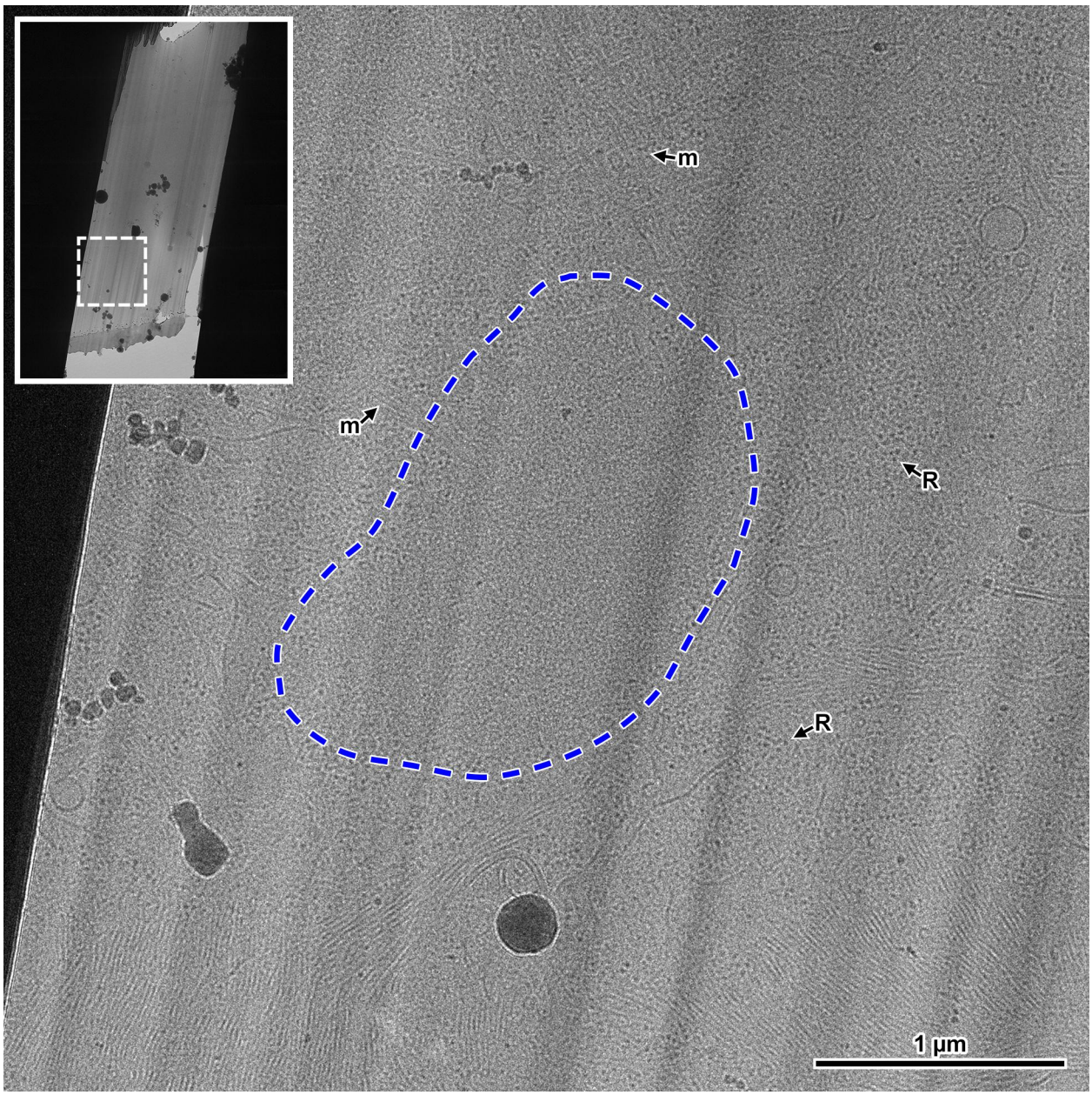

Figure S18. Targeting images for chromatin in metaphase cells.
Inset shows a montage of an entire lamella–the area bounded by the white dashed line corresponds to the location of the enlarged view. The region indicated by the blue dashed line contains chromatin and is shown at higher magnification as a cryotomographic slice in Figure 4C. Microtubules (m) and ribosomes (R) are also observed, and guided tilt-series target selection.

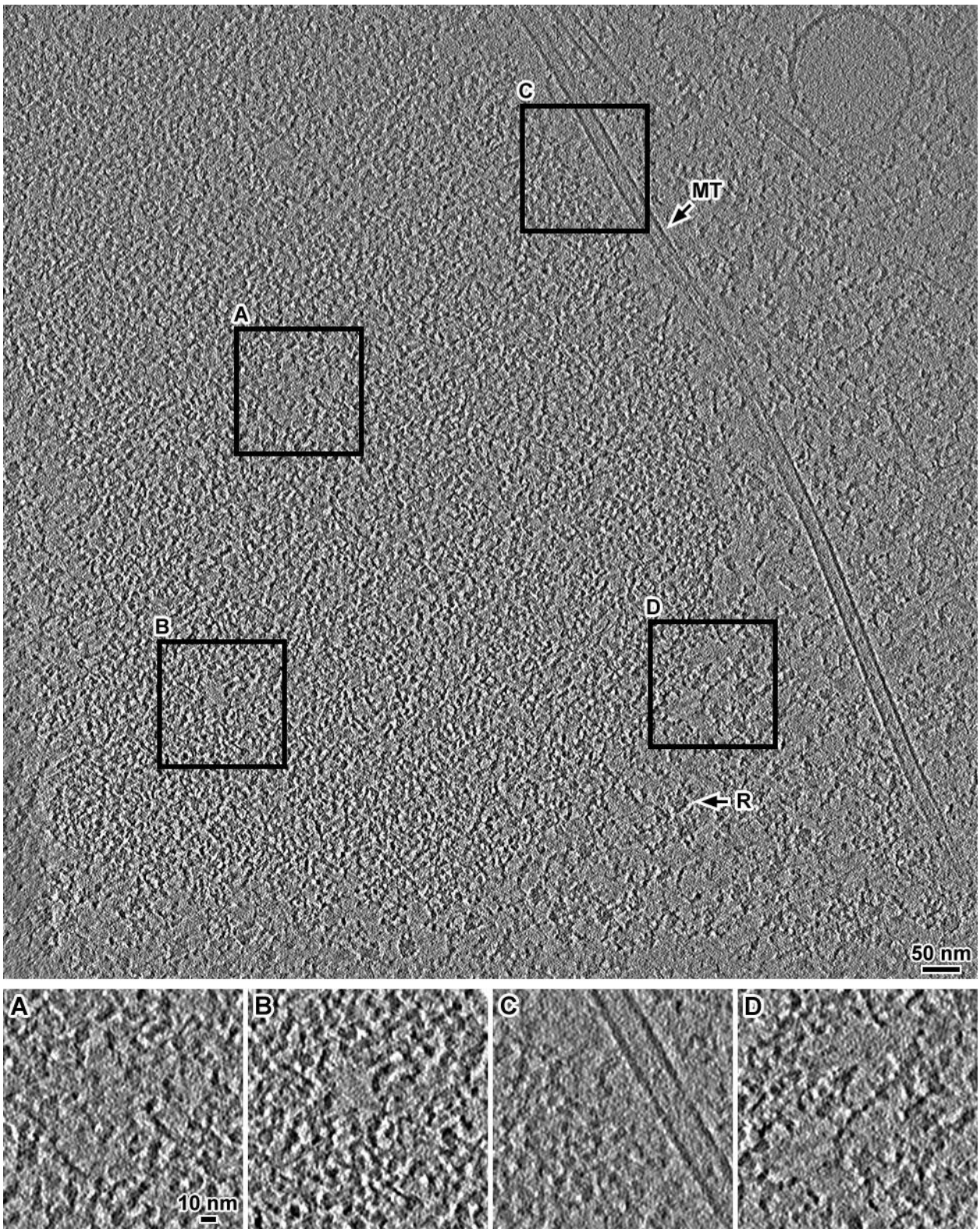

Figure S19. Additional example Volta cryotomographic slice of a metaphase cell
Cryotomographic slice (20 nm) centered on a mitotic chromatin in a metaphase RPE-1 cell. Rendered with low JPEG compression. Insets show 2-fold enlargements of nucleosome-free pockets inside the chromosome (A and B) and the chromosome

periphery (C and D). Cytological features are highlighted: ribosome (R); microtubule (MT).

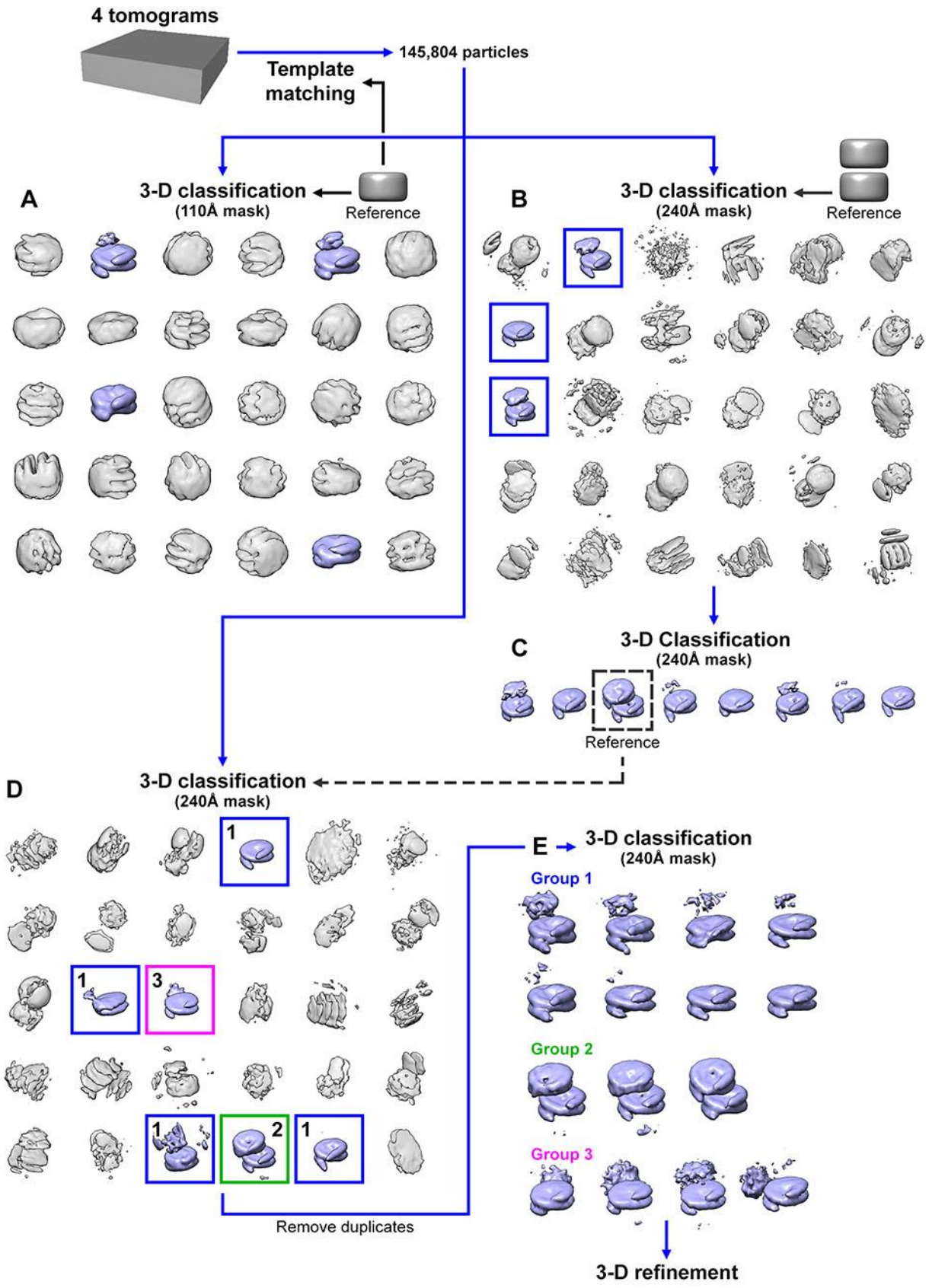
4 tomograms
145,804 particles
Template matching
A
3-D classification
(110Å mask)
Reference
B
3-D classification
(240Å mask)
Reference
C
3-D Classification
(240Å mask)
Reference
D
3-D classification
(240Å mask)
1
1
3
1
2
1
Remove duplicates
E
3-D classification
(240Å mask)
Group 1
Group 2
Group 3
3-D refinement

Figure S20. Classification flowchart of M cells
(A) Metaphase candidate nucleosome subtomograms that were template matched with a cylindrical reference were directly classified in 3-D, using a cylindrical reference and a 120 Å spherical mask. (B) In parallel, the same set of subtomograms were directly classified in 3-D using a stacked cylinder reference and a larger spherical mask. (C) A second round of classification using a nucleosome class average from B as the reference and the larger mask yielded mononucleosomes with extra densities at their face plus an unambiguous dinucleosome class. (D) Direct 3-D classification was done on the original set of subtomograms using a larger mask and the stacked dinucleosome class average from panel C as the reference. Three groups of class averages were obtained, corresponding to (1) mononucleosome, (2) stacked dinucleosome, and (3) mononucleosome with a gyre-proximal density. (E) These three groups of class averages were subjected to a third round of classification using either a mononucleosome, stacked dinucleosome or mononucleosome with a gyre-proximal density from C as the reference and large spherical mask.

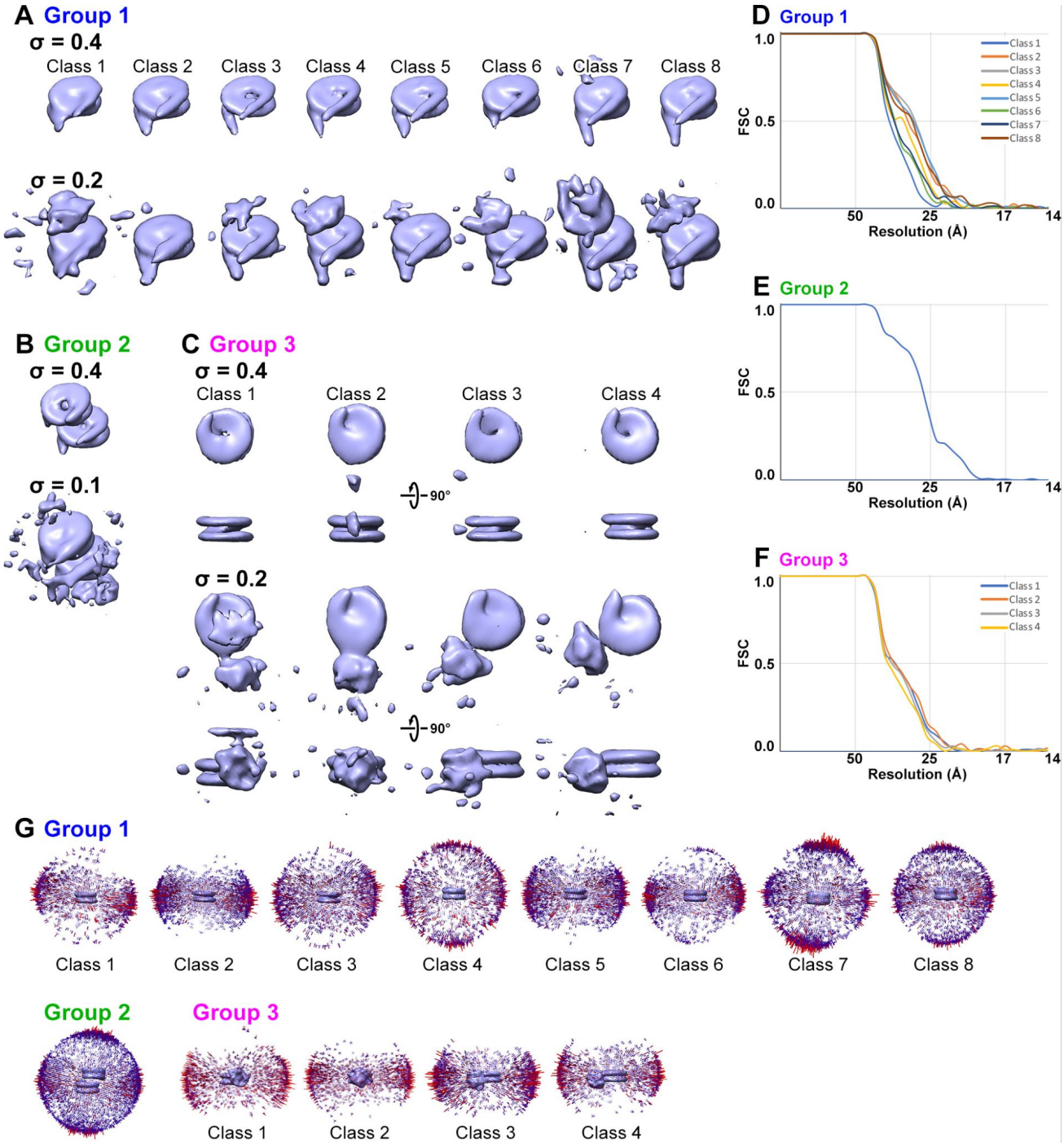

Figure S21. Refinement of metaphase mononucleosomes and dinucleosomes
Refined class averages for (A) mononucleosomes, (B) stacked dinucleosomes, and (C) mononucleosomes with a gyre-proximal density. Two contour levels are shown for each class average. (D, E, F) FSC plots and (G) angular distribution of the refined density maps. For panels A – C, the hide dust feature in UCSF Chimera was disabled.

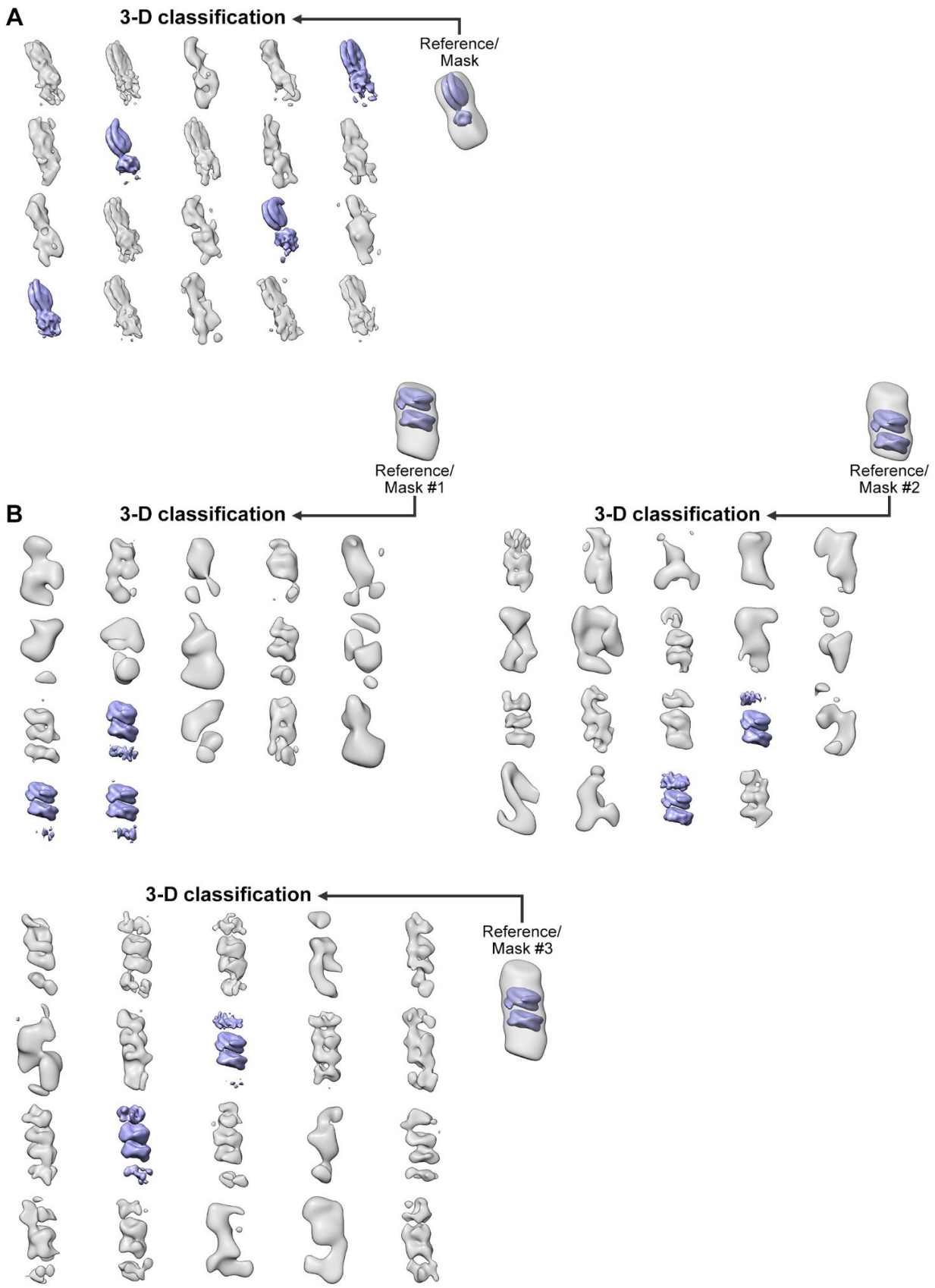
A
3-D classification
Reference/
Mask
B
Reference/
Mask #1
3-D classification
Reference/
Mask #2
3-D classification
3-D classification
Reference/
Mask #3

Figure S22. Subtomogram analysis of alternative ordered nucleosome packing motifs in metaphase cells

Similar to Figure S14, nucleosome particles from Groups 2 and 3 (Figures S21 B and C, respectively) were subjected to an additional round of 3-D classification, using custom masks that enclose volumes where an additional complex may reside. Since the particles were already aligned from the previous refinement step, a restricted angular search range was imposed for these runs. The “reference/mask” models in the figure depicts the location of the volume masked-in (gray), relative to the reference (blue) used for each classification run. The masks used for these 3-D classification runs were optimized for (A) side-by-side nucleosomes and (B) ordered trinucleosomes. Class averages that contain at least one ordered nucleosome are shaded blue.

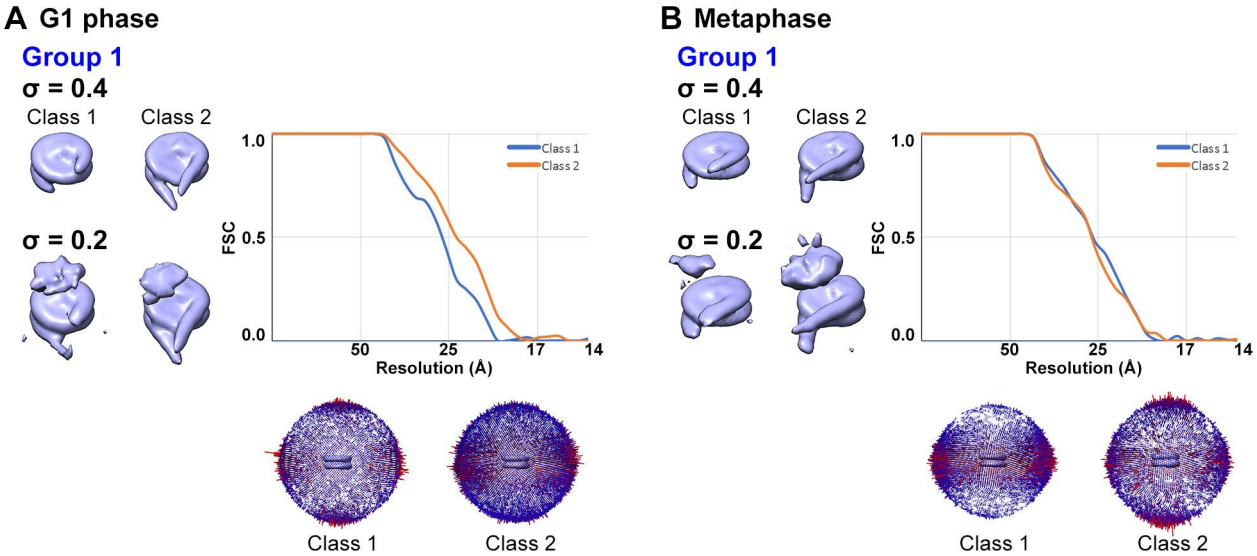

Figure S23. Refinement of Group 1 mononucleosomes combined into two classes.

Mononucleosome classes from Group 1 (Figures 3A and 5A) were manually assigned into two groups, based on the length of the linker DNA. Shown here are the refinement results for the short linker (Class 1) and long linker (Class 2) class for (A) G1 and (B) metaphase cells, respectively. The refined mononucleosome class averages here were used for docking, as shown in Figure 7.

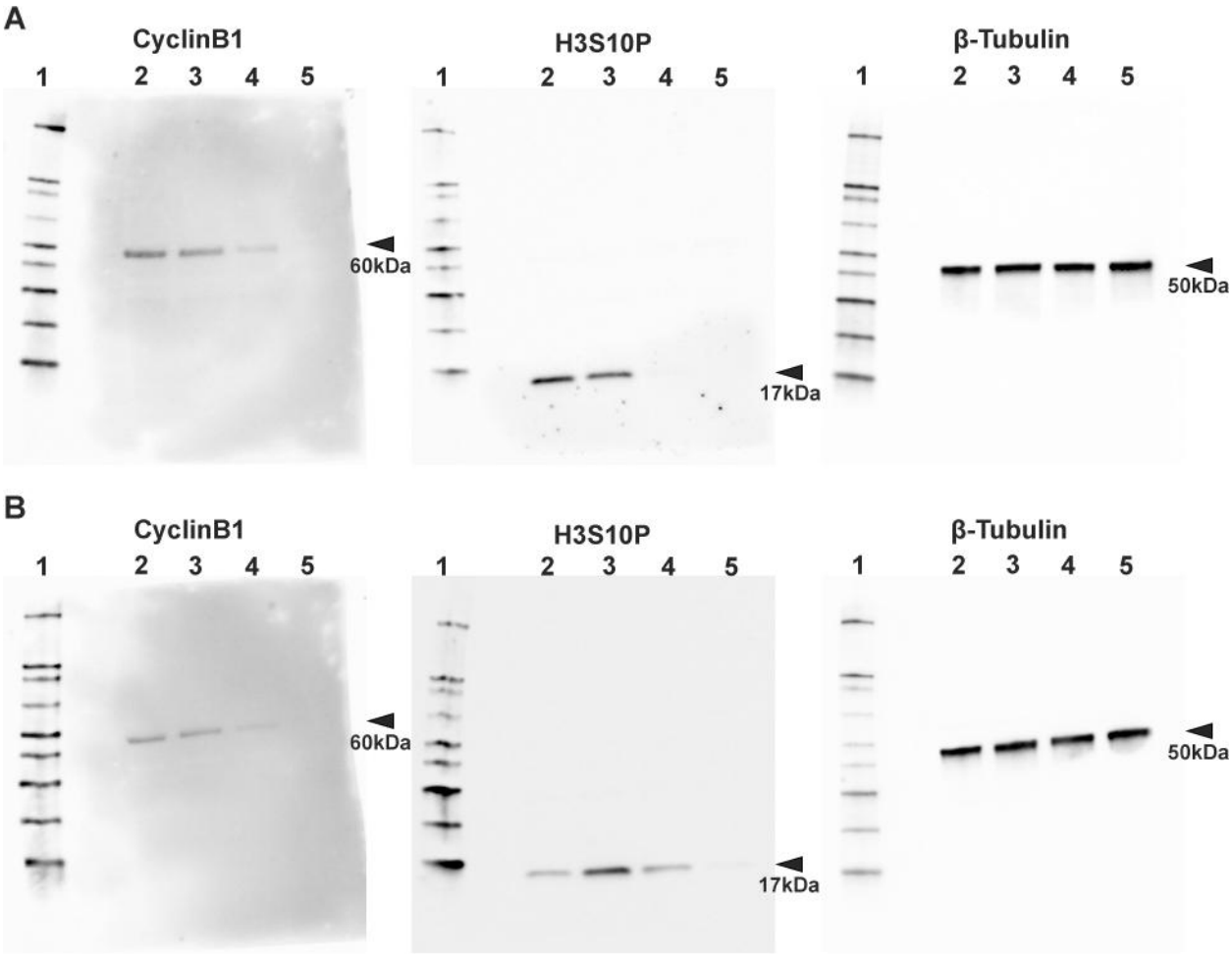

Figure S24. Uncropped immunoblots
The uncropped immunoblots from Figure S1. (A) Nocodazole arrest and washout. (B) MG132 arrest and washout. The lane number is indicated above the gels and correspond, respectively, to the protein ladder (Invitrogen, #LC5602); arrested cells; 30 minutes after washout; 60 minutes after washout; 120 minutes after washout. The position of the relevant band is indicated with the arrowhead, along with the protein's theoretical molecular weight in kilodaltons (kDa).

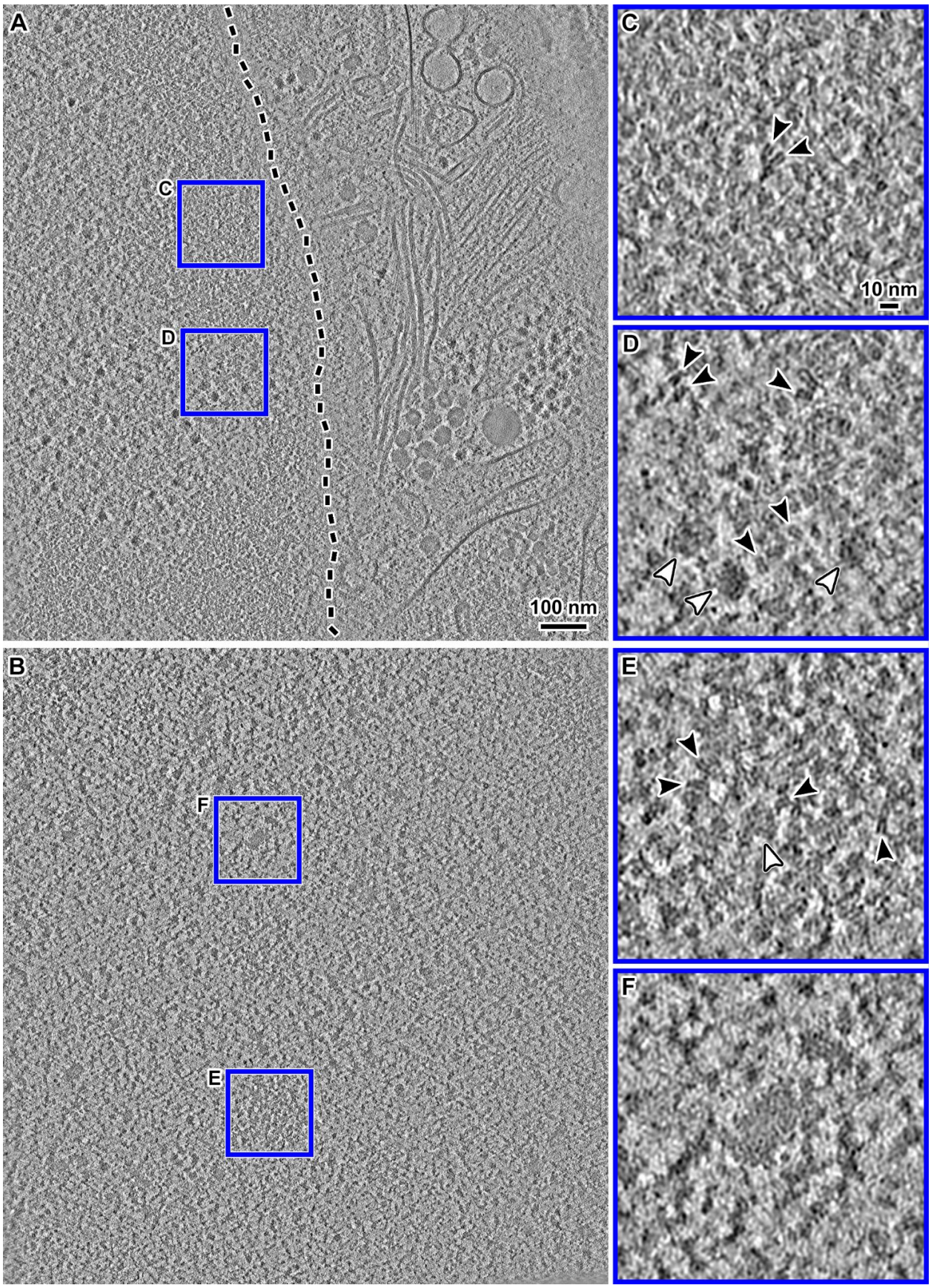
A
C
D
100 nm
B
F
E
C
10 nm
D
E
F

Figure S25. Non-denoised version of Figure 2.

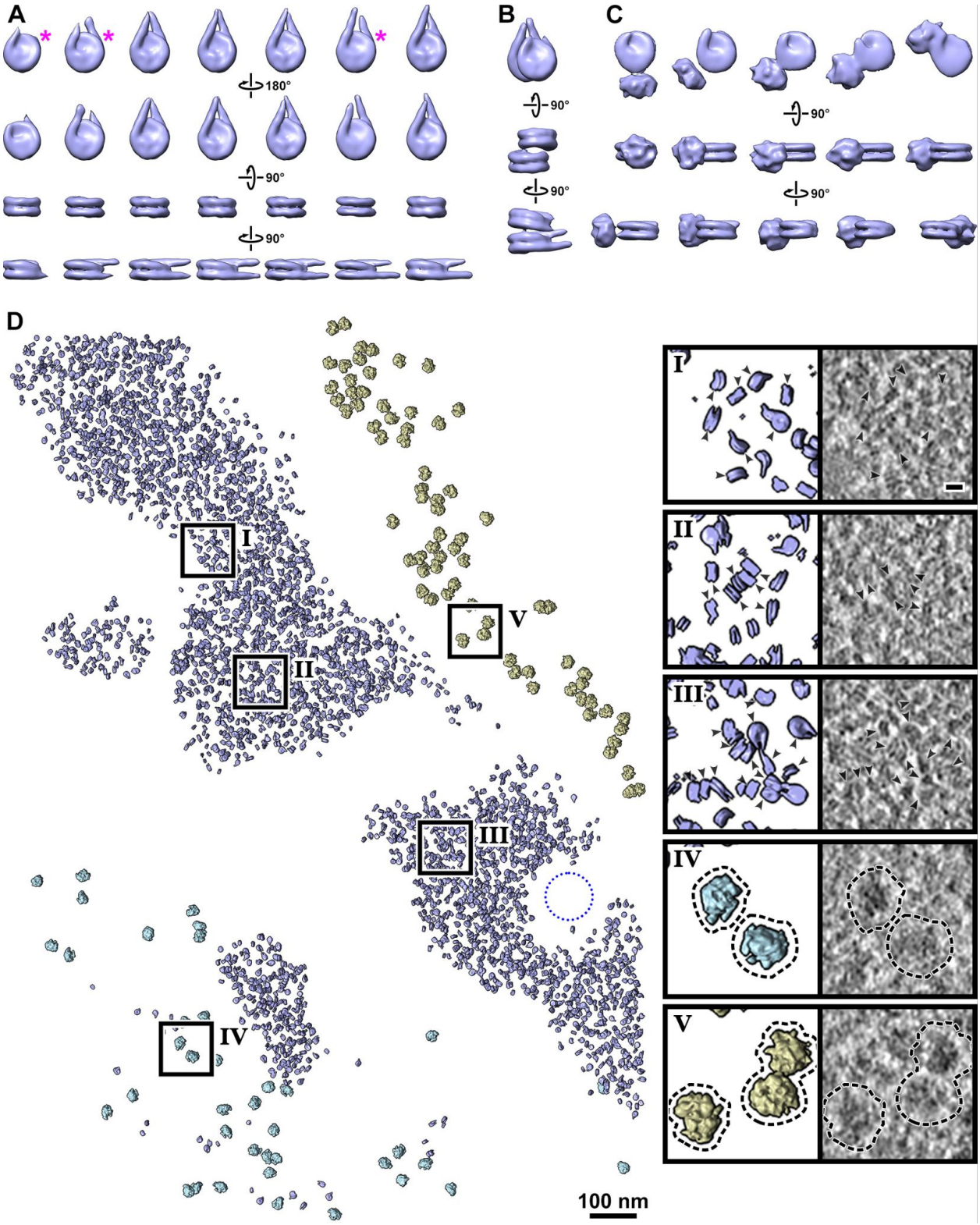

Figure S26. Reproduction of Figure 3, but with non-denoised versions of the cryotomographic slices.

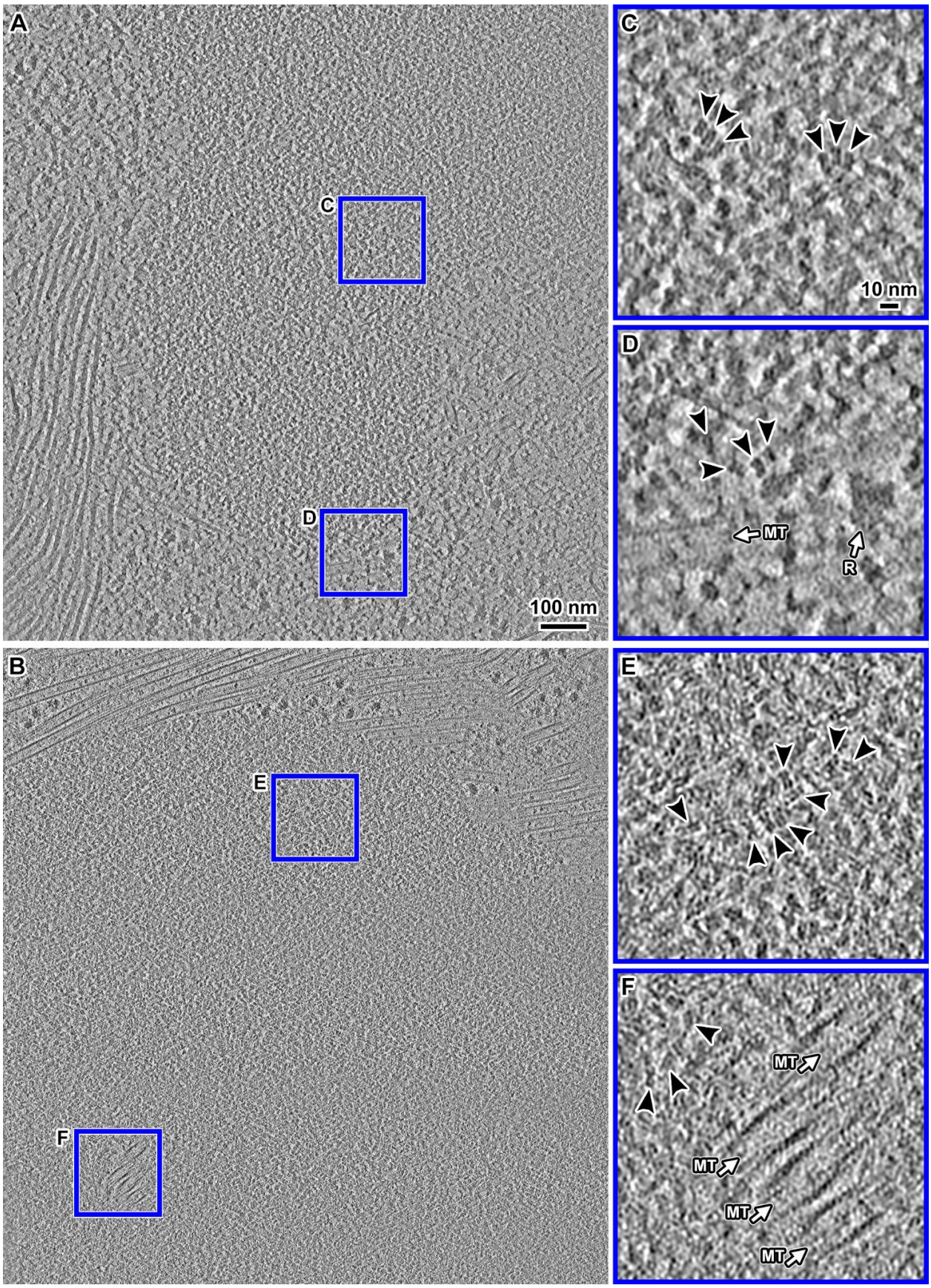
A
C
D
100 nm
B
E
F
C
10 nm
D
MT
R
E
F
MT
MT
MT
MT

Figure S27. Non-denoised version of Figure 4.

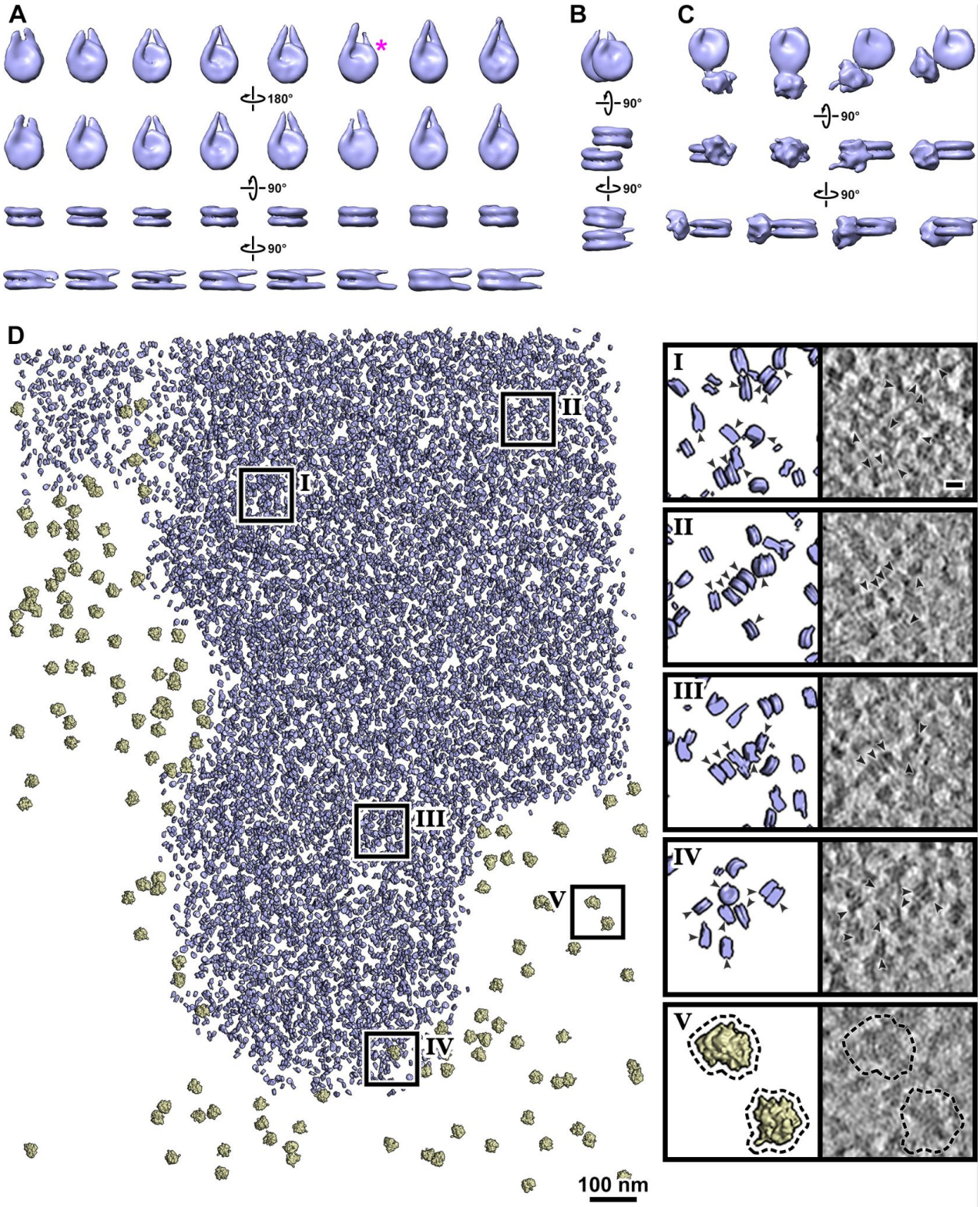

Figure S28. Reproduction of Figure 5, but with non-denoised versions of the cryotomographic slices.

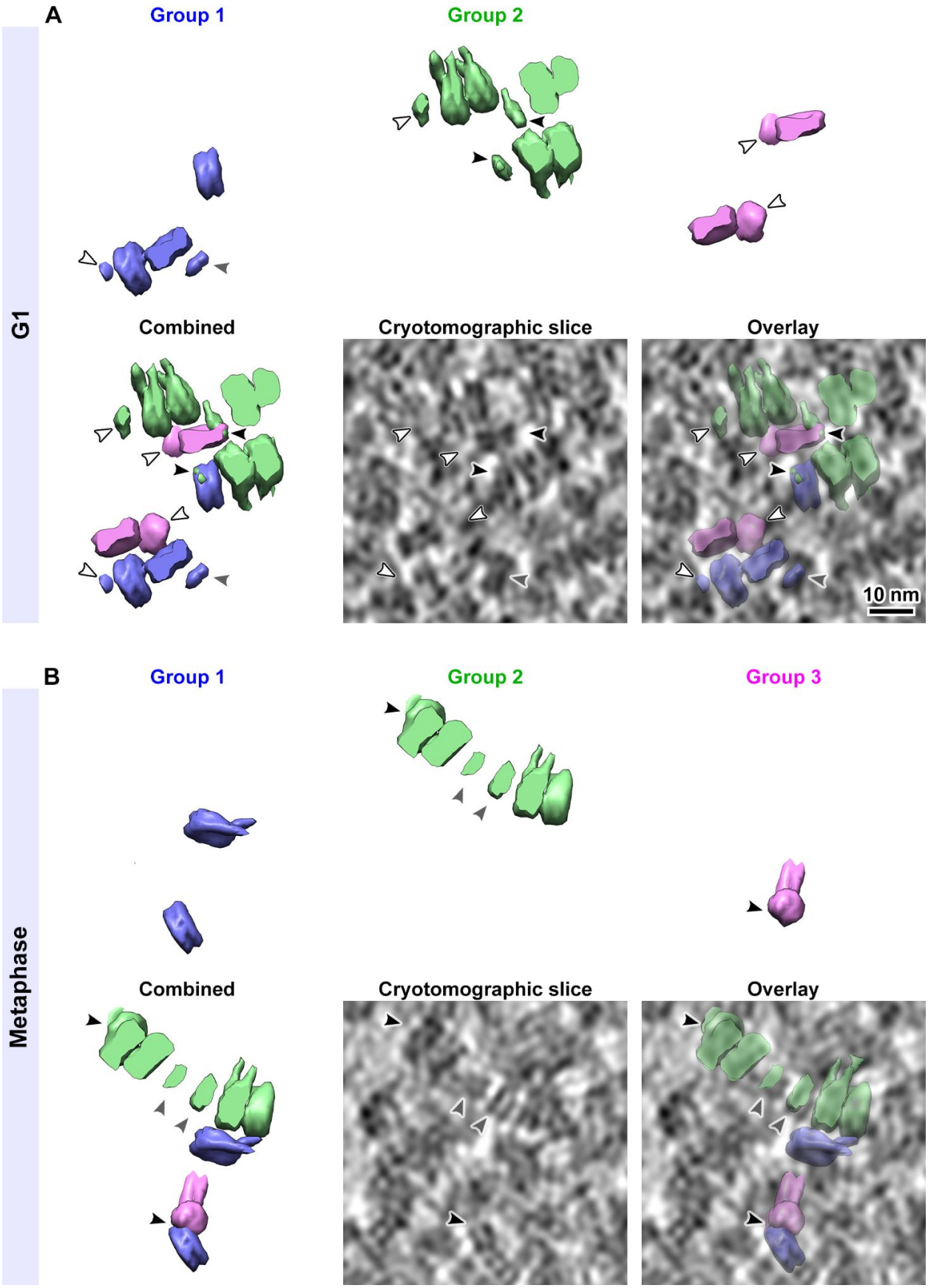
A
Group 1
Group 2
G1
Combined
Cryotomographic slice
Overlay
10 nm
B
Group 1
Group 2
Group 3
Metaphase
Combined
Cryotomographic slice
Overlay

Figure S29. Reproduction of Figure 6, but with non-denoised versions of the cryotomographic slices.

Movie S1. Subtomogram averages of nucleosomes in G1 cell nuclei
Subtomogram averages of mononucleosomes, stacked dinucleosomes, and nucleosomes with a gyre-proximal density, all from G1 chromatin domains. See also Figure 3, A – C.

Movie S2. *In situ* overview of G1 cell nucleus
The cryotomogram is rendered as 10 nm slices. Regions highlighted in blue indicate chromatin domains that were segmented using EMAN2. The remapped model shows nucleosomes (blue) and preribosomes (light blue) in the nucleus and ribosomes (yellow) in the cytoplasm. See also Figure 3D, which is rotated 90° counterclockwise relative to this movie.

Movie S3. Subtomogram averages of nucleosomes in metaphase chromatin
Subtomogram averages of mononucleosomes, stacked dinucleosomes, and nucleosomes with a gyre-proximal density, all in metaphase chromatin. See also Figure 5, A – C.

Movie S4. *In situ* overview of metaphase chromatin
The cryotomogram is rendered as 10 nm slices. The region highlighted in blue indicates chromatin, segmented using EMAN2. The remapped model shows nucleosomes (blue) and ribosomes (yellow). See also Figure 5D, which is rotated 90° counterclockwise relative to this movie.

Table 1. Relative abundance of ordered nucleosome species

	NCP	Di-NCP	Proximal
G1 phase	1.00	0.22	0.49
Metaphase	1.00	0.27	0.37

NCP = mononucleosomes (all linker DNA lengths), Di-NCP = stacked dinucleosomes, Proximal = nucleosomes with proximal density. The ratio is normalized to the number of NCP particles within each cell-cycle state.

Table 2. Summary of chromatin and nuclear features *in situ*

Structural feature	RPE-1 G1	RPE-1 M	HeLa †	Yeast †
≥ 100 nm				
Mitotic chromatin plates	n/a	Not seen	n/a	Not seen
Arc-shaped stacks / slinkies	Not seen	Not seen	Not seen	Not seen
100 – 200 nm periodic structure	Not seen	Not seen	Not seen	Not seen
Interphase domain shape	Irregular	n/a	Irregular	n/a
20 – 80 nm				
Chromatin packing	Irregular	Irregular	Irregular	Irregular
Ordered trinucleosome stacks	Not seen	Not seen	Not seen	Not seen
Slinky oligonucleosomes	Not seen	Not seen	Not seen	Not seen
Megacomplexes (in chromatin)	Rare	Rare	Rare	n/a
Megacomplexes (in nucleoplasm)	Abundant	n/a	Abundant	Abundant
Dense irregular bodies	Rare	Not seen	Rare	in *S. cere*
Pockets (mitotic chromatin)	n/a	Rare	n/a	in *S. pombe*
Pockets (G1 chromatin domain)	Ambiguous	n/a	n/a	n/a
10 – 20 nm				
Ordered dinucleosome stacks	Abundant	Abundant	Not seen	Not seen
Gyre-interacting densities	Abundant	Abundant	n/d	n/d
Canonical mononucleosome	Abundant	Abundant	Abundant	Rare
< 10 nm				
Ordered linker DNA length	Variable	Variable / no ultrashort	Long & short	Long & short
Linker DNA length symmetry	Asymmetric & symmetric	Asymmetric & symmetric	Asymmetric	Asymmetric

The chromatin and nuclear structural features (approximate size ranges in nanometers) of RPE-1 G1 phase (G1), Metaphase (M), HeLa interphase, and *S. pombe* and *S. cerevisiae* in interphase and mitosis (Yeast) are listed. † The HeLa phenotypes are from (Cai et al., 2018a) while the yeast phenotypes are from (Cai et al., 2018b; Chen et al., 2016; Ng et al., 2019; Tan et al., 2023); note that these earlier studies have a smaller sample size of canonical nucleosomes than here. “Not seen” means that the expected structures were absent in our dataset. We cannot rule out that they exist at low abundance. n/a: not applicable. n/d: not determined due to sample size issues.

Table S1. Research resources

Resource	Source	Catalog ID / link
Chemicals		
4′,6-diamidino-2-phenylindole (DAPI)	TFS	D1306
Dimethyl sulfoxide (DMSO)	Sigma	472301
DMEM/F-12 with GlutaMAX	Gibco/TFS	10565-018
Fetal bovine serum	Sigma	F9665
Glycine	Bio-Rad	1610718
MG132	Merck	M7449-1ML
Nocodazole	Merck	SML1665-1ML
Palbociclib	Selleckchem	S1116
Paraformaldehyde	EMS	15714
Penicillin-streptomycin	Gibco	15140-122
Phosphate buffered saline (PBS)	Vivantis	PB0344-1L
PBS-T (PBS + 0.1% Tween 20)	Sinopharm	T20087687
Prolong Gold antifade reagent	TFS	P36930
Taxol	Santa Cruz	33069-62-4
Triton X-100	Alfa Aesar	A16046
Antibodies		
Alexa Fluor® 647 anti-histone H3 (phospho S10)	Abcam	ab196698
Rabbit polyclonal Anti-phospho-Histone H3 (Ser10)	Abcam	ab5176
Mouse anti-rabbit IgG-HRP	Santa Cruz	sc-2357
Rabbit polyclonal to beta Tubulin	Abcam	ab6046
m-IgGκ BP-HRP	Santa Cruz	sc-516102
cyclin B1 (GNS1) mouse monoclonal IgG1	Santa Cruz	sc-245
Anti-RPB1 CTD(S5P)	Abcam	ab5131
Anti-RPB1 CTD(S2P)	Abcam	ab5095
Cell line		
hTERT-RPE-1 cells	ATCC	CRL-4000
Chromatin		
HeLa oligonucleosomes	EpiCypher	16-0003
Light microscopy		
LSM900 AiryScan microscope	Zeiss	N/A
20×, 0.8 N.A. Plan-Apochromat	Zeiss	N/A
63×, 1.4 N.A. oil Plan-Apochromat	Zeiss	N/A
ZEN 3.0 (blue edition)	Zeiss	N/A
Eclipse Ti microscope	Nikon	N/A
Plan Fluor 10x Ph1 objective	Nikon	N/A
20 mm Ø coverslip	Paul Marienfeld GmbH	0112600
Electron cryomicroscopy		

C-flat 2/4 200 mesh, gold	Protochips	CF-2/4-2Au
C-Clip Ring (autogrid)	TFS	1036173
CryoFIB autogrid	TFS	1205101
C-flat 2/4 200 mesh, copper	Protochips	CF-2/4-2C
Continuous carbon	EMS	CF200-Cu-UL
Whatman Grade 1 filter paper	Whatman	1001-055
Copper tubes, 0.3mm inner diameter	Wohlwend	N/A
Copper tube loading tool	Wohlwend	Part 733-1
Copper tube cutting device	Wohlwend	Part 732
UC7/FC7 Microtome	Leica	N/A
35° diamond knife	Diatome	Cryo35
Micromanipulator, Leica	Leica	N/A
Micromanipulator, MN-151-S	Narishige	N/A
Vitrobot Mark IV	TFS	N/A
Helios Nanolab 650 FIB-SEM	TFS	N/A
PolarPrep 2000 Cryo Transfer System	Quorum	N/A
Titan Krios G1 cryo-TEM	TFS	N/A
Falcon II camera	TFS	N/A
Gatan K3 Summit camera	AMETEK	N/A
Gatan BioContinuum imaging filter	AMETEK	N/A
Software		
Adobe Illustrator	Adobe	adobe.com
Adobe Photoshop	Adobe	adobe.com
Adobe Premiere Pro	Adobe	adobe.com
Auxiliary scripts	Gan lab	github.com/anaphaze/ot-tools
BioRender	BioRender	biorender.com
Bsoft	(Heymann and Belnap, 2007)	lsbr.niams.nih.gov/bsoft
EMAN2	(Chen et al., 2017)	blake.bcm.edu/emanwiki/EMAN2
FIJI	(Schindelin et al., 2012)	imagej.net/software/fiji
Google sheets	Google	www.google.com/sheets
IMOD	(Mastronarde, 1997)	bio3d.colorado.edu/imod
PEET	(Nicastro et al., 2006)	bio3d.colorado.edu/PEET
RELION	(Scheres, 2012)	github.com/3dem/relion
SerialEM	(Mastronarde, 2005)	bio3d.colorado.edu/SerialEM
UCSF Chimera	(Pettersen et al., 2004)	www.cgl.ucsf.edu/chimera

Table S2. Antibodies used

Antigen	1º antibody or conjugated antibody	2º antibody	Dilution 1º	Dilution 2º
Immunoblots				
H3S10P	Rabbit polyclonal Anti-phospho-Histone H3 (Ser10) Antibody (Abcam ab5176)	mouse anti-rabbit IgG-HRP (Santa Cruz sc-2357)	1:500	1:500
Cyclin B	cyclin B1 (GNS1) mouse monoclonal IgG1 (Santa Cruz sc-245)	m-IgGκ BP-HRP (Santa Cruz sc-516102)	1:500	1:500
Beta Tubulin	Rabbit polyclonal to beta Tubulin (Abcam ab6046)	mouse anti-rabbit IgG-HRP (Santa Cruz sc-2357)	1:500	1:500
Immunofluorescence				
H3S10P	Alexa Fluor 647 Mouse Monoclonal Anti-Histone H3 (phospho S10) (Abcam ab196698)	N/A	1:250	N/A
RPB1 CTD(S5P)	Rabbit polyclonal, (Abcam ab5131)	Goat anti-Rabbit IgG (H+L) Secondary Antibody, Alexa Fluor 488 (TFS A-11008)	1:300	1:500
RPB1 CTD(S2P)	Rabbit polyclonal, (Abcam ab5095)	Goat anti-Rabbit IgG (H+L) Secondary Antibody, Alexa Fluor 488 (TFS A-11008)	1:300	1:500

TFS = Thermo Fisher Scientific.

Table S3. Confocal microscopy details

General	
Model	Zeiss LSM900
Control software	cellSense v X.Y
Pinhole	1 AU
X, Y pixel	0.087 [μm]
Z pixel	0.410 [μm]
Acquisition	
Objective Lens	UPLSAPO 60XO
Objective Lens Mag.	60×
Objective Lens NA	1.35
Scan Device	Galvano
Scan Direction	One way
Sampling Speed	2.0 [μs/pixel]
Sequential Mode	Line
Integration Type	None
Integration Count	0
Zoom	×2.38
GFP channel settings	
Emission WaveLength	510 [nm]
PMT Voltage	500 [V]
C.A.	200 [μm]
Bits/Pixel	12 [bits]
Laser Wavelength	488 [nm]
Laser Transmissivity	0.05 [%]
AOTF/AOM Transmissivity	0.5 [%]
Laser ND Filter	10 [%]
Detection Wavelength	500 – 600 [nm]
DIC channel settings	
PMT Voltage	380 [V]
C.A.	200 [μm]
Bits/Pixel	12 [bits]
Laser Wavelength	488 [nm]
Laser Transmissivity	0.05 [%]
AOTF/AOM Transmissivity	0.5 [%]
Laser ND Filter	10 [%]
Live cell imaging	
Interval	30 seconds
Duration	2 hours
FoV	50 μm × 50 μm

Table S4. Cryo-ET imaging details

Sample preparation	
EM grids	Cryosections: continuous carbon Lamellae: gold
Plunge freezer	Vitrobot Mark IV
Cryomicrotome	UC7/FC7
Attachment device	Crion
Micromanipulators	Leica micromanipulator; Narishige MN-151-S
Cryomicrotome feed	100 nm
Cryo-FIB-SEM	Helios NanoLab 650 DualBeam
Cryo-transfer device	Quorum PP2000T
Milling currents	Rough: 2.8 nA Intermediate: 0.28 nA Polishing: 48 pA
Cryo-ET data collection	
Microscope	Titan Krios
Energy	300 keV
Camera: recording mode	FII: integration K3: super-resolution movie frames
Energy filter width	K3: 20 eV
Tomography software	TFS Tomo4 and SerialEM
Unbinned pixel size	FII: 7.3, 12.4Å K3: 3.4, 4.5 Å
Contrast mechanism	Defocus phase contrast (cryolamellae, cryosections, oligonucleosomes) Volta phase contrast (cryolamellae, cryosections)
Defocus (nominal)	Defocus phase contrast: −5 (K3) or −10 µm (FII) Volta phase contrast: −0.5 µm
Cumulative dose	cryosections: 100 e^- / $Å^2$ oligonucleosomes: 120 e^- / $Å^2$ cryolamellae: 110 e^- / $Å^2$
Dose fractionation	cryosections: 1/cosine oligonucleosomes and cryolamellae: (1/cosine)^(1/y), where y = 4
Tilt range	cryosections: ±60°; bidirectional, negative angles first cryolamellae: −70° to +42° start −14°, dose-symmetric oligonucleosomes: ±60° start 0°; dose-symmetric, negative angles first
Tilt increment	2°
Cryo-ET data analysis	
Tomogram processing	IMOD 4.11
Template matching	PEET 1.15
Reference creation	Bsoft 1.8.8
Mask creation	Bsoft 1.8.8, RELION 3.0.8
Subtomogram analysis	RELION 3.0.8, Auxiliary scripts
Tomogram visualization	UCSF Chimera 1.15, IMOD 4.11
Auxiliary scripts	github.com/anaphaze/ot-tools
Calculations	Google sheets, FIJI

Figure/movie editing	Adobe Photoshop, Illustrator, and Premiere Pro, www.biobender.com

Table S5. Cryotomogram details

Tomogram	Description	Sample	Fig	Dose (e/Å^2)	Pixel size (Å)	∆f * (µm)	Cam	VPP	thick (nm)	resid
20221029_03	G1, 9% DMSO	lamella	2	110	3.4	0.5	K3	+	70	0.49
20221028_39	G1, 9% DMSO	lamella	2	110	3.4	0.5	K3	+	190	0.57
20221028_14	G1, 9% DMSO	lamella	3, 6, S15, Mov S2	110	3.4	0.5	K3	+	80	0.57
20221028_{10, 18, 19, 21, 23, 24, 29, 30, 41} 20221029_{20, 32, 40, 49, 51, 53} 20221030_(Bednar et al., 2017)	G1, 9% DMSO	lamella	-	110	3.4	0.5	K3	+	70–210	0.31–1.40
20220809_05	M, 9% DMSO	lamella	4, 6	110	3.4	0.5	K3	+	150	0.31
20230209_28	M, 9% DMSO	lamella	4, Mov S4	110	3.4	0.5	K3	+	110	0.56
20230209_{42, 58}	M, 9% DMSO	lamella	-	110	3.4	0.5	K3	+	120, 80	0.85, 0.90
20161115_008	M	section	S2	95	12.4	11.1	FII	−	160	0.56
20180528_02	M	section	S2	100	7.3	0.5	FII	+	170	0.86
20201217_01	G1, 0% DMSO	lamella	S4A	120	3.4	7.0	K3	−	140	0.76
20210110_20	G1, 3% DMSO	lamella	S4B	110	3.4	8.1	K3	−	120	0.20
20210303_16	G1, 6% DMSO	lamella	S4C	110	3.4	8.4	K3	−	200	0.52
20210303_02	G1, 9% DMSO	lamella	S4D	110	3.4	8.2	K3	−	110	0.79
20210423_17	M, 9% DMSO	lamella	S5A	110	3.4	4.9	K3	−	150	1.29
20210526_01	M, 9% Glycerol	lamella	S5B	110	3.4	4.2	K3	−	160	0.54
20210923_03	M, 9% DMSO	lamella	S5C	110	3.4	0.5	K3	+	110	0.91
20211101_16	M, 9% Glycerol	lamella	S5D	110	3.4	0.5	K3	+	180	0.73
20210916_03	Oligo	plunge	S6A	120	3.4	0.5	K3	+	~90	0.27
20210904_26	Oligo, 9% DMSO	plunge	S6B	120	3.4	0.5	K3	+	~90	0.41
20221028_31	G1, 9% DMSO	lamella	S8	110	3.4	0.5	K3	+	210	0.31
20210923_09	M, 9% DMSO	lamella	S19	110	3.4	0.5	K3	+	180	0.41
20210916_{05, 06, 07, 09–33}	Oligo	plunge	-	120	3.4	0.5	K3	+	~90	0.27–1.04
20210904_{12–41}	Oligo, 9% DMSO	plunge	-	120	3.4	0.5	K3	+	~90	0.35–1.39

The tilt increment was 2° for all sets. All data reported in this table were used for subtomogram analysis and were deposited as EMPIAR-#####. Treatment/State: G1 = G1 phase; M = metaphase; Oligo = HeLa oligonucleosomes; plunge = plunge frozen. Dose, in electrons / Å^2. Pixel size is the unbinned pixel size as the specimen level. The K3 data were collected in super-resolution mode, with ½ the pixel size reported in the table. Pixel size therefore refers to the camera's "bin ×1" pixel. Refined defocus (∆f) values are reported for defocus phase-contrast data. Nominal defoci are reported for Volta phase-contrast (VPP) data. ∆tilt = tilt increment. Fig = figures that show this

dataset; those without a figure number were used for subtomogram averaging. Camera (Cam): FII = Falcon II, K3 = K3-GIF. thick = thickness, measured from the reconstructed cryotomogram. resid = alignment residual, in nanometers.

Table S6. Subtomogram analysis of chromatin

	Oligonucleosomes		G1 phase lamella		Metaphase lamella	
	0% DMSO	9% DMSO	NCP Class 1 – 7	Di-NCP	NCP Class 1 – 8	Di-NCP
Template matching						
Tomograms	29	30	21		4	
Reference	Cylinder	Cylinder	Cylinder		Cylinder	
Mask	Cylinder	Cylinder	Cylinder		Cylinder	
2-D classification						
Subtomograms	1,136,628	1,280,772	-		-	
Classes (total)	50	50	-		-	
Classes (kept)	34	27	-		-	
T parameter	2	2	-		-	
Mask (Å)	110	110	-		-	
E-step (Å)	25	25	-		-	
3-D classification						
Subtomograms	207,884	175,984	165,964		145,804	
Reference	Cylinder	Cylinder	Di-NCP STA (G1)		Di-NCP STA (Metaphase)	
Mask, sphere (Å)	110	110	240		240	
E-step (Å)	20	20	20		20	
T parameter	4	4	4		4	
Classes (total)	30	30	50		50	
Classes (kept)	2	3	3	1	4	1
Symmetry imposed	C1	C1	C1		C1	
Refinement						
Subtomograms	8,884	9,074	19,489	4,199	17,224	4,668
Reference	Cylinder	Cylinder	NCP Class 1 – 7 STA (G1)	Di-NCP STA (G1)	NCP Class 1 – 8 STA (Metaphase)	Di-NCP STA (Metaphase)
Mask, sphere (Å)	110	110	240	240	240	240
Symmetry imposed	C1	C1	C1	C1	C1	C1
Resolution (Å)						
FSC = 0.5	19.0	19.5	30.6 – 33.7	26.8	32.5 – 34.3	26.3
FSC = 0.143	16.7	18.1	24.3 – 27.4	21.1	24.9 – 26.2	21.3
EMDB entry	EMD-####	EMD-####	EMD-#### EMD-####	EMD-####	EMD-#### EMD-####	EMD-####

NCP = mononucleosomes, Di-NCP = stacked dinucleosomes, STA = subtomogram average. The values here reflect the final major round of 3-D classification (Figures S12D and S20D) and refinement (Figures S13 & S21, A & B).

Table S7. Subtomogram analysis of chromatin – nucleosomes with gyre-proximal densities

	G1 phase lamella					Metaphase lamella			
	Prox. 1	Prox. 2	Prox. 3	Prox. 4	Prox. 5	Prox. 1	Prox. 2	Prox. 3	Prox. 4
Template matching									
Tomograms	21					4			
Reference	Cylinder					Cylinder			
Mask	Cylinder					Cylinder			
2-D classification									
Subtomograms	-					-			
Classes (total)	-					-			
Classes (kept)	-					-			
T parameter	-					-			
Mask (Å)	-					-			
E-step (Å)	-					-			
3-D classification									
Subtomograms	165,964					145,804			
Reference	Di-NCP STA (G1)					Di-NCP STA (Metaphase)			
Mask, sphere (Å)	240					240			
E-step (Å)	20					20			
T parameter	4					4			
Classes (total)	50					50			
Classes (kept)	1					1			
Symmetry imposed	C1					C1			
Refinement									
Subtomograms	2,016	1,309	1,947	2,126	2,038	1,361	1,837	1,725	1,397
Reference	Prox. 1 STA (G1)	Prox. 2 STA (G1)	Prox. 3 STA (G1)	Prox. 4 STA (G1)	Prox. 5 STA (G1)	Prox. 1 STA (Metaphase)	Prox. 2 STA (Metaphase)	Prox. 3 STA (Metaphase)	Prox. 4 STA (Metaphase)
Mask, sphere (Å)	240	240	240	240	240	240	240	240	240
Symmetry imposed	C1	C1	C1	C1	C1	C1	C1	C1	C1
Resolution (Å)									
FSC = 0.5	30.6	33.4	31.3	33.0	33.7	32.5	32.6	33.4	34.3
FSC = 0.143	24.3	25.5	25.3	27.4	26.4	25.6	24.9	25.9	26.2
EMDB entry	EMD-####	EMD-####	EMD-####	EMD-####	EMD-####	EMD-####	EMD-####	EMD-####	EMD-####

Prox. = Nucleosomes with gyre-proximal density, STA = subtomogram average. The values here reflect the final major round of 3-D classification (Figures S12D and S20D) and refinement (Figures S13C and S21C).

Table S8. Subtomogram analysis of megacomplexes

	G1 phase lamella			Metaphase lamella
	Ribosome (Cytoplasm only)	Ribosome (Full volume)	Preribosome (Full volume)	Ribosome
Template matching				
Tomograms	11	21		4
Reference	Sphere	Sphere		Sphere
Mask	Sphere	Sphere		Sphere
2-D classification				
Subtomograms	-	192,309		-
Classes (total)	-	100		-
Classes (kept)	-	15		-
T parameter	-	2		-
Mask (Å)	-	300		-
E-step (Å)	-	20		-
3-D classification				
Subtomograms	11,972	25,886		48,849
Reference	Sphere	Ribosome STA		Ribosome STA
Mask, sphere (Å)	300	300		300
E-step (Å)	50	50		50
T parameter	4	4		4
Classes (total)	30	30		50
Classes (kept)	1	1	1	1
Symmetry imposed	C1	C1		C1
Refinement				
Subtomograms	684	702	635	332
Reference	Ribosome STA	Ribosome STA	Preribosome STA	Ribosome STA
Mask, sphere (Å)	300	300	300	300
Symmetry imposed	C1	C1	C1	C1
Resolution (Å)				
FSC = 0.5	31.7	33.4	33.3	36.8
FSC = 0.143	24.7	24.7	25.4	26.9
EMDB entry	EMD-####	EMD-####	EMD-####	EMD-####

STA = subtomogram average.

SUPPLEMENTAL REFERENCES

Bednar, J., I. Garcia-Saez, R. Boopathi, A.R. Cutter, G. Papai, A. Reymer, S.H. Syed, I.N. Lone, O. Tonchev, C. Crucifix, H. Menoni, C. Papin, D.A. Skoufias, H. Kurumizaka, R. Lavery, A. Hamiche, J.J. Hayes, P. Schultz, D. Angelov, C. Petosa, and S. Dimitrov. 2017. Structure and Dynamics of a 197 bp Nucleosome in Complex with Linker Histone H1. *Mol Cell*. 66:384-397 e388.

Buchholz, T.-O., A. Krull, R. Shahidi, G. Pigino, G. Jékely, and F. Jug. 2019. Content-aware image restoration for electron microscopy. *In* Methods in Cell Biology. Vol. 152. T. Müller-Reichert and G. Pigino, editors. Academic Press. 277-289.

Cai, S., D. Böck, M. Pilhofer, and L. Gan. 2018a. The in situ structures of mono-, di-, and trinucleosomes in human heterochromatin. *Mol Biol Cell*. 29:2450-2457.

Cai, S., C. Chen, Z.Y. Tan, Y. Huang, J. Shi, and L. Gan. 2018b. Cryo-ET reveals the macromolecular reorganization of S. pombe mitotic chromosomes in vivo. *Proc Natl Acad Sci U S A*. 115:10977-10982.

Chen, C., H.H. Lim, J. Shi, S. Tamura, K. Maeshima, U. Surana, and L. Gan. 2016. Budding yeast chromatin is dispersed in a crowded nucleoplasm in vivo. *Mol Biol Cell*. 27:3357-3368.

Chen, M., W. Dai, S.Y. Sun, D. Jonasch, C.Y. He, M.F. Schmid, W. Chiu, and S.J. Ludtke. 2017. Convolutional neural networks for automated annotation of cellular cryo-electron tomograms. *Nature methods*. 14:983-985.

Heymann, J.B., and D.M. Belnap. 2007. Bsoft: image processing and molecular modeling for electron microscopy. *J Struct Biol*. 157:3-18.

Khatter, H., A.G. Myasnikov, S.K. Natchiar, and B.P. Klaholz. 2015. Structure of the human 80S ribosome. *Nature*. 520:640-645.

Mastronarde, D.N. 1997. Dual-axis tomography: an approach with alignment methods that preserve resolution. *J Struct Biol*. 120:343-352.

Mastronarde, D.N. 2005. Automated electron microscope tomography using robust prediction of specimen movements. *J Struct Biol*. 152:36-51.

Ng, C.T., L. Deng, C. Chen, H.H. Lim, J. Shi, U. Surana, and L. Gan. 2019. Electron cryotomography analysis of Dam1C/DASH at the kinetochore-spindle interface in situ. *J Cell Biol*. 218:455–473.

Nicastro, D., C. Schwartz, J. Pierson, R. Gaudette, M.E. Porter, and J.R. McIntosh. 2006. The molecular architecture of axonemes revealed by cryoelectron tomography. *Science*. 313:944-948.

Pettersen, E.F., T.D. Goddard, C.C. Huang, G.S. Couch, D.M. Greenblatt, E.C. Meng, and T.E. Ferrin. 2004. UCSF Chimera--a visualization system for exploratory research and analysis. *J Comput Chem*. 25:1605-1612.

Scheres, S.H. 2012. RELION: implementation of a Bayesian approach to cryo-EM structure determination. *J Struct Biol*. 180:519-530.

Schindelin, J., I. Arganda-Carreras, E. Frise, V. Kaynig, M. Longair, T. Pietzsch, S. Preibisch, C. Rueden, S. Saalfeld, B. Schmid, J.Y. Tinevez, D.J. White, V. Hartenstein, K. Eliceiri, P. Tomancak, and A. Cardona. 2012. Fiji: an open-source platform for biological-image analysis. *Nature methods*. 9:676-682.

Tan, Z.Y., S. Cai, A.J. Noble, J.K. Chen, J. Shi, and L. Gan. 2023. Heterogeneous non-canonical nucleosomes predominate in yeast cells in situ. *Elife*. 12.